# 修士学位論文

**High precision measurement of the cyclotron frequency of the single-trapped antiproton**

**（トラップ中の単一反陽子の**
**サイクロトロン周波数の高精度測定）**

**2014年度**

**広域科学専攻・相関基礎科学系**

**31-136934**
**樋口 嵩**

# CONTENTS

# 1. INTRODUCTION

## 1.1 Motivation

### 1.1.1 Backgroud of the Antimatter research

CPT symmetry [1] is the most fundamental discrete symmetry in the Standard Model of particle physics. It states the invariance of the laws of physics under CPT transformation; a combination of charge conjugation (C), parity transformation (P), and time reversal (T). As a consequence, it predicts the exact symmetry between the properties of matter and their antimatter conjugates. However, this prediction contradicts to the observed matter-dominance of the universe (so called *baryon asymmetry*). This motivates many experiments in various fields to perform tests of CPT invariance by comparing the fundamental properties of matter and antimatter. For example;

- In oscillation experiments, the masses of the $\mathrm{K}^0$ - and $\overline{\mathrm{K}^0}$-mesons were compared with fractional precision at the $10^{-18}$ level [2].
- The $g-2$ values of the electron and the positron were compared with fractional precision of $3.5$ ppt by using Penning traps [3]. The $g-2$ values of the muon and its antiparticle were also compared at the level of $3.7$ ppb with another method [4].
- The magnetic moments of the proton and the antiproton were compared with precision of $4.4$ ppm [5] by Penning trap methods.

The BASE collaboration at the Antiproton Decelerator (AD) [6] of CERN is planning to improve the comparison between the magnetic moment of the proton and the antiproton by at least a factor of 1000 to provide one of the most sensitive tests of CPT invariance in the baryon sector. [7, 8]

### 1.1.2 Penning Trap methods

A Penning trap is a strong tool to probe fundamental physics by high precision measurements of the fundamental properties of charged particles. Its capability to measure the cyclotron frequency $\nu_c$ of charged particles with high precision enables one to measure physical properties of the particle such as the charge-to-mass-ratio or the mass. This becomes possible by the nondestructive measurement via an induced image current by the particle motion in a trap.

In order to measure the magnetic moments of particles, the spin-precession frequency $\nu_L$ (also called Larmor frequency), has to be measured as well. Together with a measurement of the cyclotron frequency $\nu_c$, the magnetic moment of the particle is obtained:

$$\frac{\mu_p}{\mu_N} = \frac{g}{2} = \frac{\nu_L}{\nu_c} \tag{1.1}$$

where $\mu_N$ is the nuclear magnetron. By measuring the Larmor frequency and the cyclotron frequency in the same magnetic field, the magnetic moment, or so-called g-factor is obtained. Larmor frequency is measured by measuring the Larmor resonance by using the continuous Stern Gerlach effect to identify the quantum spin state of the particle [9]. This technique has been applied with great success in measurements of the electron and the positron g-2 values. However, the application of this method to the proton/antiproton system is a considerable challenge, since the magnetic moment of the proton/antiproton is 658 times smaller than that of the electron/positron.

### 1.1.3 The way toward the first direct measurement of the proton g-factor

To overcome this difficultly and apply the Penning trap method to the proton/antiproton comparison, the BASE collaboration demonstrated several milestones.

- The first spin flips with a single trapped proton was observed [10].
- The magnetic moment of the proton was measured with fractional precision at the ppm level [11]
- A spin-flip for a single antiproton was observed for the first time [12].
- The double-Penning trap technique was demonstrated for the proton for the first time [13].

The double-Penning trap technique is the key technique for highly precise proton/antiproton magnetic moment measurements.

Very recently, BASE performed the first direct high precision measurement of the magnetic moment of a single trapped proton by using this technique [14]. The value has precision of 3.3 ppb, outperforms previous Penning trap experiments by a factor of 760 [15], and improves the currently accepted CODATA literature value [16] by a factor of 2.5. By applying this technique to the antiproton magnetic moment, the above mentioned 1000-fold improvement of precision will become possible.

### 1.1.4 Toward the g-factor of the antiproton

In order to apply the double Penning trap technique to measure the magnetic moment of the antiproton, BASE collaboration was preparing a new four-Penning-trap experiment at the AD of CERN within the last two years.

In 2014, BASE had its first beamtime of antiproton beam from the AD. During the beamtime, we successfully captured the first antiprotons in the trap. In addition, we performed high precision measurements of the cyclotron frequency of single antiprotons, which is an important step toward the purposed g-factor measurement. On the way toward these achievements, some unique and sophisticated techniques for antiproton experiments have been invented. This master thesis was developed within the preparation work of the experiment, which has been commissioned in the 2014 antiproton run.

## 1.2 Overview of this thesis

This thesis consists of four parts. Here, the overview of the thesis is provided.

### Part I : Theoretical Basics

We start from discussing the basic theory of the Penning trap to provide a theoretical basis of this thesis. The principle of the Penning trap and the sophisticated five-electrode Penning trap, which realizes highly harmonic electric potential are explained. After that, we will discuss the detection methods to measure the eigenfrequencies of the particle trapped in a Penning trap. By using nondestructive detection techniques, oscillation frequencies can be measured with mHz resolution out of several 10 MHz. The sideband coupling, an essential method for the cyclotron frequency measurement, will be introduced in the end of this part.

Some keywords of this part: *Five-electrode Penning trap, Trap Imperfections, Feedback cooling, Sideband coupling*

### Part II : BASE Experiments

This part gives an overview of the experimental background of BASE including the BASE Penning trap system and the AD.

For the purpose of measuring the properties of the antiproton, we placed our experiment in the AD at CERN. However, regarding perturbing magnetic fields, the AD is a rather noisy environment. Since BASE is very sensitive to magnetic field fluctuations, these fluctuations must be characterized. The results of the magnetic field measurements will also be presented in the end of this part.

Keywords: *AD operation, Data logger system, GMR sensor*

### Part III : Experimental Methods

This part will describe our experimental methods which are needed to prepare for cyclotron frequency measurements of a single antiproton. The purpose of this part is to show preparation of a single antiproton in a well tuned Penning trap.

This part consists of two chapters; *Preparation of a single antiproton* and *Trap Optimization*

In the first chapter, the unique methods to prepare a single antiproton in a Penning trap from the AD antiproton beam will be described. Many of the used techniques have been invented and employed during the beamtime 2014. This chapter describes procedures such as loading of electrons, catching of antiprotons and cleaning of contaminant particles. The unique and fascinating technique to separate and merge antiproton clouds will be shown as the last step. At the end of this chapter, we prepare a single antiproton in a BASE trap.

The second chapter of this part is the tuning of trap parameters for a five-electrode trap of BASE. Two advanced tuning methods will be demonstrated. They take advantage of the frequency shifts of the trapped particle due to the trap imperfections, and realize a highly harmonic, compensated trap. This is a very important step in preparing for high precision measurements of the cyclotron frequency.

## Part IV : High precision measurement of the cyclotron frequency

Finally, we will discuss cyclotron frequency measurements of a single trapped antiproton.

In the beginning of this part, we will discuss the precision of the cyclotron frequency and the factors which contribute to the fluctuations of the cyclotron frequency.

Next, we will discuss the performance of two advanced methods applied for high precision measurements of the cyclotron frequency.

# Part I

# Theoretical Basics

# 2. PENNING TRAP

A Penning Trap is an elegant tool to study the fundamental properties of charged particles with high precision. This chapter describes the theoretical basics of a Penning trap.

## 2.1 Particle motion in the Penning trap

A Penning trap consists of a homogeneous magnetic field $\vec{B} = B_0\vec{e}_z$ and a superimposed electrostatic quadrupolar potential. Suppose that the electric potential is expressed as

$$V(x, y, z) = V_0 C_2 (z^2 - \frac{x^2 + y^2}{2}), \tag{2.1}$$

where $1/\sqrt{C_2}$ is a specified trap length [17], the equations of motion of a particle with charge $q$ and mass $m$ denote

$$\begin{cases} m\ddot{x} = q(V_0 C_2 x + B_0 \dot{y}) \\ m\ddot{y} = q(V_0 C_2 y - B_0 \dot{x}) \\ m\ddot{z} = -2qV_0 C_2 z. \end{cases} \tag{2.2}$$

This can be rewritten as

$$\begin{cases} \ddot{x} - \omega_c \dot{y} - \frac{\omega_z^2}{2} = 0 \\ \ddot{y} + \omega_c \dot{x} - \frac{\omega_z^2}{2} = 0 \\ \ddot{z} + \omega_z^2 z^2 = 0. \end{cases} \tag{2.3}$$

where the *free cyclotron frequency* $\omega_c$[1] and the *axial frequency* $\omega_z$ are defined as

$$\omega_c = \frac{q}{m} B_0 \tag{2.4}$$

$$\omega_z = \sqrt{\frac{2qC_2V_0}{m}}. \tag{2.5}$$

By Eq.(2.3), one can see the $z$ component of the particle motion is a harmonic oscillation with frequency $\omega_z$. The radial motion is decomposed into two eigenmotions with the *modified cyclotron*

[1]Throughout this thesis, either of frequency $\nu$ and its equivalent angular frequency $\omega = 2\pi\nu$ are quoted as *frequency*, depending on which is more convenient in the context.

*frequency* $\omega_+$, and the *magnetron frequency* $\omega_-$,

$$\omega_+ = \frac{\omega_c}{2} + \sqrt{\frac{\omega_c^2}{4} - \frac{\omega_z^2}{2}}, \tag{2.6}$$

$$\omega_- = \frac{\omega_c}{2} - \sqrt{\frac{\omega_c^2}{4} - \frac{\omega_z^2}{2}}. \tag{2.7}$$

The superimposed particle motion of these three eigenmotions is shown in Figure 2.1. For a strong magnetic and a comparably weak electric field, the three eigenfrequencies of the particle motion obey the hierarchy

$$\omega_+ \gg \omega_z \gg \omega_-, \tag{2.8}$$

and they are related to the cyclotron frequency $\omega_c$ of the particle by the so called *invariance theorem* [17],

$$\omega_c^2 = \omega_+^2 + \omega_-^2 + \omega_z^2. \tag{2.9}$$

This relation is robust against first orders of trap imperfections such as a tilt of the trap axis against the magnetic field or ellipticity of the electrodes [17]. Eq.(2.9) means that the cyclotron frequency of the particle is obtained by measuring the three eigenfrequencies $\omega_+$, $\omega_-$, $\omega_z$. Typical values of these frequencies for a (anti)proton in the BASE Penning trap system are

$$\nu_+ = 30\,\text{MHz}, \quad \nu_z = 650\,\text{kHz}, \quad \nu_- = 7\,\text{kHz}.$$

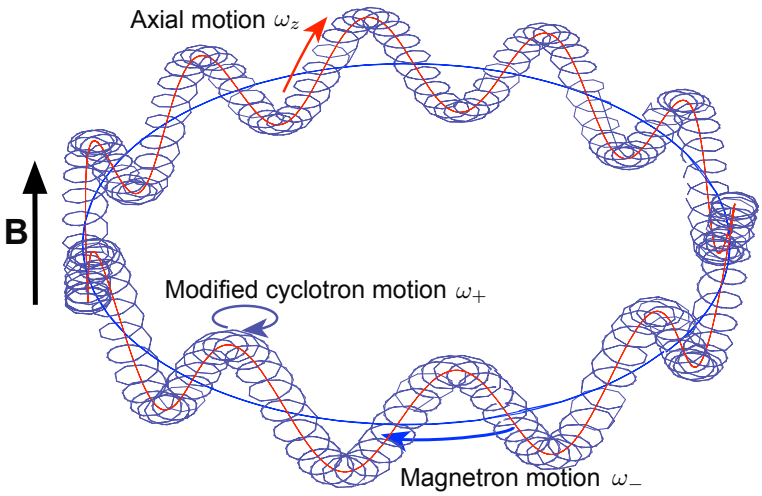


Figure 2.1: The three eigenmotions of a negative charged particle in a Penning trap.

The classical motion described above, is a superposition of threes independent harmonic oscillators, which can be quantized by introducing the canonical commutation relation of each eigenmode.

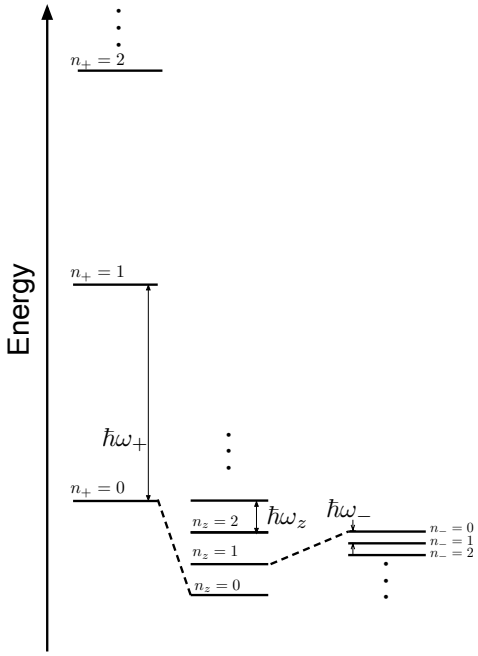


Figure 2.2: An energy diagram of a single particle trapped in a Penning trap. The energy splittings due to the spin of the particle are not shown here.

The Hamiltonian of a single particle is expressed as

$$H = \hbar\omega_+ \left(n_+ + \frac{1}{2}\right) + \hbar\omega_z \left(n_z + \frac{1}{2}\right) - \hbar\omega_- \left(n_- + \frac{1}{2}\right), \tag{2.10}$$

where $n_+, n_z$, and $n_-$ are the quantum numbers of the respective eigenmode. The energy of each mode is calculated for typical trap parameters to be

$$\hbar\omega_+ = 0.12\mu\,\mathrm{eV}, \quad \hbar\omega_z = 2.7\,\mathrm{neV}, \quad \hbar\omega_- = 30\,\mathrm{peV}. \tag{2.11}$$

The energy diagram is shown in Figure 2.2. Note that an increase of the magnetron quantum number lowers the energy of the particle. This can be understood by the classical expression of the magnetron energy :

$$E_- = \frac{1}{2}m\omega_-^2\rho_-^2 - \frac{1}{4}m\omega_z^2\rho_-^2 \simeq -\frac{1}{4}m\omega_z^2\rho_-^2. \tag{2.12}$$

The first term on the second part of the equation is the kinetic energy of the magnetron mode, and the second term is the potential energy in the quadrupolar electrostatic potential, which has a larger contribution due to the relation $\omega_z \gg \omega_-$. This means that the magnetron energy is almost pure potential energy with respect to the ring electrode.

As a consequence, an increase of magnetron radius $\rho_-$ (which corresponds to an increase of the quantum number $n_-$) leads to a decrease of the total energy. In this thesis, the magnetron energy is denoted as $-|E_-|$ for the clarity of discussions.

## 2.2 The Five-Electrode Penning Trap

In the preceding section, we assumed the electrostatic potential of the Penning trap as an ideal quadrupolar potential expressed as Eq.(2.1). In this section we discuss the experimental method to attain a potential which is close to an ideal potential, and how the high-order terms of the potential can be experimentally compensated.

The Penning traps used in the experiment consist of five cylindrical electrodes, as shown in Figure 2.3.

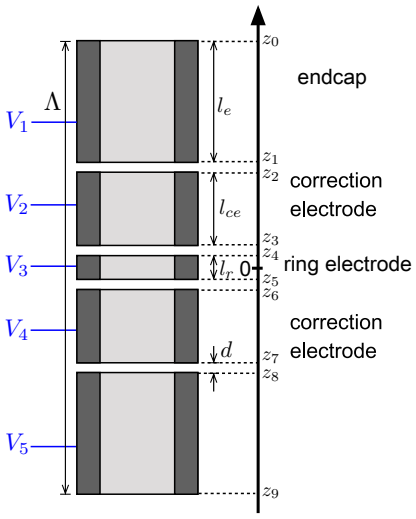


Figure 2.3: Five-electrode Penning Trap

Suppose that we apply a voltage to each of these five electrodes to make a harmonic potential. The electric potential produced by these electrodes is obtained by solving the Laplace equation under the corresponding boundary condition. The Laplace equation in cylindrical coordinates is, if radial symmetry is assumed,

$$\Delta\Phi = \frac{1}{\rho}\frac{\partial}{\partial\rho}\left(\rho\frac{\partial\Phi}{\partial\rho}\right) + \frac{\partial^2\Phi}{\partial z^2} = 0 \tag{2.13}$$

The general solution of this differential equation is expressed using special functions as [18],

$$\Phi(\rho, z) = \sum_{n=1}^{\infty} I_0(k_n\rho)\left[A_n^{(1)}\sin(k_n z) + A_n^{(2)}\cos(k_n z)\right] \quad \left(\text{for } k_n = \frac{n\pi}{\Lambda}\ (n \in \mathbb{N})\right) \tag{2.14}$$

where $\Lambda$ is the total length of the trap, and $I_0$ represents the modified Bessel-functions of second kind. By defining $V_1 = V_5 = 0$, which means grounding these electrodes, coefficients $A_n^{(2)}$ in Eq.(2.14) disappear. The coefficients $A_n^{(1)}$ can be explicitly written down by comparing $\Phi(a, z)$ of Eq.(2.14) with the boundary condition on the surface of the electrodes, where a step-like potential is applied. Finally, the complete expression of the potential is obtained [19].

$$\begin{aligned}\Phi(\rho, z) &= \sum_{n=1}^{\infty}\left[\frac{V_1\cos(k_n z_0) - V_5\cos(k_n\Lambda)}{k_n} + \sum_{i=1}^{4}\frac{V_{i+1} - V_i}{k_n^2 d}\left(\sin(k_n z_{2i}) - \sin(k_n z_{2i-1})\right)\right] \\ &\times \frac{2}{\Lambda}\frac{I_0(k_n\rho)}{I_0(k_n a)}\sin\left(k_n\left(z + \frac{\Lambda}{2}\right)\right)\end{aligned} \tag{2.15}$$

The variables $z_i$ are defined in Figure 2.3. Using this expression, one can see how high order terms of

the potential arise in this case. Suppose that one expands the potential of Eq.(2.15) in the form of

$$\Phi(0,z) = V_0 \sum_{j=0}^{n} C_j z^j \tag{2.16}$$

where $V_0$ is the voltage applied to the ring electrode, which define the gradient of the harmonic potential. The odd coefficients can be neglected for two reasons. First, the terms themselves are small due to the mirror symmetry of the trap design. Second, since the the effect on the forces experienced by the particle are cancelled by averaging over the particle orbit.

By the comparison of Eq.(2.15) and Eq.(2.16), the coefficients $C_j$ are given as

$$\begin{aligned} C_j &= \frac{2}{j!\Lambda V_0} \sum_{n=1}^{\infty} \left[ \frac{V_1 \cos(k_n z_0) - V_5 \cos(k_n \Lambda)}{k_n} + \sum_{i=1}^{4} \frac{V_{i+1} - V_i}{k_n^2 d} (\sin(k_n z_{2i}) - \sin(k_n z_{2i-1})) \right] \\ &\times \frac{(n\pi/\Lambda)^j}{I_0(k_n a)} \sin\left(\frac{\pi}{2}(n+j)\right). \end{aligned} \tag{2.17}$$

By comparing the expression Eq.(2.16) to the Legendre polynomial expression of the Laplace equation, the potential expression including radial coordinates is given as

$$\Phi(\rho,z) = V_0 \sum_j C_j (\rho^2 + z^2)^{j/2} P_j \left( \frac{z}{\sqrt{\rho^2 + z^2}} \right). \tag{2.18}$$

In the experiment, the voltage of each electrode is set as follows.

$$\begin{cases} V_1 = V_5 = 0 \quad \text{(Endcaps:Grounded)} \\ V_3 = V_0 = V_{\text{ring}} \quad \text{(Ring electrode)} \\ V_2 = V_4 = V_{ce} \quad \text{(Correction electrodes)} \end{cases} \tag{2.19}$$

For the further discussion, the *tuning ratio* $\mathrm{TR} = V_{ce}/V_0$ is defined as a voltage ratio between the ring electrode and the correction electrode. By substituting the voltage configuration of Eq.(2.19), Eq.(2.17) can be written in the form

$$C_j = E_j(l_r) + D_j(l_r, l_{ce}) \cdot \mathrm{TR} \tag{2.20}$$

where $D_j(l_r)$ and $E_j(l_r, l_{ce})$ are constants defined by the dimension of the trap i.e. the lengths of the trap electrodes $l_r$, $l_{ce}$ and the trap radius $a$.

By this feature, one can tune the trap parameters to obtain a so called *compensated* and *orthogonal* trap, which satisfies the condition $C_4 = C_6 = D_2 = 0$. The trap *compensation* means that higher order potential coefficients ($C_4$, $C_6$) are compensated, and the *orthogonality* corresponds to $D_2 = 0$, which means one can set the value of $\mathrm{TR}$ without affecting the potential curvature of the trap defined by $C_2$.

In the actual design of the the trap, the radius is fixed by other experimental constraints, and the three free parameters $l_r$, $l_{ce}$, $\mathrm{TR}$ is chosen to satisfy the above conditions [20].

## 2.3 Frequency Shifts Caused by Trap Imperfections

### 2.3.1 Effects of Anharmonicity of the Electrostatic potential

The presence of the higher order terms of the electric potential, which are discussed in the former section, modifies the equation of motion Eq.(2.3) and causes shifts of the eigenfrequencies of the particle motion. These frequency shifts are derived in [21] by treating the effect of anharmonicity perturbatively. The shifts due to $C_4$ and $C_6$ are denoted as

$$\frac{\Delta\omega_+}{\omega_+} = \frac{1}{qV_0}\frac{C_4}{C_2^2}\left(-\frac{3}{4}\left(\frac{\omega_z}{\omega_+}\right)^4 E_+ + \frac{3}{2}\left(\frac{\omega_z}{\omega_+}\right)^2 E_z - 3\left(\frac{\omega_z}{\omega_+}\right)^2 |E_-|\right), \tag{2.21}$$

$$\frac{\Delta\omega_z}{\omega_z} = \frac{1}{qV_0}\frac{C_4}{C_2^2}\left(-\frac{3}{2}\left(\frac{\omega_z}{\omega_+}\right)^2 E_+ + \frac{3}{4}E_z - 3|E_-|\right), \tag{2.22}$$

$$\frac{\Delta\omega_-}{\omega_-} = \frac{1}{qV_0}\frac{C_4}{C_2^2}\left(-3\left(\frac{\omega_z}{\omega_+}\right)^2 E_+ + 3E_z - 3|E_-|\right), \tag{2.23}$$

$$\begin{aligned}\frac{\Delta\omega_+}{\omega_+} = \frac{1}{(qV_0)^2}\frac{C_6}{C_2^3}\Bigg(&-\frac{15}{16}\left(\frac{\omega_z}{\omega_+}\right)^4 E_+^2 - \frac{45}{16}E_z^2 - \frac{45}{4}|E_-|^2 \\ &+\frac{45}{8}\left(\frac{\omega_z}{\omega_+}\right)^2 E_+E_z - \frac{45}{4}\left(\frac{\omega_z}{\omega_+}\right)^2 E_+|E_-| + \frac{45}{2}E_z|E_-|\Bigg),\end{aligned} \tag{2.24}$$

$$\begin{aligned}\frac{\Delta\omega_z}{\omega_z} = \frac{1}{(qV_0)^2}\frac{C_6}{C_2^3}\Bigg(&\frac{45}{16}\left(\frac{\omega_z}{\omega_+}\right)^4 E_+^2 + \frac{15}{16}E_z^2 + \frac{45}{4}|E_-|^2 \\ &-\frac{45}{8}\left(\frac{\omega_z}{\omega_+}\right)^2 E_+E_z + \frac{45}{2}\left(\frac{\omega_z}{\omega_+}\right)^2 E_+|E_-| - \frac{45}{4}E_z|E_-|\Bigg),\end{aligned} \tag{2.25}$$

$$\begin{aligned}\frac{\Delta\omega_-}{\omega_-} = \frac{1}{(qV_0)^2}\frac{C_6}{C_2^3}\Bigg(&\frac{45}{8}\left(\frac{\omega_z}{\omega_+}\right)^4 E_+^2 + \frac{45}{8}E_z^2 + \frac{15}{2}|E_-|^2 \\ &-\frac{45}{2}\left(\frac{\omega_z}{\omega_+}\right)^2 E_+E_z + \frac{45}{2}\left(\frac{\omega_z}{\omega_+}\right)^2 E_+|E_-| - \frac{45}{2}E_z|E_-|\Bigg).\end{aligned} \tag{2.26}$$

The effects of the potential anharmonicity to shifts of the free cyclotron frequency is given by accounting the frequency shift of each eigenfrequency;

$$\frac{\Delta\omega_c}{\omega_c} = \frac{\omega_+}{\omega_c^2}\Delta\omega_+ + \frac{\omega_-}{\omega_c^2}\Delta\omega_- + \frac{\omega_z}{\omega_c^2}\Delta\omega_z. \tag{2.27}$$

These expressions are also important in the sense that they give the relation which enables us to estimate the trap parameters by controlling the energy of eigenmotions. (cf. Chap. 8)

### 2.3.2 Effects of the Magnetic Field Inhomogeneity

Another contribution to the trap imperfections is the inhomogeneity of the magnetic field. By assuming a static magnetic field, the Laplace equation of the magnetic vector potential $\vec{A}$ leads to the following expansion of magnetic field with coefficients $B_k$ [18],

$$\vec{B} = B_0\vec{e_z} + \sum_k B_k((\rho^2+z^2)^{k/2})\left(P_k\left(\frac{z}{\sqrt{\rho^2+z^2}}\right)\vec{e_z} + \frac{1}{k+1}P_k^1\left(\frac{z}{\sqrt{\rho^2+z^2}}\right)\vec{e_\rho}\right) \quad (2.28)$$

where $P_k$, $P_k^1$ are Legendre polynomials. The effect of this inhomogeneity to the shift of the eigenfrequencies are treated in the same way as anharmonicity of the electric potential. If we treat the second order of inhomogeneity, Eq.(2.28) is expressed as

$$\vec{B}(\rho,z) = B_0\vec{e_z} + B_2\left(\left(z^2-\frac{\rho^2}{2}\right)\vec{e_z} - \rho z\vec{e_\rho}\right). \quad (2.29)$$

The frequency shifts due to the presence of $B_2$ are given as,

$$\frac{\Delta\omega_+}{\omega_+} = \frac{1}{m\omega_z^2}\frac{B_2}{B_0}\left(-\left(\frac{\omega_z}{\omega_+}\right)^2 E_+ + E_z - 2|E_-|\right), \quad (2.30)$$

$$\frac{\Delta\omega_z}{\omega_z} = \frac{1}{m\omega_z^2}\frac{B_2}{B_0}\left(E_+ + |E_-|\right), \quad (2.31)$$

$$\frac{\Delta\omega_-}{\omega_-} = \frac{1}{m\omega_z^2}\frac{B_2}{B_0}\left(2E_+ - E_z + 2|E_-|\right). \quad (2.32)$$

Unlike the case of electric potential, one has to consider the effect of $B_1$ term in case of the magnetic field inhomogeneity. To discuss this effect, the equation of axial motion of the particle is expressed as

$$\begin{aligned}\ddot{z} &= -\frac{q}{m}\left(\vec{\nabla}\Phi_e|\vec{e_z}\right) - \frac{1}{m}\left(\vec{\nabla}\Phi_M|\vec{e_z}\right)\\ &= -\frac{q}{m}\left(\vec{\nabla}\Phi_e|\vec{e_z}\right) + \frac{1}{m}\vec{\mu_p}\cdot\vec{B}\end{aligned} \quad (2.33)$$

where $\vec{\mu_p}$ is the magnetic moment of the particle, which is given by

$$\begin{aligned}\vec{\mu_p} &= \frac{q}{2m}\vec{J}\\ &= \frac{q}{2m}\left(\vec{L_+} + \vec{L_-} + \vec{S}\right)\\ &\simeq \frac{q}{2m}\vec{L_+} = \frac{qE_+}{m\omega_+}\vec{e_z}.\end{aligned} \quad (2.34)$$

The existence of the magnetic field gradient $B_1$ shifts the center of the axial oscillation of the particle by

$$\delta z = -\frac{\mu B_1}{m\omega_z^2}. \quad (2.35)$$

Observation of Eq.(2.33) gives the expression of the first order effect of the frequency shift due to this shift of the position of the particle. The cyclotron frequency shift due to $B_1$ is expressed as

$$\frac{\Delta\omega_c}{\omega_c} = -\frac{1}{m\omega_z^2}\left(\frac{B_1}{B_0}\right)^2 E_+ \quad (2.36)$$

## 2.4 Continuous Stern-Gerlach Effect

By superimposing on purpose a large inhomogeneity $B_2$ — so-called "magnetic bottle" — one can detect the spin of the trapped particle as a shift of the axial frequency. Let us treat this effect from Eq.(2.33) as a starting point. In the presence of large $B_2$, Eq.(2.33) is written as

$$\ddot{z} = -\frac{2C_2 q V_0}{m} z - \frac{2\mu_p B_2}{m} z, \tag{2.37}$$

which suggests that the presence of $B_2$ modifies the potential experienced by the particle. The spin momentum of the particle is given as

$$\vec{\mu_s} = \pm g \frac{q}{2m} \frac{\hbar}{2} \vec{e_z} \tag{2.38}$$

according to up/down of the spin of the particles. Substitution of Eq.(2.38) to Eq.(2.37) gives

$$\ddot{z} + \left( \omega_{z,0}^2 \pm g \frac{q\hbar B_2}{2m^2} \right) z = 0 \tag{2.39}$$

where $\omega_{z,0}$ is the modified axial frequency includes the shift due to the angular momentum of the particle coupled with $B_2$. This equation of motion gives the axial frequency depending on the spin state as

$$\omega_z = \sqrt{\omega_{z,0}^2 \pm g \frac{q\hbar B_2}{2m^2}} \simeq \omega_{z,0} \pm g \frac{q\hbar B_2}{4m^2 \omega_{z,0}}. \tag{2.40}$$

As a consequence, the spin flip of the particle results in the axial frequency shift of

$$\Delta\omega_{z,SF} = g \frac{q\hbar B_2}{2m^2 \omega_{z,0}} \tag{2.41}$$

If we prepare a large magnetic bottle, we can detect the spin flip of the particle by the axial frequency shift. This principle of measurement is called *continuous Stern-Gerlach effect* [9]. This principle can be applied to measure the Larmor frequency $\omega_L = gq/(2m)B$. Eq.(2.41) indicates that the frequency shift due to a spin flip scales as $m^{-2}$. In order to increase this frequency shift of the (anti)proton to an observable level, one needs to prepare a very strong superimposed magnetic bottle $B_2$ to the trap. For example, a 100 mHz frequency shift due to a spin flip corresponds to $1.5 \times 10^5\,\mathrm{T/m^2}$. Such a strong magnetic bottle term is realized by using a ferromagnetic ring electrode, made out of a material with high saturation magnetization. In case of BASE, Co/Fe alloys are used for this purpose.

## 2.5 The Double-Penning Trap Method

As mentioned in Chap.1, the g-factor of the particle can be expressed by its cyclotron frequency $\omega_c$ and the Larmor frequency $\omega_L$ as

$$g = 2\frac{\omega_L}{\omega_c}, \tag{2.42}$$

therefore it can be obtained by measuring these two frequencies in the same magnetic field.

The continuous Stern-Gerlach effect enables us to detect the spin state of the (anti)proton by the superimposition of the Penning trap with a strong magnetic bottle $B_2$. On the other hand, as discussed in Sect. 2.3.2, the inhomogeneity of the magnetic field leads to the frequency shift of the cyclotron frequency.

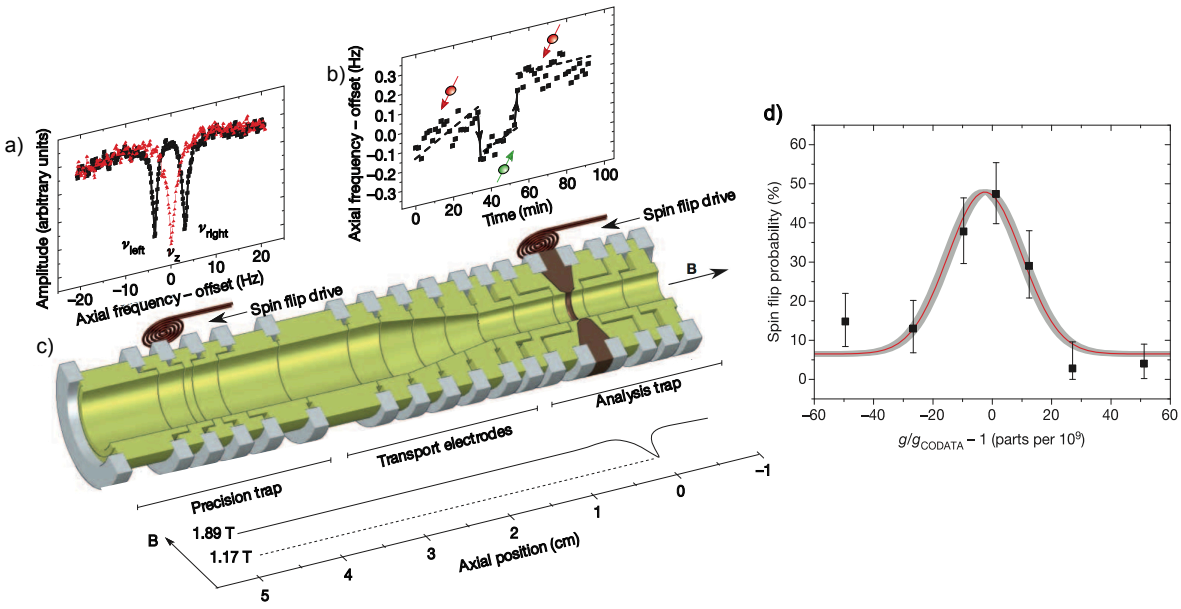


Figure 2.4: The double-Penning trap method applied to the g-factor measurement of the proton.(from [14])

The double-Penning trap method is a method invented to overcome this problem. The idea is to separate the parts of the experiment to measure the cyclotron frequency and to detect the spin state of the particle. Figure 2.4 shows the scheme of the double-Penning trap method. This figure is from [14] where the recent g-factor measurement of the proton is presented. The two traps named as a Precision trap and an Analysis trap have the following features.

- The Precision trap is located under the homogeneous magnetic field. The cyclotron frequency of the particle is measured in high precision. Figure 2.4 b) shows describes the cyclotron frequency measurement using sideband-coupling method. (cf. Sect. 3.31)
- The Analysis trap has a strong superimposed magnetic bottle. By observing the frequency shift of the axial frequency, spin-flips of single particles can be observed.

Two coils to apply the rf drive are implemented to both traps. The experiment follows the procedure below:

1. The particle is trapped in the Analysis Trap in the beginning. The spin state of the particle is determined by the application of the spin-flip drive to observe the frequency shift as shown in a).

2. The particle is transport to the the Precision trap. The cyclotron frequency of the particle is measured.

3. A spin-flip drive with frequency $\nu_1$ is applied to the particle in the Precision trap.

4. The particle is transported back to the Analysis trap to measure its spin state after the drive of $\nu_1$.

A repetition of steps 1 to 4 gives a transition probability of the rf drive with frequency $\nu_1$. By sweeping the rf frequency $\nu_1$ and repeating the same set of procedure for each, the g-factor resonance curve is obtained as shown in Figure 2.4 d). The principle of the cyclotron frequency measurement will be discussed in the next chapter. The detail of the BASE traps will be described in Chap. 5.

# 3. Detection Methods

## 3.1 Detection Principle

So far, we have discussed the particle motion and its eigenfrequencies in a Penning trap. This section describes the method to measure these frequencies by non-destructive electronic detection.

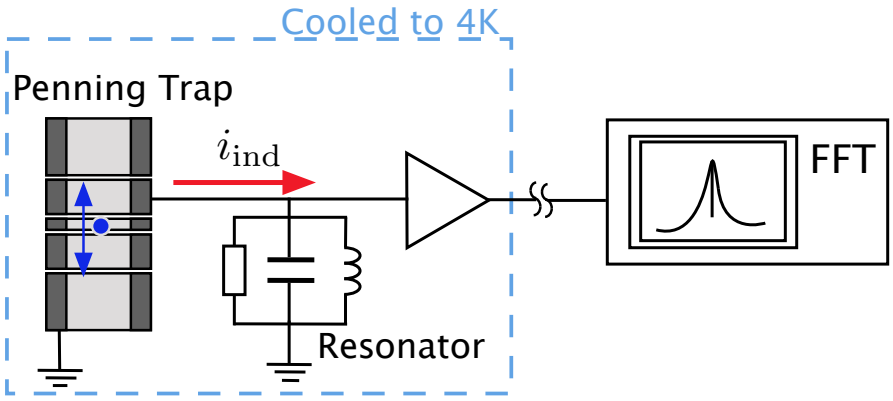


Figure 3.1: Illustration of the image-current detection principle in a Penning trap. The particle motion creates an oscillating image current at its motional frequency. The image current is detected using a cryogenic resonator and amplifier.

### 3.1.1 Description of the Detection System

The schematic in Figure 3.1 shows the detection system of a Penning trap. One of the trap electrodes is connected to a tuned circuit with a high quality factor formed by a superconducting coil inside a resonator and the parasitic capacitance of the trap electrodes. The trap, resonator, and the amplifier are placed in the cryogenic environment and cooled to 4 K.

The particle trapped in the Penning trap induces image currents at the eigenfrequency of the eigenmotion of the particle. The frequency of the image current is detected by the interaction of the particle with the detector. The frequency of the signal is down-converted to be measured by an FFT analyzer[1] with the resolution of 1 mHz. Hereafter, the axial motion of the particle is treated to explain the detection principle.

[1] All the FFT spectra shown in this thesis is mixed down by Mini Circuits ZAD-8, and measured by Stanford Research SR780.

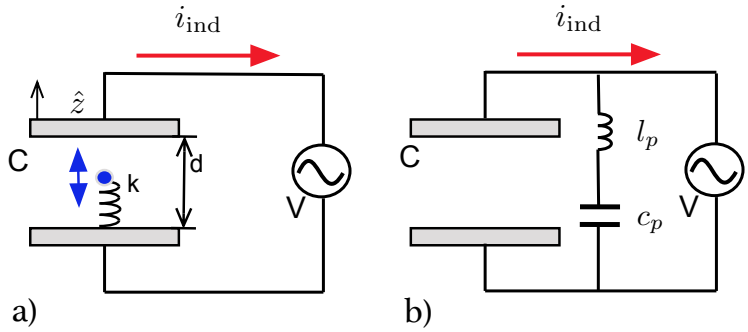


Figure 3.2: b) shows the equivalent circuit of a), where the oscillating particle is replaced with inductor $l_p$ and capacitor $c_p$.

### 3.1.2 The Trapped Particle as an Equivalent Circuit

To discuss the detection of the image current caused by the trapped particle, we start from the simple model described in Figure 3.2 a), where a particle of charge $q$ and mass $m$ is supposed to be connected to a parallel plate capacitor $C$ by an electrically neutral massless spring $k\,(\omega_z = (k/m)^{1/2})$ The current induced by the trapped particle is given as [22]

$$i_{\text{ind}} = \frac{qv_z}{d}. \tag{3.1}$$

where $d$ is the distance between the plates of the capacitor $C$. On the other hand, the equation of motion of the particle is expressed as

$$m\ddot{z} = -kz + F_e \tag{3.2}$$

where $F_e$ is the external force on the particle:

$$F_e = \frac{qV}{d}. \tag{3.3}$$

In Eq.(3.2), a Coulomb force due to the induced current is neglected since it is assumed that the particle's amplitude is small compared to $d$, which corresponds to typical experimental conditions. By using Eq.(3.1) and Eq.(3.3), Eq.(3.2) is rewritten as

$$l_p \frac{di_{\text{ind}}}{dt} + \frac{1}{c_p}\int i_{\text{ind}} dt = V \tag{3.4}$$

where $l_p = md^2/q^2$ and $c_p = (\omega_z^2 l_p)^{-1}$. This equation relates the oscillatory motion of the particle to the equivalent circuit shown in Figure 3.2 b).

If a resistor is connected in parallel to the capacitor $C$, as described in Figure 3.3, power consumption on the resistor is expressed as

$$P = \frac{dE}{dt} = R \cdot i_{\text{ind}}^2. \tag{3.5}$$

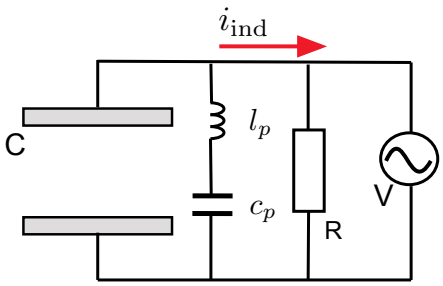


Figure 3.3: An equivalent circuit of the trapped particle, with the resistance.

This power consumption dissipates the energy of the particle, which modifies Eq.(3.2) and Eq.(3.4) as

$$m\ddot{z} = -kz - m\gamma\dot{z} + F_e, \tag{3.6}$$

$$l_p \frac{di_{\mathrm{ind}}}{dt} + R \cdot i_{\mathrm{ind}} + \frac{1}{c_p}\int i_{\mathrm{ind}} dt = V \tag{3.7}$$

with a damping constant $\gamma$. By comparing Eq.(3.6) and Eq.(3.7), the relation between the damping constant and the circuit components is obtained. $\gamma$ together with the time constant $\tau$ is expressed as

$$\gamma = \frac{q^2 R}{md^2} \iff \tau = \frac{md^2}{q^2 R}. \tag{3.8}$$

The dissipation caused by the resistive component plays an important role in the dynamical behavior of the particle's interaction with the detector, which will be discussed in the following section.

The discussions so far can be extended to the case of $n$ uncorrelated particles. Eq.(3.1) and Eq.(3.2) are rewritten using the center of mass coordinates of the particles $Z = \sum_k^n z_k/n$ [22];

$$i_{\mathrm{ind},n} = \frac{nq\dot{Z}}{d} \tag{3.9}$$

$$m\ddot{Z} = -kZ + \frac{qV}{d} \tag{3.10}$$

Therefore, $n$ uncorrelated oscillating particles are expressed by the equivalent circuit in Figure 3.2 b) with the replacement of

$$l_p \to \frac{l_p}{n}, \quad c_p \to nc_p. \tag{3.11}$$

### 3.1.3 Interaction of the Trapped Particle with the Detection System

Figure 3.4 gives the equivalent circuit of a particle trapped in a Penning trap. In this case, $l_p$ and $c_p$ are redefined as $l_p = mD^2/q^2$ and $c_p = (\omega_z^2 l_p)^{-1}$, where $D$ is a quantity of the trap called *effective*

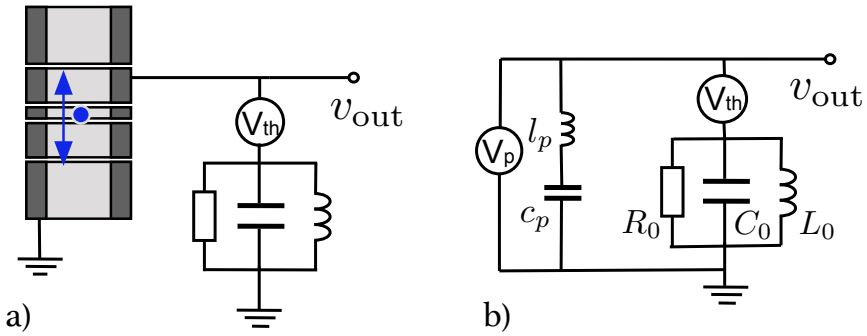


Figure 3.4: b) shows the equivalent circuit of a).

*electrode distance*. The effective electrode distance depends on the trap geometry and the details of the pickup geometry. The capacitor as shown in Figure 3.2 is included to $C_0$ in Figure 3.4. $\mathrm{V_p}$ expresses the potential produced between the trap electrodes due to the particle motion.

The detector is expressed as a parallel tank circuit with $R_0$, $C_0$, $L_0$. The resonance frequency of the detector $\nu_0 = 1/2\pi\sqrt{L_0 C_0}$ is tuned to be $\nu_0 \sim \nu_z = \omega_z/2\pi$. The impedance of the detector $Z_d$ is expressed as

$$Z_{\mathrm{d}} = \left(\frac{1}{R_0} + j\left(\omega C_0 - \frac{1}{\omega L_0}\right)\right)^{-1} \tag{3.12}$$

This expression gives the relation

$$R_0 = 2\pi\nu_0 L_0 Q \tag{3.13}$$

where $Q$ is the quality factor of the resonance. $Q$ is defined by the resonance frequency $\nu_0$ and the 3dB width of the resonance $\Delta\nu$ as

$$Q = \frac{\nu_0}{\Delta\nu}. \tag{3.14}$$

To obtain a good signal strength, the detector should have high $R_0$ and $Q$, whose typical values are $1\,\mathrm{G\Omega}$ and $100\,\mathrm{k\Omega}$, respectively. The impedance of the detector expressed as Eq.(3.12) is simplified around the resonant frequency of the detector $\nu \sim \nu_0$ as

$$Z_{\mathrm{d}} \sim R_0. \tag{3.15}$$

Let us discuss how the output signal at $v_{\mathrm{out}}$ in Figure 3.4 is expressed. The spectrum on the FFT analyzer detected via the amplifier (cf. Figure 3.1) is the resonance of the overall circuit in Figure 3.4 b), driven primarily by the Johnson-Nyquist noise $V_{\mathrm{th}}$. The amplitude of $V_{\mathrm{th}}$ satisfies [23]

$$\overline{V_{\mathrm{th}}^2} = 4k_B T \Delta f \cdot \mathrm{Re}[Z_{\mathrm{total}}] \tag{3.16}$$

for a frequency bandwidth $\Delta f$. $T$ in Eq.(3.16) represents the temperature of the detector, which is about 4 K, as mentioned in the former part of this section.

The total impedance of the circuit around the resonant frequency $\nu \sim \nu_0$ can be approximated by

$$Z_{\text{total}} \sim \frac{R_0 \left(\omega l_p - \frac{1}{\omega c_p}\right)^2 - j\left(\omega l_p - \frac{1}{\omega c_p}\right)}{R_0^2 + \left(\omega l_p - \frac{1}{\omega c_p}\right)^2}. \tag{3.17}$$

The real part of the total impedance is given as

$$\text{Re}[Z_{\text{total}}] \sim \frac{R_0}{1 + \frac{R_0^2}{\omega_z^2 l_p^2}\left(\frac{\omega\omega_z}{\omega^2 - \omega_z^2}\right)^2}. \tag{3.18}$$

Eq.(3.18) indicates that $\text{Re}[Z_{\text{total}}]$ is an inverse Lorentzian-like function of $\nu$ scaled by $R_0$ which has the offset of $R_0$ and a dip at frequency $\nu_z$. The output spectrum signal is given by Eq.(3.16) and Eq.(3.18) as

$$\sqrt{\overline{v_{\text{out}}^2}} = \sqrt{4k_B T \Delta f \frac{R_0}{1 + \frac{R_0^2}{\omega_z^2 l_p^2}\left(\frac{\omega\omega_z}{\omega^2 - \omega_z^2}\right)^2}}. \tag{3.19}$$

The actual signal of this interaction is shown in the spectrum of Figure 3.5 b). The qualitative explanation of this behavior is as follows; Among the signal generated by the thermal noise $e_{th}$, off-resonant components ($\nu \neq \nu_z$) go through the resistance component of the detector. On the other hand, the frequency component of $\nu = \nu_z$ goes through the series tank circuit $l_p$, $c_p$ and shorts the spectral noise of the resonator. The full width at half maximum of the dip is calculated as [22]

$$\Delta\nu_z = \frac{1}{2\pi}\frac{R_0}{l_p} = \frac{1}{2\pi}\frac{q^2 R_0}{mD^2} = \frac{1}{2\pi\tau_z} \tag{3.20}$$

where $\tau_z$ is the damping time constant $\tau$ introduced in Eq.(3.8), with the replacement of $R \to R_0$, $d \to D$. Together with the relation between the number of trapped particles $n$ and $l_p$ in Eq.(3.11), one can see that the dip width for $n$ particles stored in a Penning trap is expressed as

$$\Delta\nu_{z,n} = \frac{n}{2\pi}\frac{1}{\tau_z} = \frac{n}{2\pi}\frac{q^2 R_0}{mD^2}. \tag{3.21}$$

This relation is useful to count the number of stored particles by the signal on the FFT analyzer.

The transient interaction between a trapped particle and the resonator is discussed as follows.

If the trapped particle has a high energy, thus has a large amplitude, the direct signal with the particle's eigenfrequency is observed as a peak in the FFT analyzer spectrum as shown in Figure 3.5 a). The trapped particle loses its energy through the energy dissipation at the resistive component of the resonator. Through this process, the amplitude of the oscillating signal $V_{\text{p}}$ decreases to the same order as the thermal noise $V_{\text{th}}$. This process is called *resistive cooling*. After being restively cooled, the particle appears as a dip in the signal of the FFT analyzer as shown in Figure 3.5 b).

When the eigenmode of the particle is coupled to the resonator and reaches the equilibrial state, the probability distribution of the energy of this mode is given as a Boltzmann distribution defined by the temperature of the resonator. Hereafter we define this temperature as a temperature of the eigenmode of the particle.

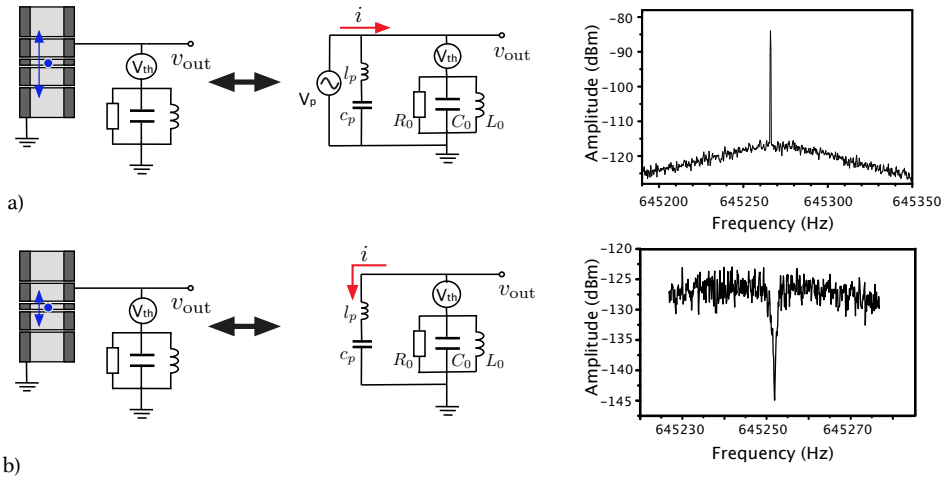


Figure 3.5: The equivalent circuit of the detection system and the signal of the spectrum of an FFT analyzer. In a), the power dissipation of an excited particle is observed. In b), the short of the resonator's thermal noise due to a particle in thermal equilibrium is shown.

## 3.2 Temperature Control by an Active Feedback System

In the preceding section, it was shown that the interaction with the detector cools the particle to the temperature defined by the amplitude of thermal noise of the resonator. The concept of active feedback is that one can control the particle temperature by tuning the noise voltage by the application of feedback.

Figure 3.6 illustrates the concept of the feedback system. Figure 3.6 a) describes the detection system without feedback. The resonator is simplified as a resistor $R_0$. The thermal noise due to the detector resistance is represented as $V_{\mathrm{th}}$. $T_0$ is the temperature of the environment where the detector is placed. Figure 3.6 b) gives the circuit with feedback line to the trap electrode. Throughout discussion in this section, $g$ stands the gain of the negative feedback signal, $V_{\mathrm{g}}$ stands the noise signal due to the fed-back amplifier signal. Figure 3.6 c) describes its equivalent circuit in the sight of the trapped particle, replacing the feedback components of Figure 3.6 b) by the effective noise voltage $V_e$ and the effective resistance $R_e$. The effective temperature of the resonator $T_e$ is the temperature experienced by the particle, which is defined by $V_e$ and $R_e$.

This section derives how the effective temperature of Figure 3.6 c) $T_e$ is expressed as a function of the feedback gain in order to see how the feedback system can control particle temperature.

As already mentioned in Eq. (3.16), the thermal noise $V$ generated on the resistance $R$ generally satisfy

$$\overline{V^2} = 4k_B T R \Delta f. \tag{3.22}$$

Another general property of thermal noise is

$$\overline{V} = 0. \tag{3.23}$$

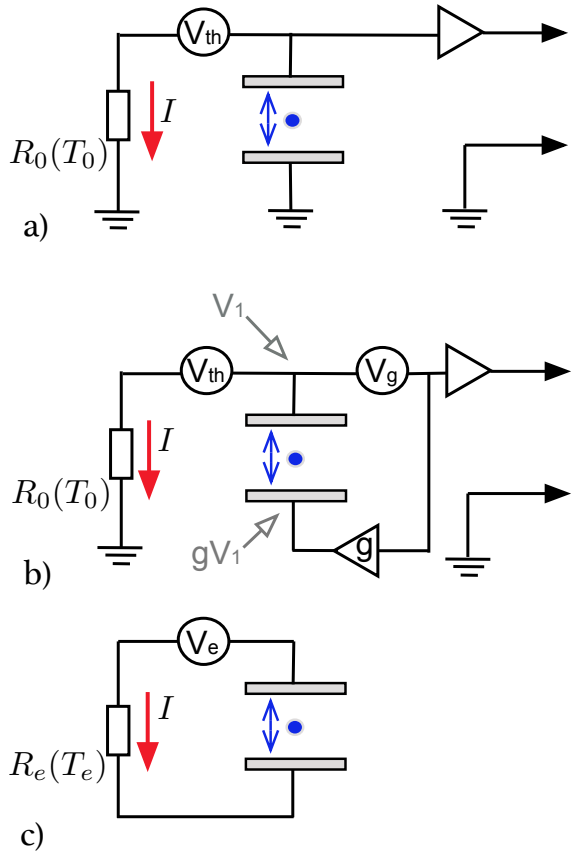


Figure 3.6: The conceptual circuit without a) and with b) feedback. c) gives the equivalent circuit of b), which is experienced by the trapped particle.

Therefore, there is a relation between $(T_0, R_0)$ and $(T_e, R_e)$ as

$$\frac{T_e}{T_0} = \frac{\overline{V_e^2}}{\overline{V_{\text{th}}^2}} \frac{R_0}{R_e}. \tag{3.24}$$

$R_e$ is identified by comparing the voltage between trap electrodes of Figure 3.6 b) and c).

$$\begin{aligned} V_1 - gV_1 + \overline{V_{\text{th}}} &= (1-g)IR_0 = IR_e \\ &\Rightarrow R_e = (1-g)R_0 \end{aligned} \tag{3.25}$$

$\overline{V_e^2}$ is derived by comparing the noise voltage amplitude between the trap electrode as

$$\overline{V_e^2} = (1-g^2)\overline{V_{\text{th}}^2} + g^2\overline{V_g^2}. \tag{3.26}$$

According to Eq.(3.24), the ratio between the temperature with and without feedback is expressed as

$$\begin{aligned} \frac{T_e}{T_0} &= \left( (1-g)^2 + g^2 \frac{\overline{V_g^2}}{\overline{V_{\text{th}}^2}} \right) \cdot \frac{R_0}{R_e} \\ &= 1 - g + \frac{g^2}{1-g} \frac{\overline{V_g^2}}{\overline{V_{\text{th}}^2}}. \end{aligned} \tag{3.27}$$

This demonstrates that the application of feedback can be used to reduce the temperature of the particle, which has a wide application in high precision Penning trap experiment.

If the noise from the amplifier $V_g$ are negligible, Eq.(3.27) is simplified as $T_e = (1-g)T_0$. In reality, the existence of $V_g$ determines the limit of cooling by the feedback. Inserting a phase shifter to the feedback line, one can control the phase of the feedback. Positive feedback heats the particle temperature.

As defined in Eq.(3.8), the damping time constant $\tau_z$ which defines the time scale of thermalization of the particle is expressed as

$$\tau_z = \frac{1}{\gamma_z} = \frac{mD^2}{q^2 R} \tag{3.28}$$

Therefore the damping constant is varied according to the feedback strength as,

$$\tau_{z,e} = \frac{1}{1-g} \tau_{z,0}, \tag{3.29}$$

which means that the cooling with negative feedback cool the resonator temperature and results in a slower resistive cooling of the particle.

The application of a feedback system to the measurement will be discussed in Chap.11.

## 3.3 Sideband Coupling Method

As explained in Sect.2.1, the three eigenmotions of the trapped particle are independent from each other, therefore while neglecting higher order trap imperfections, there is no energy transfer between two modes.

The sideband coupling method [17, 25] mixes two eigenmotions by the principle of Rabi resonance. We employ this method to measure all eigenfrequencies with an axial detector by coupling the radial motions to the axial mode.

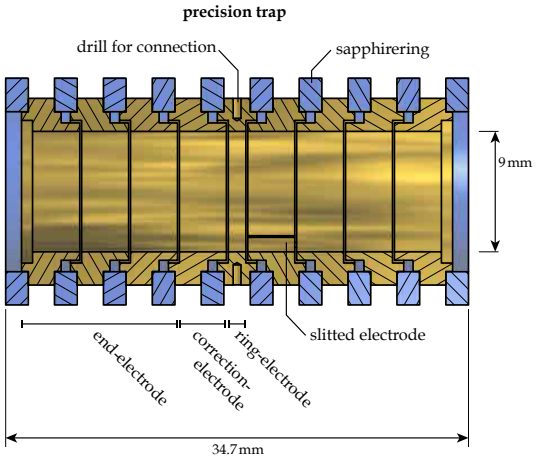


Figure 3.7: The Precision Trap of the BASE experiment. The correction electrode on the right side is slitted to produce a quadrupolar excitation rf signal. This figure is taken from [20]

Figure 3.7 shows the configuration of electrodes of one of the traps of BASE. By applying an rf signal[2] with frequency $\nu_{\text{rf}}$ at the radially segmented electrode (indicted as "slitted electrode" in Figure 3.7), one can produce a field expressed as

$$\vec{E} = \text{Re}\left[\mathcal{E}_0 \exp(i2\pi\nu_{\text{rf}}t)(z\vec{e_\rho} - \rho\vec{e_z})\right] \tag{3.30}$$

where $\mathcal{E}_0$ is the gradient of the applied field. Tuning of $\nu_{\text{rf}}$ to $\nu_+ - \nu_z$ couples the axial and the modified cyclotron modes, and tuning to $\nu_z + \nu_-$ results in a coupling of the axial and the magnetron modes. Hereafter, we treat the cyclotron-axial coupling as an example.

The axial component of the coupled mode is obtained as [10]

$$\begin{aligned} z(t) &= z_0 \cos\left(\frac{\Omega_0}{2}t\right)\sin(2\pi\nu_z t) \\ &= \frac{z_0}{2}\left[\sin\left(2\pi\left(\nu_z + \frac{\Omega_0}{4\pi}\right)t\right) + \sin\left(2\pi\left(\nu_z - \frac{\Omega_0}{4\pi}\right)t\right)\right] \end{aligned} \tag{3.31}$$

[2]For rf excitations, Rohde & Schwarz SMB100A is used. This signal generator is used to apply rf excitations hereafter in this thesis.

where the resonant Rabi frequency $\Omega_0 := q\mathcal{E}_0/(4\pi m\sqrt{\nu_z\nu_+})$, defined by the field gradient $\mathcal{E}_0$. Eq.(3.31) indicates that two frequency components are detected in the signal of the axial detector during the irradiation of the rf field. In fact, the dip signal due to the axial motion of the particle on the detector signal are split to form the so-called *double-dip*, with the frequencies

$$\nu_l = \nu_z - \frac{\Omega_0}{4\pi} \tag{3.32}$$

$$\nu_r = \nu_z + \frac{\Omega_0}{4\pi}. \tag{3.33}$$

as Figure 3.8 shows.

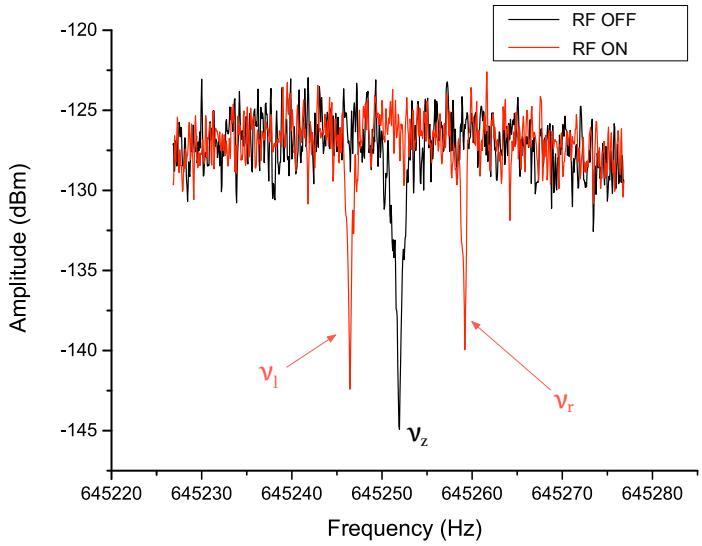


Figure 3.8: A double-dip signal due to the coupling of the axial and the modified cyclotron mode. When the rf of the frequency $\nu_{\rm rf} \approx \nu_+ - \nu_z$ is applied, the double-dip $\nu_l$ and $\nu_r$ appear in the signal.

If the frequency of irradiated rf is slightly detuned from the resonance as $\nu_{\rm rf} = \nu_+ - \nu_z + \delta$, the frequencies of the double-dip shift as

$$\nu_l = \nu_z - \frac{\delta}{2} - \frac{\Omega}{4\pi} \tag{3.34}$$

$$\nu_r = \nu_z - \frac{\delta}{2} + \frac{\Omega}{4\pi} \tag{3.35}$$

where $\Omega = \sqrt{\Omega_0^2 + \delta^2}$ is the off-resonant Rabi frequency. By adding up the two resulting frequencies one obtains,

$$\nu_l + \nu_r = 2\nu_z - \delta = \nu_z - \nu_{\rm rf} + \nu_+, \tag{3.36}$$

which enables one to obtain the modified cyclotron frequency $\nu_+$ by the measurements of the single dip $\nu_z$ and the double-dip $\nu_l$ and $\nu_r$, even if the coupling frequency is detuned.

Another important application of sideband coupling is the cooling of the energy of the radial modes. The coupling of the modes leads to an exchange of energy between different modes. Suppose that an axial detector is connected to the trap, which resistively cools the axial mode to the effective temperature of the resonator. If a radial mode is coupled to the axial mode, the radial mode loses its energy through dissipation at the axial detector. The cooling limit obtained by this process is discussed as follows. Consider the case of axial-modified cyclotron coupling. The transition between the quantum states of each mode is discussed using the energy diagram shown in Figure 3.9. Suppose the initial state of the particle to be $(n_+, n_z)$. The interaction between this state and the rf-photon of energy $\hbar(\omega_+ - \omega_z)$ can cause two transitions;

1. $(n_+, n_z) \rightarrow (n_+ + 1, n_z - 1)$
2. $(n_+, n_z) \rightarrow (n_+ - 1, n_z + -1)$.

These two processes are described with their probabilities $P_1$ and $P_2$ in Figure 3.9. The calculations of matrix elements give

$$\begin{cases} P_1 \propto \left| \langle n_+ + 1, n_z - 1 | \, a_+^\dagger a_z \, | n_+, n_z \rangle \right|^2 = n_z(n_+ + 1) \\ P_2 \propto \left| \langle n_+ - 1, n_z + 1 | \, a_+ a_z^\dagger \, | n_+, n_z \rangle \right|^2 = n_+(n_z + 1) \end{cases} \tag{3.37}$$

with the same proportional factor for $P_1$ and $P_2$. In Eq.(3.37), creation-annihilation operators $a_i^\dagger, a_i$ are used to calculate the matrix element. They satisfy

$$a_i^\dagger \, | n_i \rangle = \sqrt{n_i + 1} \, | n_i + 1 \rangle \, , \quad a_i \, | n_i \rangle = \sqrt{n_i} \, | n_i - 1 \rangle \, . \tag{3.38}$$

By comparing the probabilities $P_1$ and $P_2$, we get

$$\begin{cases} n_+ > n_z \implies P_1 < P_2 \\ n_+ < n_z \implies P_1 > P_2 \quad . \end{cases} \tag{3.39}$$

This result means that the modified cyclotron mode is cooled until $n_+ = n_z$. Consequently, the temperature of the modified cyclotron mode at thermal equilibrium $T_+$ is related to the axial temperature $T_z$ as

$$\frac{T_+}{T_z} = \frac{< E_+ >}{< E_z >} = \frac{\hbar\omega_+}{\hbar\omega_z} \frac{< n_+ >}{< n_z >} = \frac{\omega_+}{\omega_z}. \tag{3.40}$$

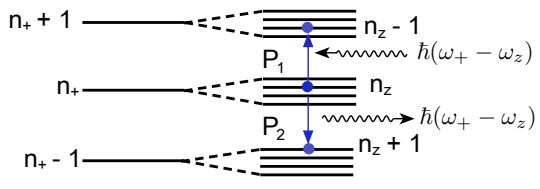


Figure 3.9: The transitions of quantum states due to the interaction with rf-photon.

The same discussion can be applied to the axial-magnetron coupling to derive the relations;

$$T_+ = \frac{\nu_+}{\nu_z} T_z, \quad T_- = \frac{\nu_-}{\nu_z} T_z. \tag{3.41}$$

Eq.(3.41) defines the temperature of a coupled radial mode when the temperature of the axial resonator is known. Note that the cooling of magnetron mode via sideband coupling decreases the quantum number of the mode, therefore make the magnetron radius small. Cooling a magnetron mode of a particle is an essential procedure to stabilize the frequency of the particle.

# Part II

# BASE Experiment

# 4. ANTIPROTON DECELERATOR

In this part, the experimental background of BASE will be described.

We shall start from the Antiproton Decelerator (AD) [6], the facility we work in, and then treat the BASE setup. The understanding of the AD as well as the setup is important especially because the AD, which is a special location for antiproton studies, adversely produces noise which can affect our measurements. In Chap.6, we shall analyze the magnetic field fluctuations which are present the AD-hall as the end of our part of experimental background.

The AD in CERN is the only facility which provides low energy antiprotons available for antimatter experiments in particle traps. This chapter gives a brief description of the system and mechanisms of the AD.

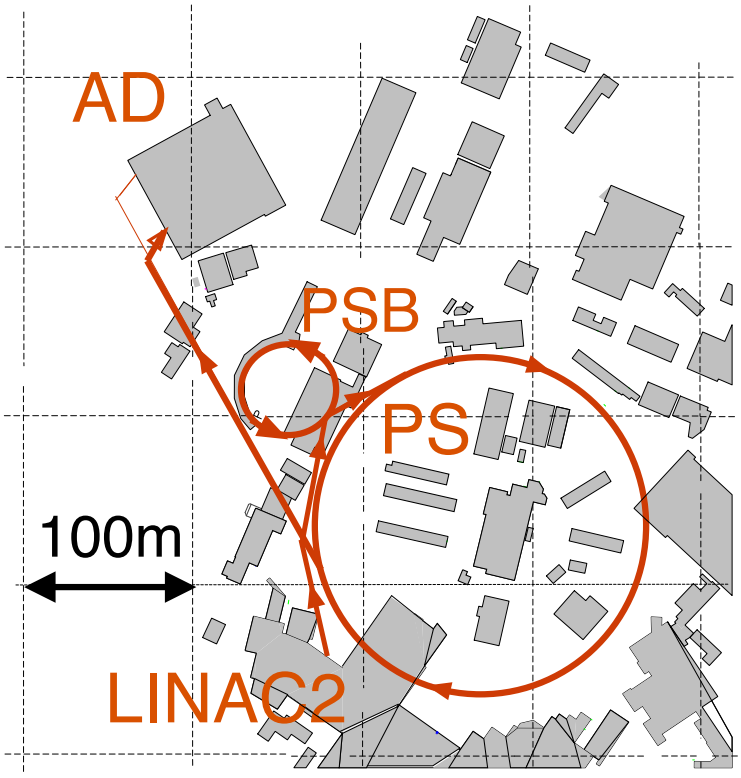


Figure 4.1: An accelerator complex of CERN from LINAC2 to AD.

Figure 4.1 shows the accelerator chain of CERN leading the AD. Protons are accelerated by a linear accelerator (LINAC2), a booster synchrotron (PSB) and a main synchrotron (PS) up to 26 GeV/$c$. This high energy proton beam is impinged on an iridium target at the injection point of the AD to produce antiprotons. In the AD target area, these antiprotons are produced, collimated and momentum-selected to prepare for their injection into the ring shown in Figure 4.2 a)[1]. A part of the AD ring and the transfer line from the production are of antiprotons can be seen in photographs of Figure 4.3 .

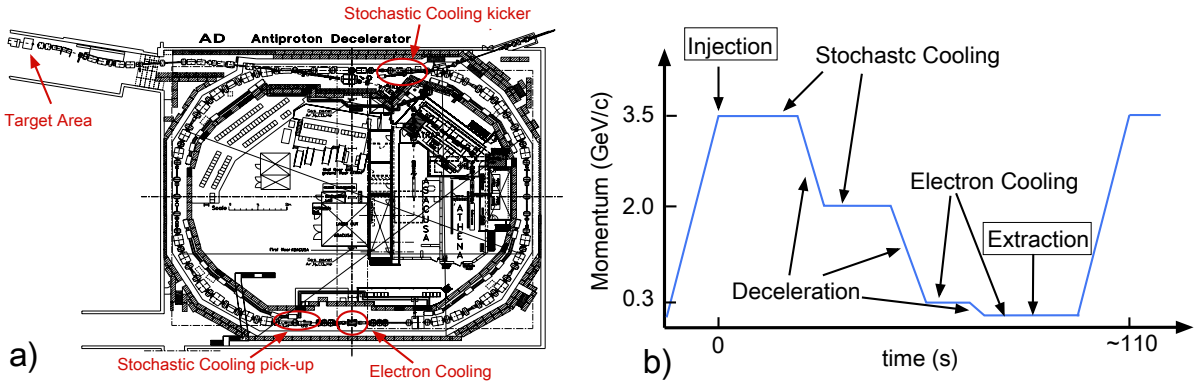


Figure 4.2: a) The layout of the AD-hall (from [6]). b) A typical cycle of the AD operation.

The antiprotons stored in the AD ring lose their energy by decelerating operation with an rf cavity. After each deceleration process, a cooling process is performed to reduce the transverse emittance and the momentum spread of the beam which are broadened by deceleration. The currents applied to the bending magnets are adjusted according to the momentum of the antiproton at each stage of deceleration.

The AD has two methods to cool antiprotons; stochastic cooling [26] and electron cooling [27]. The stochastic cooling is a method to reduce the beam emittance by applying the correction voltage according to the measured profile of the beam, which in fact a very similar to feedback-cooling which was descried in the previous chapter. The electron cooling is a cooling process to cool the antiprotons by collisions with radiatively cooled electrons. The sectors used for these cooling processes are shown in Figure 4.2 a). The AD operation cycle consists of three steps of deceleration processes followed by cooling processes as shown in Figure

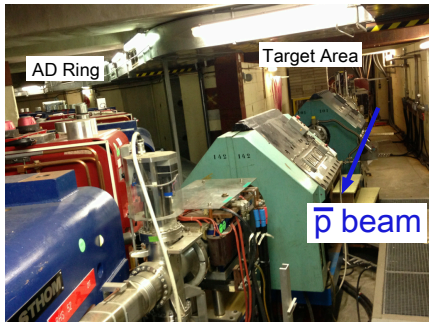


Figure 4.3: The AD ring is shown on the left hand side. The target area locates behind the concrete wall on the right hand side of the photograph.

[1]This figure was taken from an old drawing in 1999, therefore a zone of BASE is not shown.

4.2 b). The antiprotons which have momentums about 3.5GeV/$c$ (27 GeV in kinetic energy) at the production are decelerated and cooled to 100 MeV/$c$ (5.3 MeV) at the end, then they are extracted to the experimental groups as bunches of typically $3 \times 10^7$ antiprotons.

In the most part of the beamtime, the AD is operated on the cycle of Figure 4.2 b) with a typical cycle length of 110 s. We call this as a *low energy mode*. In the last week of beamtime 2014, the AD is operated on a so-called *high energy mode*. In this mode, the antiprotons are extracted in the second deceleration step, and thus the operation has a shorter cycle length of typically 80 s.

# 5. THE BASE SETUP

This chapter describes the apparatus of the BASE experiment. We shall start with an overview on the mechanical setup and the integration of the apparatus into the AD-hall. Then, the heart of the experiment is described, which consists of an advanced Penning trap system in a superconducting magnet. The advanced data logger system, which will serve for analyses in the later part of this thesis, is also introduced.

## 5.1 Integration

To apply the double trap technique which was applied to the proton [14] to the antiproton as well, the BASE experiment has been set-up at CERN within the last two years [8]. A dedicated experimental zone (DE5) and an antiproton transfer line were constructed, and implemented into the AD facility. A drawing of integration is shown in Figure 5.1.

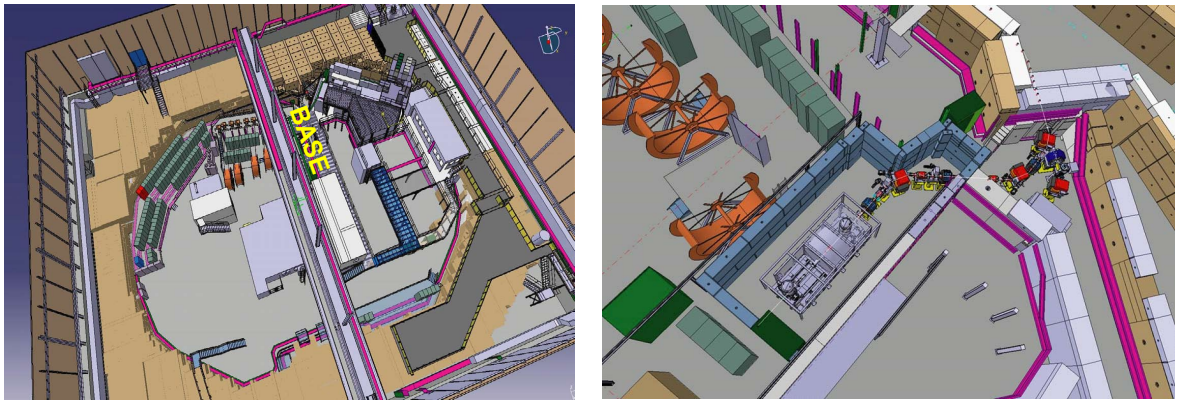


Figure 5.1: Integration of BASE into the AD-facility. Left: Overview of the AD-hall, right: detailed view of the BASE experiment.

## 5.2 Experiment Zone and Beamline

The BASE experimental zone has a length of 9.6 m and a width of 3.6 m (see Figure 5.2). It is surrounded by concrete blocks to shield the outer space from radiation generated by antiproton annihilation. A beamline from the AD ring to DE5 zone consists of bending magnets, quadrupole magnets, and corrector magnets. Its top view is shown in Figure 5.2

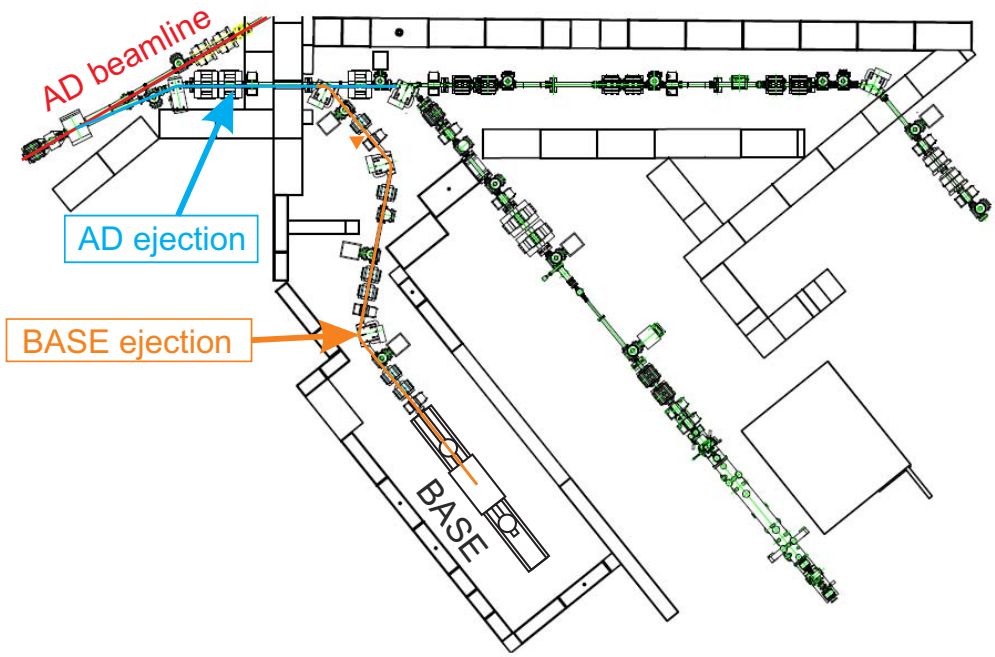


Figure 5.2: Topview of the BASE experiment zone and the beamline.

## 5.3 BASE Apparatus

Figure 5.3 shows the apparatus of BASE. The Penning trap stack is mounted in the homogeneous center of the magnet. Two cryostats operated with cryoliquids (each cryostat has a 35-l liquid Helium tank and a 35-l liquid Nitrogen tank) are mounted on the upstream and the downstream side of the apparatus. Cryogenic operation is crucial to provide long antiproton storage times and allow use of highly sensitive superconducting detection electronics for a single particle.
The heart of the experiment is

- an advanced Penning trap system consisting of four Penning traps, mounted in a hermetically sealed, pinched-off vacuum chamber with a volume of about 1 liter, which is closed by a 25 $\mu$m thick stainless steel foil,
- and superconducting detection systems for non-destructive frequency measurements.

Other key components are highly stable precision voltage sources for biasing of the trap electrodes, with an absolute voltage stability of 0.2 ppm (Stahl electronics, UM1-14), a sequence of low noise RC-filter stages at 300 K, 77 K and 4 K, as well as radio-frequency instruments as standard spectrum analyzers and rf-frequency generators. A detailed view of the experiment and its key components are shown in Figure 5.3. The upstream part of the experiment is connected to the antiproton transfer line. About 10 cm upstream of the trap-can a CMOS based cryogenic beam monitor is placed, which allows

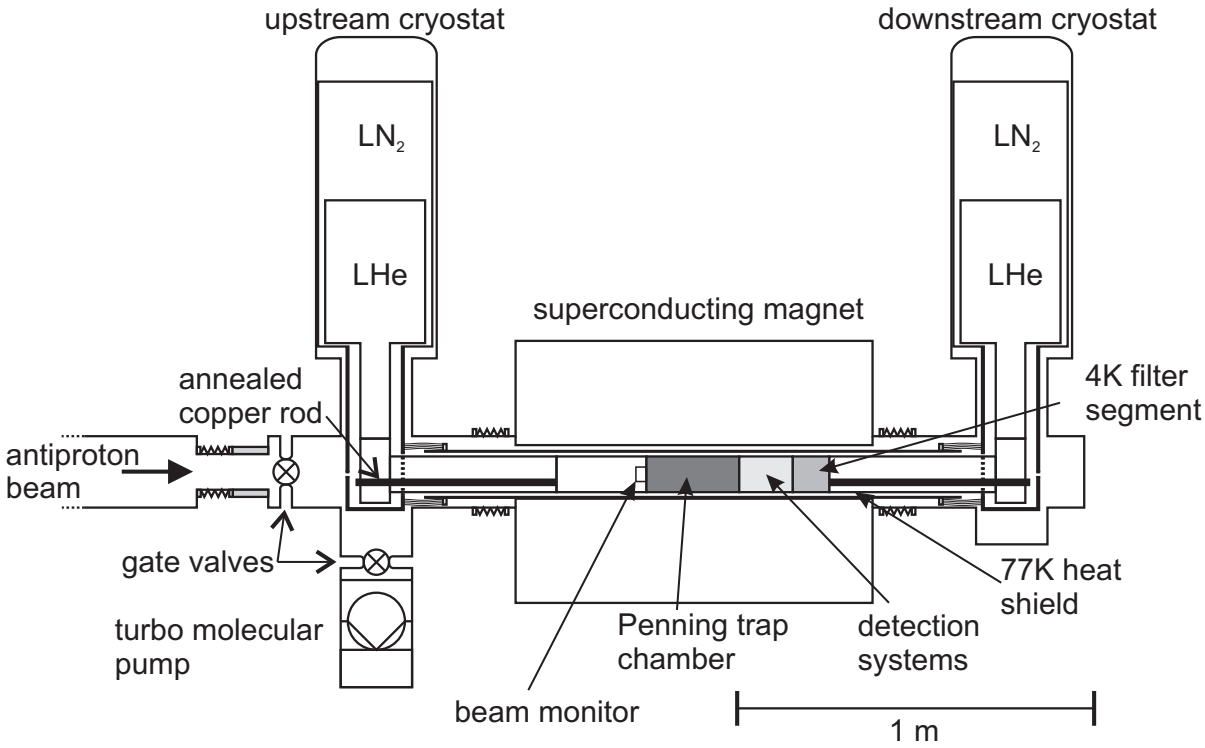


Figure 5.3: Detailed view of the BASE apparatus including the major components of the experiment. For details see text.

focusing of the antiproton beam to the center of the degrader. Downstream of the trap can a 4 K filter board is mounted, a segment including the superconducting detectors, as well as a segment including another 4 K filter stage. In order to minimize resistive losses as well as electromagnetic interference it is of importance to place the detectors close to the trap.

The 4 K parts are connected to the cold-fingers of the cryostats by means of annealed high purity copper rods with thermal conductances on the order $10^4$ W/(m·K). This entire 4 K assembly is surrounded by thermal shields connected to the liquid nitrogen reservoirs of the cryostats which reduce the heat impact on the 4 K stage by a factor of $(300/77)^4$. The power consumption of the 77 K stage is at 20 W, the consumption of the 4 K stage at 150 mW. This allows us to operate the experiment for 5 days without any external cryoliquid supplies.

## 5.4 BASE Traps

### 5.4.1 Overview of the BASE Four-Trap System

The BASE trap stack is shown in Fig. 5.4. It consists of four independent Penning traps which are all in cylindrical, compensated and orthogonal design [28]. BASE employs the double-Penning trap with a Precision Trap (PT) and an Analysis Trap (AT) . The Precision Trap is located in the homogeneous

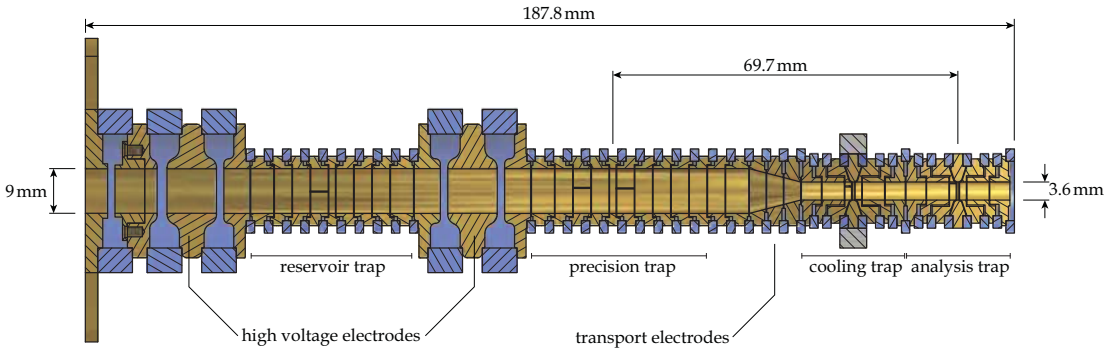


Figure 5.4: The BASE Penning trap system, which consists out of four Penning traps. For details see text.

magnetic field and realizes the high-precision frequency measurements, while the AT has a strong superimposed magnetic field mottle term to detect the spin-flip in the principle of the continuous Stern-Gerlach effect. In addition to the Precision Trap and the Analysis Trap, BASE apparatus has another two traps: a Reservoir Trap (RT) and a Cooling Trap (CT).
The Reservoir Trap serves as an antiproton reservoir. The idea is to load this trap with several AD shots and to extract single particles whenever a particle is lost in the precision experiment cycle. In this work, methods were developed to extract a single antiproton from the reservoir, without any additional particle loss.
The second trap which was added is the Cooling Trap. As described in [12], it is crucial in (anti)proton magnetic moment measurements to cool the cyclotron motion of the particles efficiently to sub-thermal temperatures. This is done by coupling the trapped particle to the cyclotron detection system which cools the particle resistively. The Cooling Trap is designed to have a small diameter which leads to small cooling-time constants, thus provides fast cooling. It will play an important roll in the planned measurements of the magnetic moments.

### 5.4.2 Antiproton Catching System

The key components to catch antiprotons provided by the AD are shown in Figure 5.5. The electron gun in Figure 5.5 is placed at downstream of the Analysis Trap. The trap stack including the electron gun is placed inside a hermetically-sealed, ultra high vacuum trap chamber (called *trapcan* in Figure 5.5). The window of the XHV flange shown in Figure 5.5 separates this ultra high vacuum region from the insulation vacuum. During the beamtime, we trapped antiprotons in one of the Penning traps and stored them for longer than four weeks. With these observations and using an estimation method of vacuum from antiproton lifetimes, the pressure inside the trap chamber is estimated to be better than $5 \times 10^{-17}$ mbar.

An antiproton bunch enter the BASE apparatus passes through the three-layer degrader structure. The detail of the design can be found in [29]. The three layers are designed in a way that they have broad acceptance range of an energy of injected antiprotons. The aluminum foil of the downstream structure of the degrader is used as a target of electrons for the proton production. Therefore, the electrode at the aluminum foil is called as the *target electrode*. Antiprotons passed through the degrader have broad range energies up to an order of MeV. According to simulations, 0.1 % out of the original

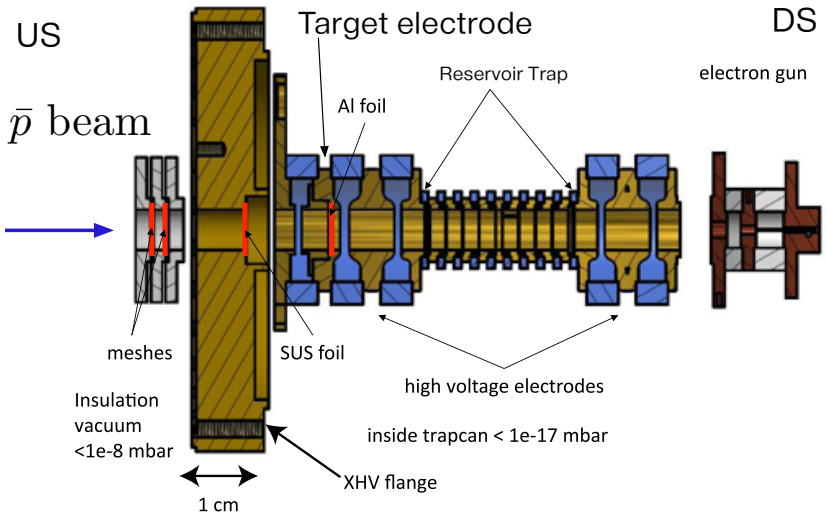


Figure 5.5: Degrader structure, an electron gun, the high voltage electrodes are shown together with the Reservoir Trap. Components between the Reservoir Trap and the electron gun are omitted from this figure.

$10^7$ antiprotons are decelerated to energies below 10 keV. This low energy fraction can be captured by the high voltage potentials applied to the electrodes on both sides of the RT.

The high voltage electrodes are connected to the high voltage supplies via switches which are triggered by a TTL signal. These high voltage potentials are ramped to several kV in a raise time of 100 - 200 ns.

After captured in the trap, antiprotons are cooled sympathetically via collisions with electrons which are prepared in the trap beforehand. The electron gun provides the electron for this purpose.

The electron gun, whose structure is show in Figure 5.6, is a tungsten made field emission tip. It is mounted close to an acceleration electrode where typically 1 kV is applied to extract electron currents of several 100 nA. The voltage at acceleration electrode decides the current radiated from the tip by field emission, while the voltage applied to the base electrode defines their energy. In Figure 5.6 a), the electron current measured at the target electrode is plotted as a function of the voltage at the acceleration electrode. The purpose of the electron gun for the antiproton experiments is to provide electrons to cool antiprotons which have high energies soon after they are captured in the RT. The electron gun can be also used for production of protons at the target electrode for a proton experiment.

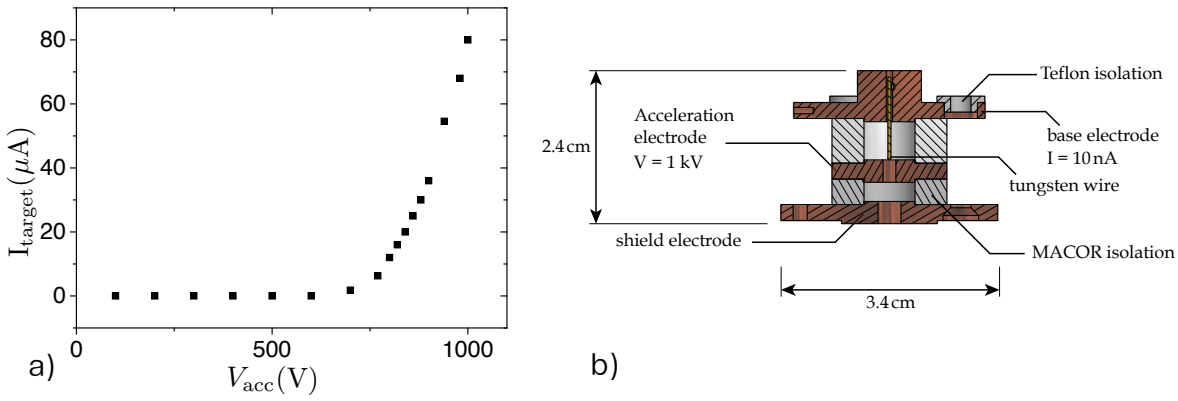


Figure 5.6: a) Performance of the electron gun. The current measured at the target electrode is plotted as a function of the acceleration voltage at the electron gun. b) Structure of the electron gun.

The trap system has been designed and assembled in a thesis by Georg Schneider [20]. I refer this document for a detailed discussion.

## 5.5 SQL-based Data Logger System

The data logger system of BASE continuously records the following log information.

- Temperatures of the apparatus inside the flanges
- Temperatures of the voltage supplies UM 1-14, connected to the trap electrodes

- Room temperature
- Ambient magnetic fields in the DE5 zone
- Vibrations of the stage of the apparatus

Among the log information, the information of magnetic fields is the most important for the experiment. The data logger system includes multiple magnetic field probes (Hall probes, flux gates and a GMR sensor) at different positions, which enable us to characterize the external fluctuations cause by crane operation, ramp of the magnets of other experiments, etc.. Figure 5.7 shows the positions of three of the magnetic field probes. Figure 5.8 demonstrates characterization of changes of the magnetic field by the multiple probes. The magnetic field is measured by three probes (a Hall probe (LakeShore Model 475) on the pole, one of the three-axis Hall probes (Metrolab THM1176) and the GMR sensor (NVE AA002-02, read by Fluke 8508A)) during transport of a liquid helium dewar. The dewar is carried from the position next to the upstream cryostat (the same position as Figure 5.7), and then moved to an upstair stage using a crane (see Figure 6.1). The effects of the chain of the crane, the dewar and the crane can be separately observed in the changes of the magnetic field at each position of the different probes as the dewar is carried above.

Detailed understanding of fluctuations caused by the AD is crucial for the planned high precision measurements. The GMR sensor included to the log-system has a sensitivity high enough to detect the operation of the AD. It will be employed to characterize magnetic field fluctuations in Chap. 6.

The acquired log information is stored on an SQL database. As described in Figure 5.9, information recorded by each device is stored on a database together with its timestamp. By referring the data from its timestamp, we can extract useful information from the database (e.g. the magnetic fields measured by multiple probes at the same time, the averaged magnetic field during each cyclotron frequency measurement).

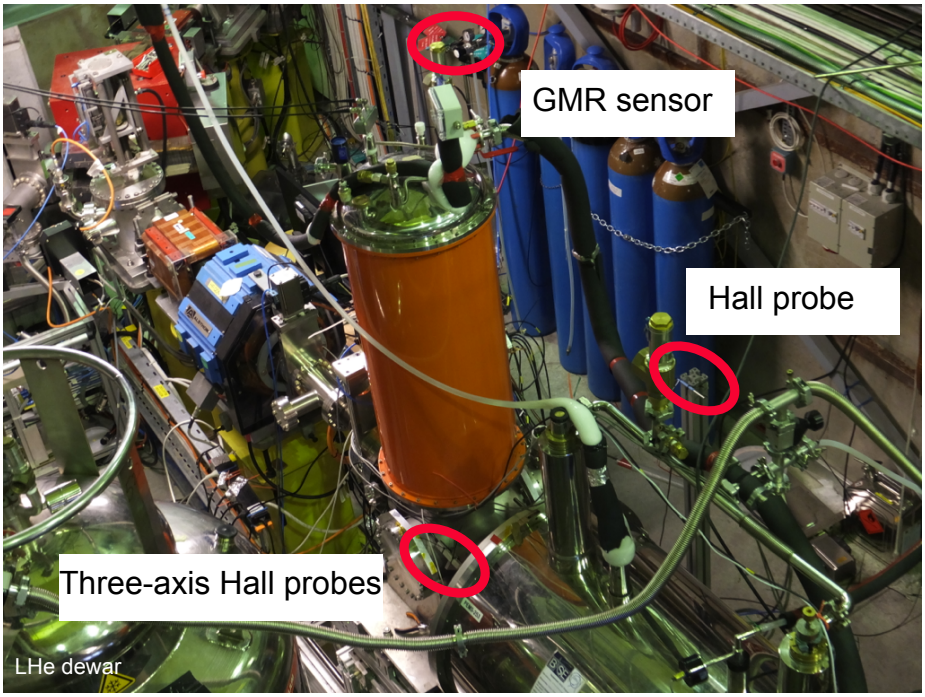


Figure 5.7: Three of the magnetic field probes: Hall probe, three-axis Hall probes, GMR sensor.

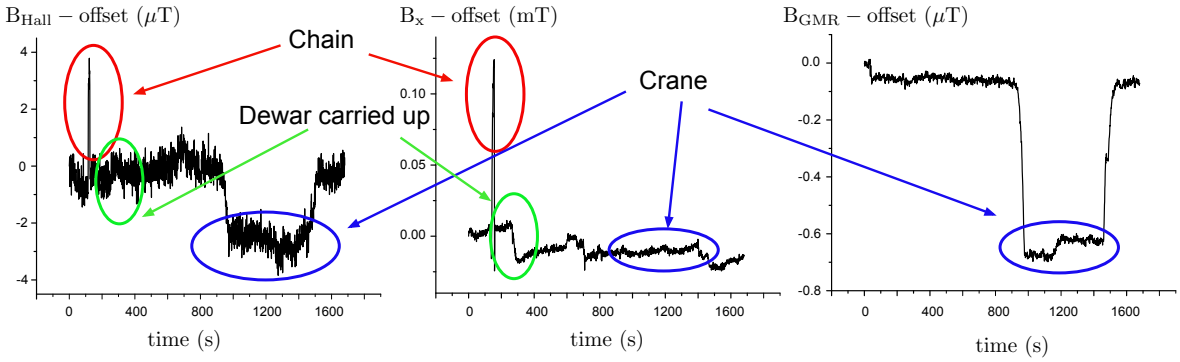


Figure 5.8: The changes of a magnetic field during transportation of a liquid helium dewar. $B_x$ stands for the magnetic field measured by an x-axis probe of the three-axis probes, which faces upward.

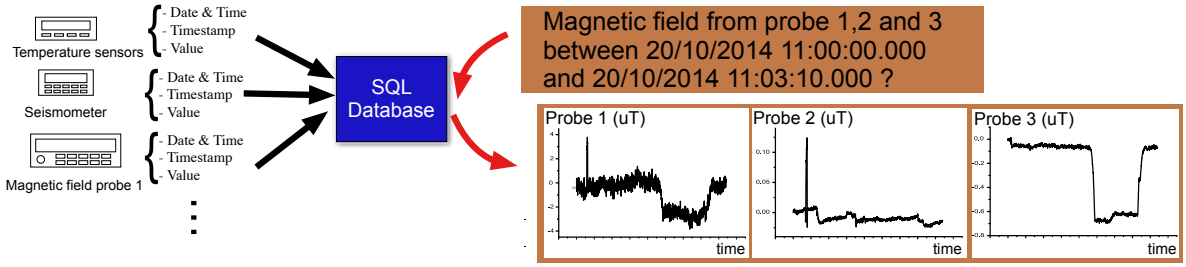


Figure 5.9: A description of an SQL database used in the BASE data logger system.

# 6. MAGNETIC FIELD NOISE IN THE AD-HALL

The magnetic field fluctuations produced in the AD hall can be crucial for the precision of the measurement. In this chapter, the results of the measurements are presented to characterize the magnetic noise.

## 6.1 Sources of Fluctuations

The following three factors are representative causes of magnetic field fluctuations in the BASE zone.

- Magnets of other experiments
  There are four other experiments which usually work in the AD-hall; ALPHA, ASACUSA, ATRAP and AEgIS. All of them use one or several superconducting magnets. Ramps of these magnets cause obvious shifts of the magnetic field.

- AD crane
  There is a crane in the AD-hall which is used for purpose such as exchanges of dewars for cryoliquid, or carrying the parts of the experiments. The crane and its chain, both are made by steel are shown in Figure 6.1. When the crane is located above or passes the BASE zone, its interaction with the field produced by the BASE magnet changes the magnetic field in the zone.

  We observe changes of the measured ambient magnetic field due to these crane operations.

- AD operation
  The AD operation produces weak magnetic field fluctuations synchronized with its deceleration-cooling cycle. This fluctuations are detected by a GMR sensor implemented in the data logger system.

Figure 6.1:
The AD crane above the experimental zone of BASE.

The results of measurements to characterize these fluctuations will be shown in the next section.

## 6.2 Magnetic Field Measurements

### 6.2.1 Measurements before the Beamtime

Before the installation of the trap apparatus, the magnetic field inside the superconducting magnetic of BASE and the ambient magnetic field are measured by an NMR probe (Metrolab NMR Precision Teslameter 2025 with Metrolab Probe 6) and a Hall probe (LakeShore Model 475) (Fiure 6.2). The purpose of these measurements is to estimate the strength of the magnetic field noise and to estimate the shielding factor of our superconducting magnet. The AD was not on operation when these measurements were performed.

In Figure 6.3, the result of the measurement was compared with the information of crane operations and activities of ASACUSA, the most neighboring experiment. We observed shifts of the ambient magnetic field of 5-10 $\mu$T due to ramps of one of the superconducting magnets of ASACUSA. When it was turned on, it ramped up gradually in about half an hour. After hours, it was ramped down in half an hour. We also observed the shifts of the magnetic field due to the crane operations, whose typical strength in the ambient field is about 2-3 $\mu$T. When the crane passed over the BASE apparatus, the magnetic field changed by this order for several minutes when it was above the apparatus, and turned back after it passed.

Due to the self-shielding properties of the superconducting magnet in persistent mode, they are reduced by a factor of 10 inside the magnet. These shifts inside the superconducting magnet, whose strength is about $1.94\,\mathrm{T}$, correspond to relative shifts in the order of $10^{-7}$.

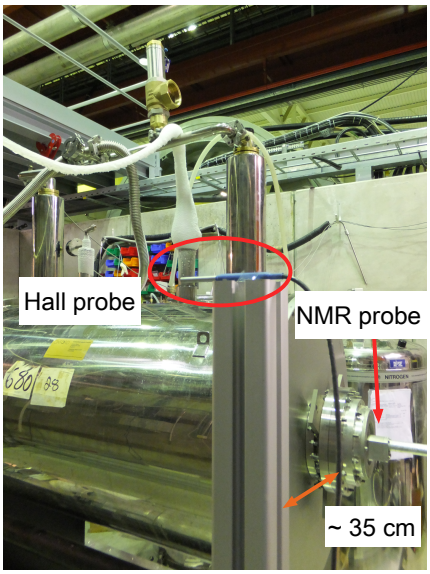


Figure 6.2:
Placement of the Hall probe and the NMR probe for the measurement before the beamtime. The Hall probe was placed on a pole which located at 35 cm from the end of the magnet. The NMR probe is at the end of the rod shown in the photograph and inserted to the homogeneous center of the magnet.

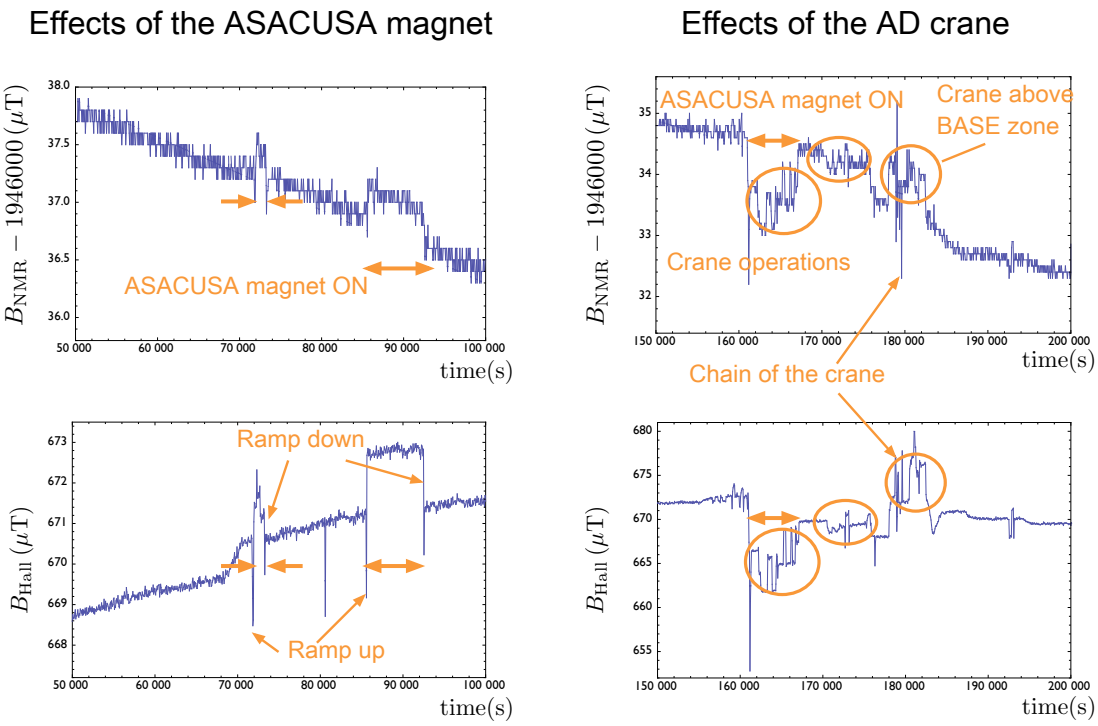


Figure 6.3: The results of the measurement performed by an NMR probe and a Hall probe. The information of the ASACUSA magnet and the AD crane are noted in the graphs.

### 6.2.2 Measurements during the Beamtime

During the beamtime, the ambient magnetic field was monitored by probes implemented in the data logger system. The magnetic field inside the magnet was derived by the modified cyclotron frequency of the particle as [1]

$$B_{\bar{p}} := \frac{2\pi\nu_+}{(q/m_{\bar{p}})}. \tag{6.1}$$

To compare the magnetic field inside and outside the magnet, the ambient magnetic field measured by the probes are averaged over the double-dip measurement of the cyclotron frequency. The jitter of the magnetic field, defined by

$$\delta B_i := B_i - B_{i-1} \tag{6.2}$$

are plotted in Figure 6.4. In Figure 6.4, several significant magnetic field shifts are observed. By referring the measurement of the Hall probe, the shifts around time 6000 s and 17500 s are identified as the crane operation and the ramp of a magnet.

$$\begin{aligned} \delta B_{\text{Hall}}/\delta B_p &\sim 8 \\ \delta B_{\text{Hall}}/\delta B_{\text{GMR}} &\sim 6 \\ \delta B_{\text{GMR}}/\delta B_p &\sim 1 \end{aligned}$$

The ratio between the Hall probe and the field inside the magnet was consistent with the shielding factor measured before the beamtime. A difference between the strength of fluctuations observed by the Hall probe and the GMR sensor is supposed to be caused by the spatial distribution of the fluctuations. For example, the magnetic field fluctuation of vertical directions at the BASE zone will be reduced at the position of the GMR sensor due to the metal stage above it (see a photograph of Figure 5.7).

The magnetic filed fluctuations produced by the AD can only be directly detected by the GMR sensor of the data logger system. As shown in Figure 6.5, the magnetic field fluctuation in the order of 100 - 200 nT are detected. They reflect the cycle of ramps of the bending magnets of the AD whose currents are periodically switched according to the momentum of circulating antiproton bunches.

[1] The absolute magnetic field estimated by this expression is differ in the order of $10^{-1}$ mT from the one defined for the free cyclotron frequency $\nu_c$. However, this definition can be employed if one is interested in the differences of the magnetic field. $\frac{\partial B}{\partial \nu_+} \simeq \frac{\partial B}{\partial \nu_c}$ stands until the order of $10^{-11}$ T/Hz

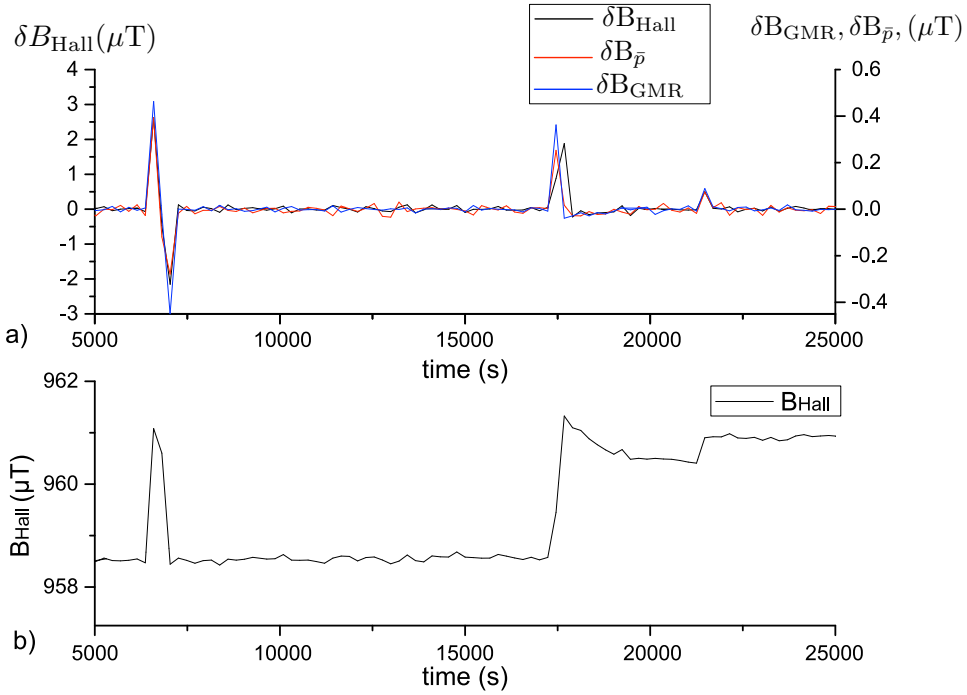


Figure 6.4: Jitters of the magnetic field measured by two probes and an antiproton trapped in a BASE trap. The magnetic field measured by the Hall probe and the GMR sensor is averaged over the cyclotron frequency measurement cycle.

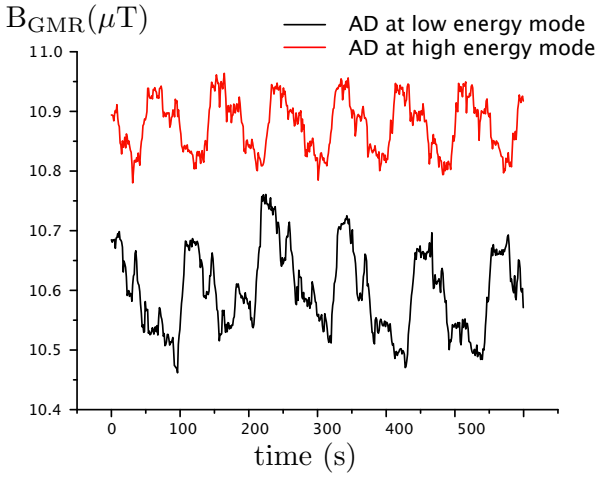


Figure 6.5: The magnetic field fluctuation detected by the GMR sensor. Two lines stand the measurements on two days with different AD operation modes.

To summarize this chapter, we shall summarize the characters of each factor of magnetic field fluctuations. Together with their strength, the order of timescales of the changes are important for the discussion in the later chapters. According to the results in Figure 6.3, 6.4 and 6.5, they are summarized as Table 6.1.

| | Strength in the ambient field | Timescale |
|---|---|---|
| Magnet of other experiments | 5-10 $\mu$T | minutes - hours |
| AD crane | 2-3 $\mu$T | minutes |
| AD operation | 100-200 nT | periodic (80 or 110 s) |

Table 6.1: A summary of the magnetic field fluctuations

# Part III

# Experimental methods

# 7. PREPARATION OF A SINGLE ANTIPROTON

In this part, we will discuss two experimental methods to prepare for measurements of the cyclotron frequency. First, we shall describe the methods to prepare a single antiproton from high energy bunches provided by the AD. Next, the method to optimize the trap parameters to minimize the trap imperfections will be described.

As mentioned in Chap.4, antiprotons are provide by the AD as bunches of 5.3 MeV energy with $10^7$ antiprotons. To perform a measurement of a single antiproton, we need to capture these antiprotons and cool them and prepare a single antiproton from them. We developed methods to perform this preparation during the beamtime 2014.

This chapter describes the procedure of preparing a single antiproton in the Reservoir Trap. A brief overview of the involved preparation steps is given in the list below.

1. Loading of electrons (Sect. 7.1)
   Electrons produced by field emission at the electron gun are loaded to the trap in order to cool antiprotons sympathetically.

2. Catching of antiprotons (Sect. 7.2)
   An antiproton bunch from the AD is decelerated by the degrader structure, and then captured using a high voltage pulses. The captured antiprotons are cooled sympathetically by interaction with the electrons prepared at the former step.

3. Cleaning of the trap (Sect. 7.3)
   The trap just after the catching of antiprotons contains contaminant particles such as ions and electrons. These contaminants are cleaned by several methods, and a clean cloud of antiprotons remains in the trap.

4. Separation of an antiproton cloud and preparation of a single antiproton (Sect. 7.4)
   A separation technique, which divides particle clouds trapped in the Reservoir Trap (RT) enables us to prepare a single antiproton in the trap, and store the rest of the antiprotons in the reservoir.

Each step is explained in detail in the following sections.

## 7.1 Loading of Electrons

Antiprotons caught in the Reservoir Trap (RT) have energies in the order of keV. They are cooled sympathetically with electrons [30] which are loaded before catching. The process of electron loading is described in Figure 7.1.

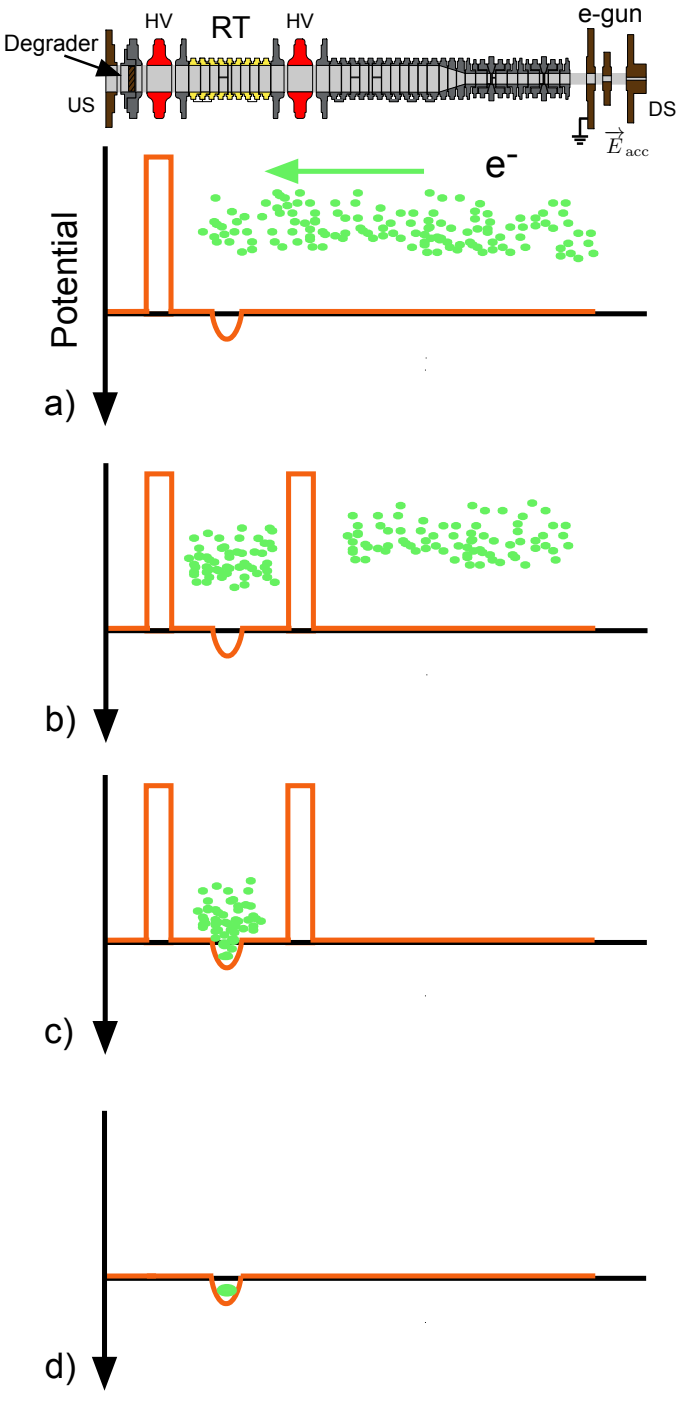


Figure 7.1: The procedure of loading electrons into the RT. For details see text.

1. The upstream high voltage electrode is ramped up to -100V to catch the electron beam produced by the electron gun. The electrons are emitted from the electron gun by field emission. A typical voltage applied to the acceleration electrode (see 5.4.2) of the electron gun is $V_{\text{acc}} = -1100V$. Figure 7.1 a).

2. A few seconds after turning on the electron gun, the downstream high voltage electrode is ramped up to close the potential well in order to capture electrons in the trap. After that, the electron gun is turned off. Figure7.1 b)

3. The electrons captured by the high voltage potential are cooled by cyclotron radiation. Figure 7.1 c)

4. After waiting for radiative cooling of the electrons, the high voltage electrodes are ramped down, and the electrons remain in the trap. Figure 7.1 d)

In the process of Figure 7.1 c), the electrons lose their energy by cyclotron radiation. The time constant of the radiative cooling is given by [17]

$$\tau_e = \frac{3\pi\epsilon_0 m_e^3 c^3}{e^4 B^2}. \tag{7.1}$$

For the 1.95 T magnet of BASE, $\tau_e$ is about 0.7 s. The electrons are cooled to the temperature of the background blackbody radiation, which is 4.2 K (corresponds to 0.36 meV). When antiprotons are caught in the RT, they lose their energy via collisions with these cooled electrons. The time constant of this sympathetic cooling depends on electron as well as antiproton densities. For typical BASE loading parameters of about 10000 electrons and 1000 antiprotons, the antiprotons are cooled within typically 10 s.

The presence of electrons in the trap appears as a frequency shift of the resonator as is shown in Figure 7.2. The large amount of the trapped electrons results in the significant frequency shift according to their number. The frequency shift observed in Figure 7.2 corresponds to 15000 electrons.

## 7.2 Catching of antiprotons

A typical antiproton bunch provided by the AD has an energy of 5.3 MeV and a pulse length of about 150 ns. According to simulations, the antiproton beam after passing the degrader is estimated to have a broad energy distribution up to 1 MeV, and its low energy tail is caught by an adequately timed pulse applied to one of the high voltage electrodes at appropriate timing. Figure 7.3 illustrates this procedure.

1. Before catching, an electron cloud is prepared in the trap, and both high voltage electrodes are ramped up to -1000 V. Figure 7.3 a)

2. The upstream high voltage electrode is pulsed down for 100 $\mu$s to catch the antiproton cloud which transmits through the degrader structure. This operation is triggered by a TTL signal which is synchronized to the AD extraction pulse. Figure 7.3 b),c)

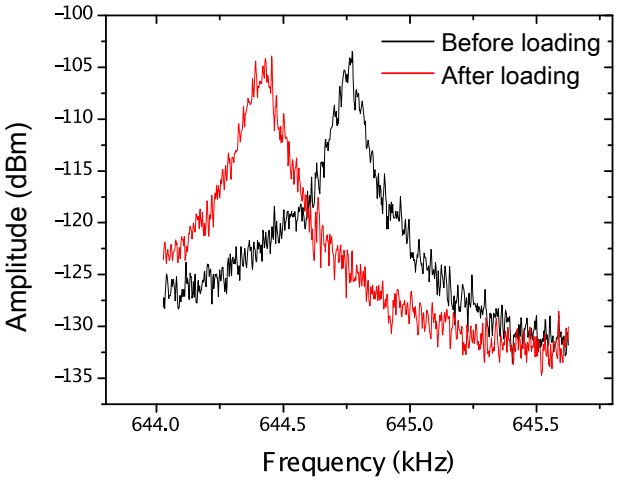


Figure 7.2: The frequency shift of the axial resonator after electron loading.

3. The captured antiprotons lose their energy by energy exchanges with the cooled electrons in the trap. Figure 7.3 d)

4. After waiting for about 10 s for the sympathetic cooling of the antiprotons, the high voltage electrodes are ramped down. Antiprotons and electrons remain in the trap. Figure 7.3 e)

A typical fraction of captured antiprotons according to the simulation is in the order of $10^{-4}$. Measurements of annihilation signals of the antiprotons by a scintillator placed at 2 m from the apparatus gives the order of caught antiprotons as $10^3$ out of one AD shot of $10^7$ antiprotons, which is consistent with the simulations.

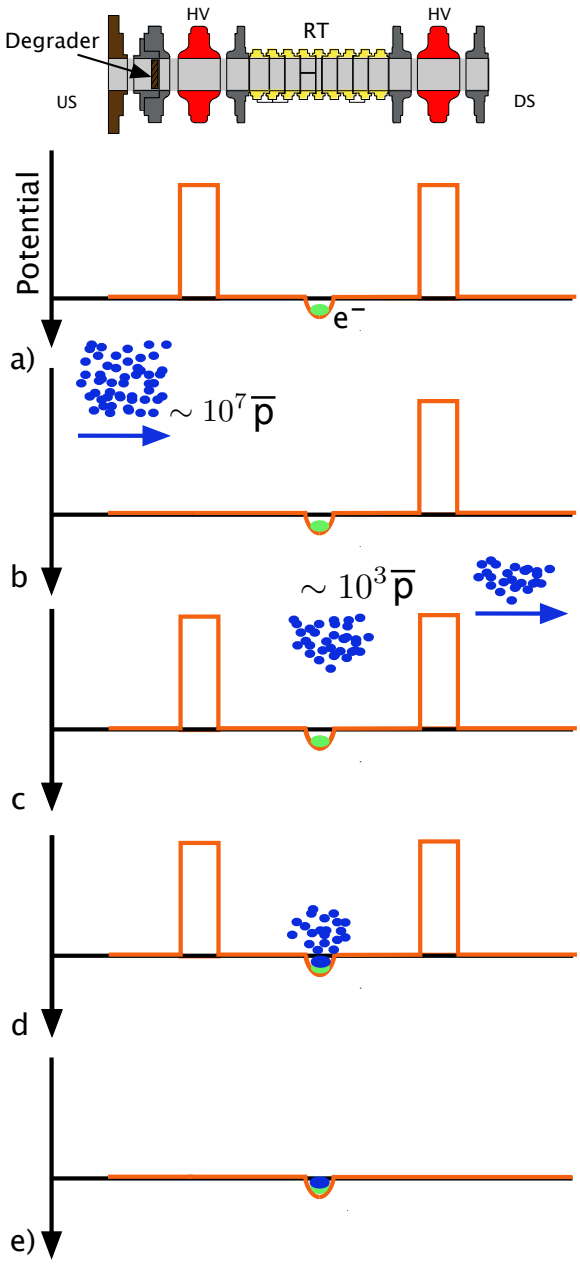


Figure 7.3: The procedure of catching an antiproton cloud provided by the AD. For details, see text.

## 7.3 Cleaning of the Trap

After catching of antiprotons, the trap contains multiple kinds of negatively charged particles; electrons and negative ions as $H^-$ ions and heavier ions as $C^-$, $O^-$, which are produced by the collision of the antiproton beam with the degrader structure. The existence of these contaminants perturb the electric potential experienced by the antiprotons. The Coulomb interaction between the antiprotons and these contaminants shifts the eigenfrequencies of the antiprotons as well. This section describes methods which are used to remove these contaminant particles from the trap.

### 7.3.1 The Cleaning Methods

Figure 7.4 illustrates a basic idea for the cleaning. The procedure is to selectively excite the target particles by rf radiation, then ramp down the trapping potential for a short time to evaporate the hot particles. The segmented correction electrode R2 (see 3.3)is used to apply the excitation signal. During these operations, a positive voltage is applied to the electrode at the target to attract the particles come out from the trap.

The methods to selectively excite each kind of particles are explained in this section. Table 7.1 lists the calculated results of the eigenfrequencies of each particle for the typical trap parameters ($C_2 = -18394.8\,\mathrm{m}^{-2}$, $B = 1.946\,\mathrm{T}$, $V_0 = 4.664499\mathrm{V}$ ).

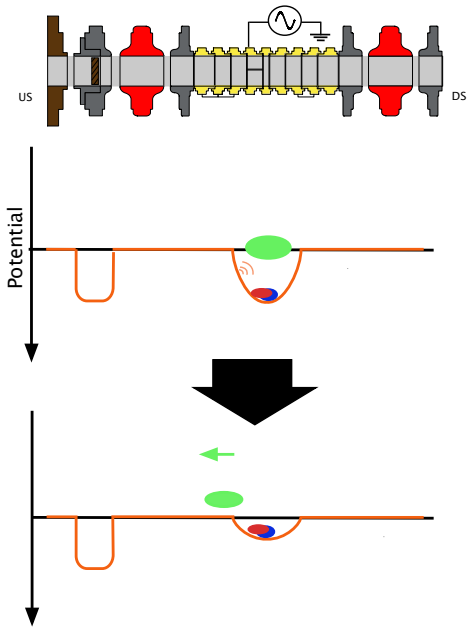


Figure 7.4: The idea of cleaning the trap. Targeted particles are selectively excited by applying an rf signal. A positive voltage is applied to the degrader to remove excited particles.

| | Axial frequency $\nu_z$ | Modified cyclotron frequency $\nu_+$ | Magnetron frequency $\nu_-$ |
|---|---|---|---|
| $e^-$ | 27.65 MHz | 54.47 GHz | 7.017 kHz |
| $\bar{p}$ | 645.3 kHz | 29.66 MHz | 7.019 kHz |
| $H^-$ | 644.9 kHz | 29.62 MHz | 7.019 kHz |
| $C^-$ | 186.9 kHz | 2.481 MHz | 7.037 kHz |
| $O^-$ | 161.9 kHz | 1.861 MHz | 7.043 kHz |

Table 7.1: The calculated eigenfrequencies of the possible trapped charged particles. $C^-$, $O^-$ are listed as representatives of the heavier ions.

- Heating of electrons
  By tuning the excitation frequency to the axial frequency of the electron, we can selectively excite the axial motion of the electrons. During the excitation, the depth of the trap potential is lowered to several volts for a short time, in order to remove the heated electrons.

- $H^-$ ion cleaning
  Since the axial frequency of the $H^-$ ion and the antiproton are close, the excitation of the modified cyclotron mode is used to selectively clean $H^-$ ions. After the cyclotron excitation, the trapping potential is ramped down to small voltages. Heated particles escape from the trap by mode coupling.

- Ion cleaning using SWIFT
  SWIFT (Stored Waveform Inverse Fourier Transform) is a technique to produce a broad band noise signal in a defined frequency span. Thereby, a band excitation which includes the axial frequencies of the contaminant ions, but excludes the eignenfrequencies of the antiproton, can be applied. While applying SWIFT drives, the antiprotons are tuned to resonance with the detector by adjusting the trapping voltage, which ensures permanent cooling of the antiprotons while other particles are heated.

After each step of the procedure, sideband cooling of the magnetron mode is performed in order to decrease the magnetron radii of the antiprotons and prevent them to be lost from the trap. In application, sweeping the frequency of magnetron coupling in the range of several hundreds Hz is effective to cool the fraction of the particles which are on large magnetron radii. Figure 7.5 shows the resonator signal while the magnetron cooling sweep is applied. Together with the excitation signal itself, which is swept to lower frequency, we can see the signal of antiprotons whose resonant magnetron-axial coupling frequencies are shifting to lower frequency as they are being cooled.

Because of their large number in the trap and fast cooling time, it is difficult to remove all electrons from the trap by rf drives. Thus, so-called the *electron kick-out* method is used for the more effective removal of electrons. As illustrated in Figure 7.6, electrons are removed from the trap by a short pulse of a step-like potential. The difference in mass between electrons and the other particles gives lower acceleration to antiprotons and the heavy ions, which enables us to remove the electrons while keeping the antiprotons trapped.

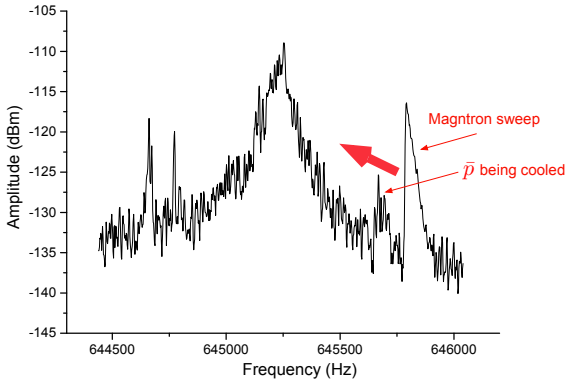


Figure 7.5: An FFT spectrum recorded during a sweep of the magnetron sideband drive frequency from higher to lower frequency.

1. The trapping potential is deepened, and then the particles are transported to the edge of the RT. The voltage at the target electrode of the degrader is ramped down to attract kicked-out electrons. Figure 7.6 b).

2. The step-like potential is created. The particles stay at the upstream edge of the sloped potential well. Figure 7.6 c).

3. The potential wall at the upstream high voltage electrode is pulsed down for short time. The potential well is closed again before the antiprotons escape from the trap. Figure 7.6 d).

4. The remaining particles are transported back to the center of the trap and the potential is lowered as before.

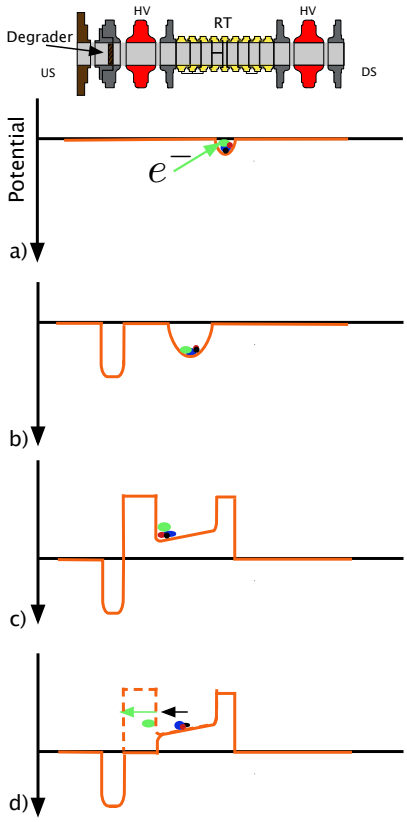


Figure 7.6: Illustration of the electron kick-out scheme. Blue, red, green, black particle clouds respectively represent antiprotons, $H^-$ ions and heavy ions such as $C^-$. During the procedure of electron kick-out, the target electrode is positively biased to attract the outgoing electrons.

### 7.3.2 The Overall Cleaning Procedure

This section describes the overall cleaning procedure. A typical cleaning procedure to remove all the particles from the RT except antiprotons is listed below.

1. Figure 7.7 a) is a spectrum of a resonator signal soon after catching of antiprotons. Presence of a large number of electrons screen the potential experienced by the antiprotons, therefore shifts the eigenfrequencies of the particles. Therefore, signals from antiprotons are not observed in the resonator signal.

2. Electrons are removed by selective excitations of their axial modes. After removing the electrons, signals from the other trapped particles appear in the spectrum. In Figure 7.7 b), signals from $H^-$ ions and antiprotons are observed.

3. The technique of the electron kick-out is applied for the further removal of electrons.

4. Cleaning of $H^-$ is performed. Figure 7.7 c) and Figure 7.6 d) are taken to confirm the removal. They are measured by detuning the trapping potential and detecting direct peak signals from antiprotons and $H^-$ ions. We can see that the peak from $H^-$ ions are gone after the cleaning procedure. A large number of particles enables us to observe the direct signal of the axial oscillation of the particles.

5. Heavy ions are cleaned by SWIFT excitations.

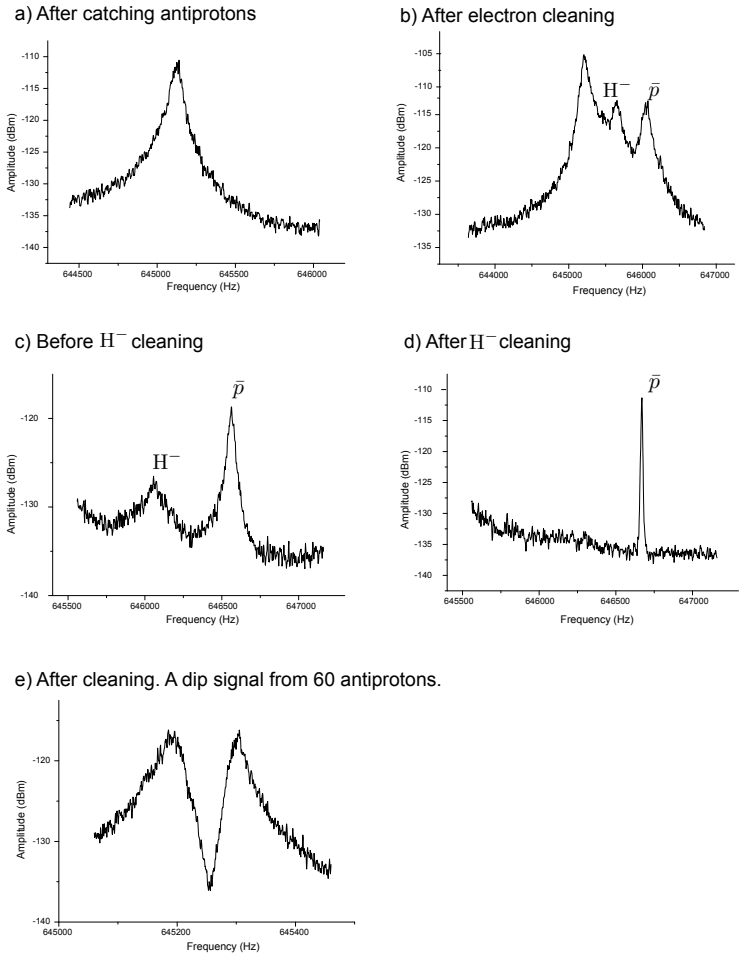


Figure 7.7: Spectra measured during the overall cleaning procedure.

Each step of the procedure is repeated until a pure antiproton cloud is prepared. In the end, we get a clear and stable signal of antiproton dip as shown in Figure 7.7 e). The number of the antiprotons of

this cloud is estimated to be about 40 according to Eq.(3.21).

## 7.4 Separation of a Particle Cloud

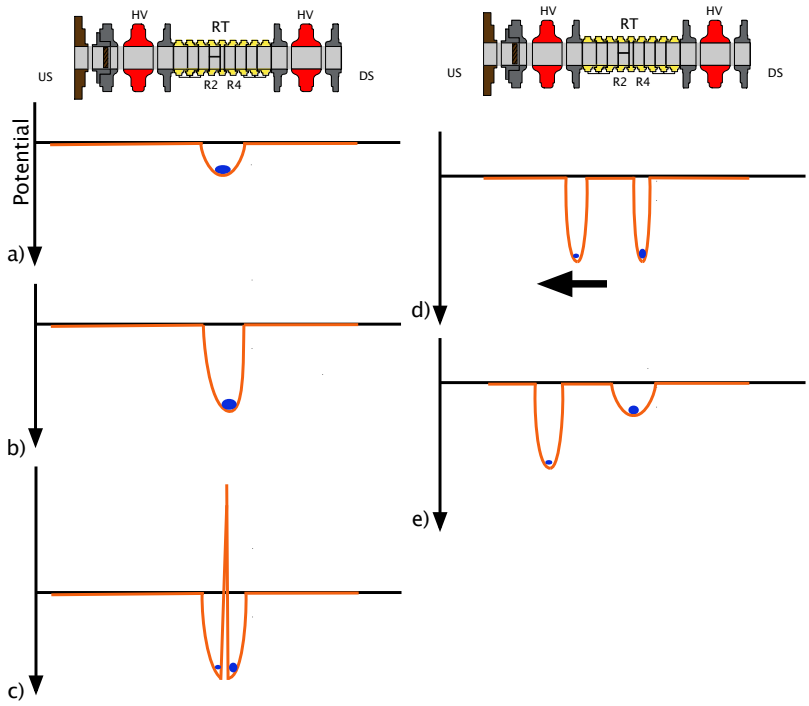


Figure 7.8: Illustration of the particle separation procedure. The ring electrode is used as a potential tweezer, which can separate a fraction of only a few precent from the antiproton cloud. The process can also reversed to merge two clouds. For details see text.

We developed a scheme to separate and merge a particle cloud by using potential ramps. Figure 7.8 illustrates the procedure to separate a particle cloud. A particle cloud in the trap is separated, then one of its fractions is parked at the high voltage electrode while the other fraction remains in the RT. By adjusting the asymmetry of the potential at step b) in Figure 7.8, the fraction of the particles after the separation can be controlled. We tested this method with a procedure shown in Figure 7.9 a). A cloud of about 60 antiprotons is prepared for this measurement.

First, the number of particles in the cloud before separation was evaluated from its dip width. Next, the cloud of antiprotons is separated into two fractions, the upstream cloud and the downstream

cloud. Then the number of antiprotons in each cloud is counted by loading it to the trap and evaluating the dip width. The fraction of the particles is evaluated by taking the ratio of a dip width of the cloud with that of the original 60-antiproton cloud. When the particles are transported, the magnetron modes of the particles are cooled before the dip widths are measured.

This procedure is repeated for different voltages at R4 at the step of separation. As a result, the fraction of each cloud after separation is obtained as a function of $V_{\mathrm{R4}}$ as shown in Figure 7.9 b). During the repetition of the measurements, the voltage of R2 at separation is fixed to 13.5 V.[1] After each set of the procedure, the clouds are merged and the next procedure starts from counting the number of the total antiprotons.

The both ends of the plot in Figure 7.9 b) is important for application. The spectrum of the signal from the downstream cloud at $V_{\mathrm{R4}} = 12.9\,\mathrm{V}$ is shown in Figure 7.10. Its dip width, which is about 1.8 Hz, corresponds to a single antiproton derived by Eq.(3.21) and the known properties of the detection system.[2] By choosing the offset voltage at R4 as $12.9\,\mathrm{V}$ or $13.5\,\mathrm{V}$, we can prepare a single particle in the trap and keep the rest of the antiprotons at the particle reservoir in another trap.

Note that the measurement in Figure 7.9 b) was carried out separating and merging the same antiproton cloud in about 50 cycles. No particle loss has been observed during the entire measurement sequence.

[1] The fact that a value of $V_{\mathrm{R4}}$ which gives an even separation is larger than $V_{\mathrm{R2}} = 13.5\,\mathrm{V}$ is explained by an offset potential on the electrode R4. This effect will be discussed in detail in the next chapter.

[2] The dip width corresponds to a single antiproton is confirmed by the following measurement: a cloud of several antiprotons was prepared and evaluation of the dip width and an rf excitation of antiprotons were repeated in turn. By this procedure, we counted the dip width of the particle clouds while we removed antiprotons one by one. The dip width of a single antiproton obtained by this measurement is used for other cases when we estimate the absolute number of antiprotons contained in a cloud.

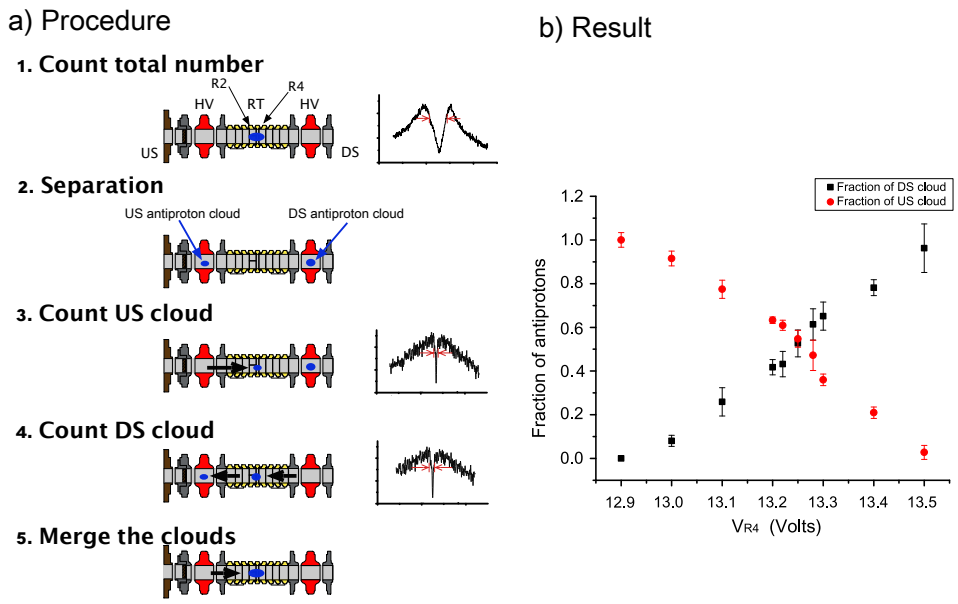


Figure 7.9: The procedure and the result of the sweep of a separation parameter. The procedure a) is repeated for different voltages which are applied to R4 at the time of separation.

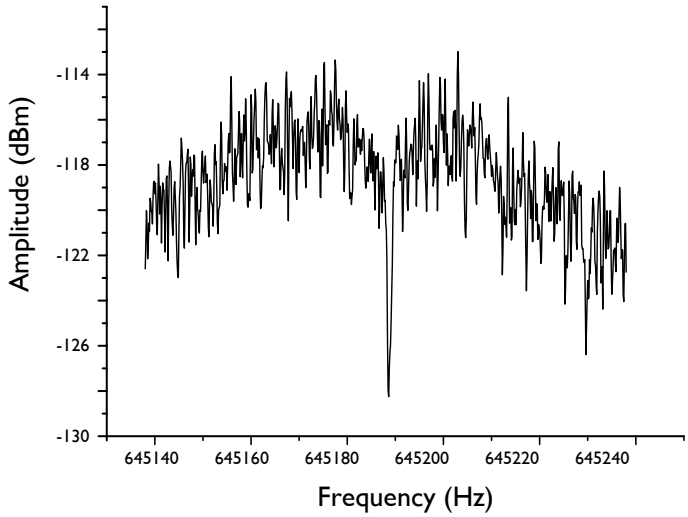


Figure 7.10: The spectrum of the downstream cloud when the voltage at separation is set to be $V_{\mathrm{R4}} = 12.9\,\mathrm{V}$.

## 7.5 Swapping of Two Particles

Our methods in operating the trap potential enables us to transport the particle reliably from one trap to another trap. We apply this technique to swap two particles between the high voltage electrodes and the RT. This transport procedure was repeated several 1000 times with no particle loss.

The procedure of swapping is shown in Figure 7.11. Prior to this procedure, we need to prepare the clouds of the particles, perform cleaning and prepare single particles using the separation method. Particles are transported in the same way as a separation procedure, and loaded alternately into the trap. The time needed for switching the particles is 18 s. This fast transportation minimizes the expected magnetic field fluctuations for the planned g-factor measurement.

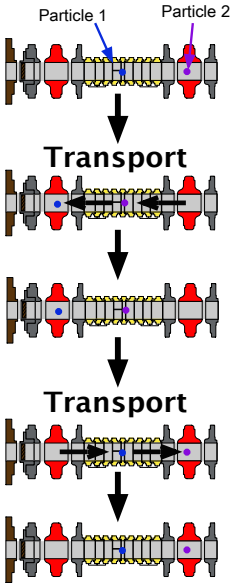


Figure 7.11: The swapping of two particles.

# 8. TRAP OPTIMIZATIONS

A single antiproton prepared in the trap is not enough to start the measurement. We need a step to optimize the trap in order to minimize the imperfection of the trap. The system of the five-electrode Penning trap, whose principle has been discussed in Sect. 2.2, is taken advantage for this purpose. In this chapter, the methods to tune the trap parameters close to the ideal state are described in the case of the Reservoir Trap.

## 8.1 Tuning Ratio optimization

### 8.1.1 Harmonicity Tuning

If the tuning ratio is not optimized, a large quadrupolar potential term $C_4$ is present. This is directly reflected in the observed frequency-dip signals. This feature is used to perform harmonicity tuning at the level of $10^{-4}$ in the units of the tuning ratio. As derived in Eq.(3.19), the particle interaction with the detector appears on the signal of the detector as an inverse Lorentz-like peak. Energy fluctuations of $dE_z$ obey the Boltzmann distribution of the temperature of the detector $T_z$ when the axial mode of the particle is thermalized.

If the trap is not well optimized, and the frequency shift due to $C_4$ (Eq.(2.23)) is present, then $C_4$ is coupled to the energy fluctuations of $E_z$. This leads to broadening of the dip signal as well as to a reduction of the depth of the frequency dip. The line shape of the dip is expressed by the convolution of a Lorentz function and a Boltzmann distribution as

$$\chi(\omega) = \frac{A}{\pi k_B T_z} \int_0^\infty dE_z \exp\left(-\frac{E_z}{k_B T_z}\right) \frac{\gamma_z/2}{\left(\omega - \omega_z\left(1 + \frac{3}{4}\frac{C_4}{C_2^2}\frac{E_z}{qV_0}\right)\right)^2 + \gamma_z^2/4}. \tag{8.1}$$

Therefore, by sweeping the tuning ratio and compare the depth of the dip signals, one can obtain the approximate optimized tuning ratio. The result of this measurement is shown in Figure 8.1. In Figure 8.1 a), depths of the dip for the different tuning ratios are plotted. A spectrum for each datapoint of Figure 8.1 a) are shown in Figure 8.1b). This result suggests that the optimized tuning ratio is between 0.8674 and 0.8680.

### 8.1.2 Precise Tuning by Magnetron Excitations

After obtaining the rough range of the optimized tuning ratio, more precise tuning is performed to the trap. As explained in Sect.2.3, the imperfection of a Penning trap causes the shifts of the eigen-frequencies depending on the energies of the eigenmodes according to Eq.(2.23) and Eq.(2.26). This effect is used to optimize the tuning ratio by changing the magnetron radius in a controlled way. The

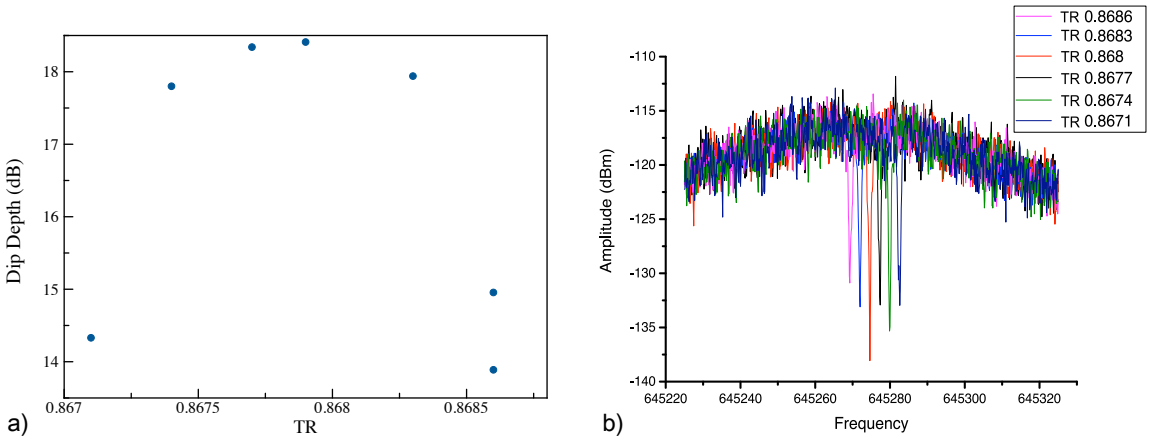


Figure 8.1: a) The result of a sweep of the value tuning ratio. The maximum of the dip depth is given by a TR around 0.868. b) A spectrum of a dip signal for each tuning ratio is shown.

shift of the axial frequency according to the magnetron energy of the particle is expressed using the magnetron radius $\rho_-$ as

$$\begin{aligned} \left.\frac{\Delta\nu_z}{\nu_z}\right|_{z_0,\rho_+} &= -\frac{3}{2}\frac{C_4}{C_2}\rho_-^2 + \frac{15}{16}\frac{C_6}{C_2}[(-6z_0^2+12\rho_+^2)\rho_-^2 + 3\rho_-^4] \\ &\simeq -\frac{3}{2}\frac{C_4}{C_2}\rho_-^2 + \frac{45}{16}\frac{C_6}{C_2}\rho_-^4, \end{aligned} \tag{8.2}$$

where $\rho_+$ and $z_0$ are the the radius of the modified cyclotron mode and the amplitude of the axial motion, respectively. The hierarchy $\rho_+ \ll z_0 \ll \rho_-$ is used to derive the approximate relation.

By applying burst signals through the excitation line connected to the segmented electrode of the trap, we can excite the magnetron mode of the particle. The radius of the excited magnetron mode $\rho_-$ is known to be proportional to the number of the cycles of the applied burst signals. By fixing the tuning ratio and increasing the number of the cycles, the axial frequency shift which corresponds to Eq.(8.2) is measured as a function of the number of the cycles of the burst signals. By defining $\alpha$ as a proportionality factor between $\rho_-$ and the burst cycle number $N$, Eq.(2.31) is denoted as

$$\left.\frac{\Delta\nu_z}{\nu_z}\right|_{z_0,\rho_+} = -\frac{3}{2}\frac{C_4}{C_2}(\alpha N)^2 + \frac{45}{16}\frac{C_6}{C_2}(\alpha N)^4 \tag{8.3}$$

In Figure 8.2 a), the result of this measurement with a single trapped antiproton is presented. The frequency of the signal is set to the frequency of the magnetron frequency $\upsilon_-$, and the amplitude of the burst signals are set to -23 dBm at the output of a signal generator (Agilent 33522A). For the measurement of each datapoint in Figure 8.2, the magnetron energy was cooled by sideband cooling, and then excited by the burst signals. The asymmetry of the trapping potential is compensated before the measurement. The voltage at the ring electrode R3 is set to 4.664499 V during the measurement sequences.

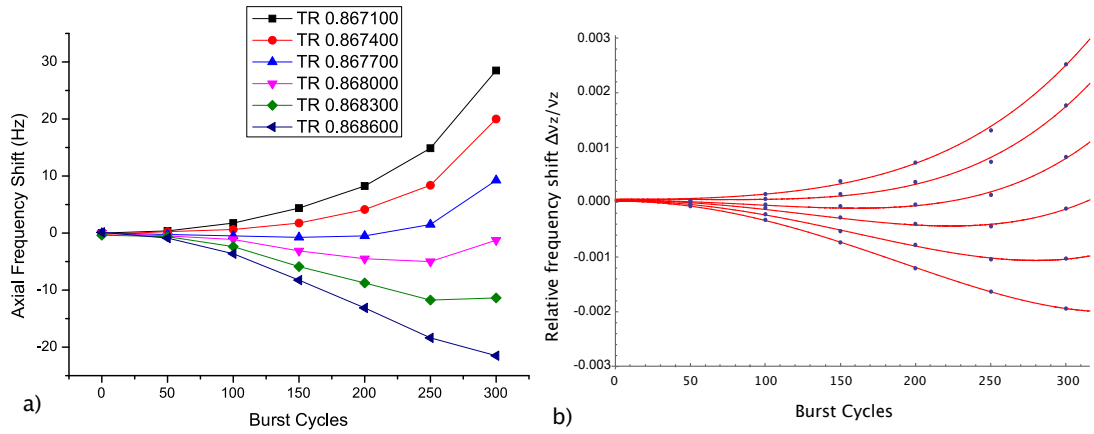


Figure 8.2: a) The shifts of the axial frequency $\Delta\nu_z$ as functions of the cycle numbers of the burst excitation signal for different tuning ratios. b) $\Delta\nu_z/\nu_z$ is fitted by a polynomial function).

As shown in Figure 8.2 b), $\Delta\nu_z/\nu_z$ is fitted by a polynomial function

$$\frac{\Delta\nu_z}{\nu_z}(N) = a_0 + a_2 \cdot N^2 + a_4 \cdot N^4. \tag{8.4}$$

The fitting coefficients are related to Eq.(8.3) by

$$a_2 = -\frac{3}{2}\frac{C_4}{C_2}\alpha^2, \quad a_4 = \frac{45}{16}\frac{C_6}{C_2}\alpha^4. \tag{8.5}$$

The fitting coefficients $a_2$ is plotted for different tuning ratios in Figure 8.3 a). If one fits $a_2(\mathrm{TR})$ by a linear function, the intersection of a fitting function and the x-axis gives the optimized tuning ratio which attains $a_2 = 0 \iff C_4 = 0$. The optimized tuning ratio according to this measurement is 0.867342(17).

The calculated value of $D_4$ is used to extract $C_6$ from $\alpha$ for the optimized tuning ratio. The validity of this method depends on the robustness of the coefficient $D_4$, which is not affected by the accuracy of the ring voltage or the tuning ratio as far as the end cap electrodes are grounded.[1] The uncertainty of $D_4$ due to the existence of a residual asymmetry of the potential is estimated in Figure 8.3 b) by assuming the existence of a voltage drop[2] at one of the correction electrodes. By comparing this result with a typical value of a voltage drop, which is tens of millivolts, we can confirm that the calculated value of $D_4$ has enough accuracy. If we define the derivative of $a_2(\mathrm{TR})$ as $\beta$, $\beta$ is related to other coefficients as

$$\beta := \frac{d}{d\mathrm{TR}}a_2(\mathrm{TR}) = -\frac{3}{2}\frac{D_4}{C_2}\cdot\alpha^2 \quad \Longrightarrow \alpha^2 = -\frac{2}{3}\frac{C_2}{D_4}\cdot\beta. \tag{8.6}$$

[1] This can be verified by the expression of $D_4$ using Eq.(2.17).
[2] This effect will be discussed in more detail in the next section.

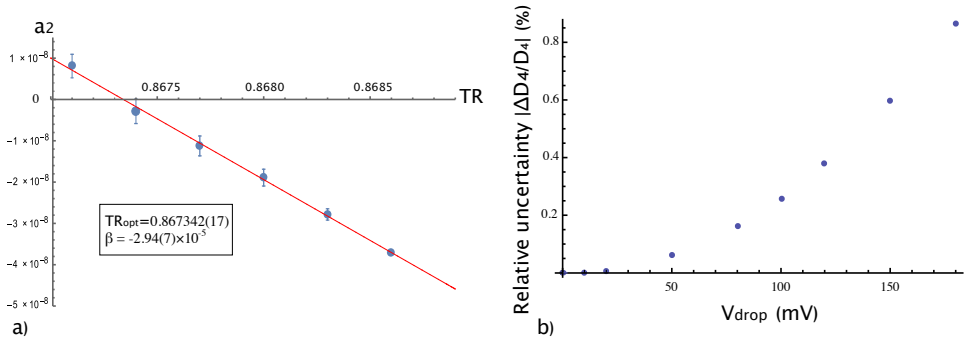


Figure 8.3: a)The dependency of the fitting coefficients $a_2$ on the tuning ratio. The x-intercept of the linear fitting function gives the optimized tuning ratio. The slope of the fitting function gives the parameter $\beta$ from which $\alpha$ is extracted. b) The estimation of the uncertainty of $D_4$ according to the calculation. For each datapoint, $\Delta D_4$ is calculated by assuming an existence of a certain value of $V_{\mathrm{drop}}$.

The value of $C_2$ is derived from the axial frequency without the burst signals. $\beta$ is derived from the result of fitting in Figure 8.3 a). By substituting these coefficients to Eq.(8.6), $\alpha$ is obtained to be

$$\alpha = 16.2(2)\mu\mathrm{m/cycle}. \tag{8.7}$$

By using this value of $\alpha$, the upper limit of the residual $C_6$ for the optimized trap is estimated as

$$C_6(\mathrm{TR_{opt}}) = 0 \pm 844\,\mathrm{m}^{-6}. \tag{8.8}$$

The uncertainty of $C_6$ is evaluated by the uncertainty of the linear fitting of $a_4(\mathrm{TR})$, which gives an estimated upper limit of $|C_6|$.

## 8.2 Asymmetry Compensation

As we mentioned in Chap. 3, one of the correction electrodes (R4) of the RT is connected to the resonator. There is a voltage drop for the trapping voltage at this electrode due to a leakage current via the connection to the resonator. This voltage drop is in an order of tens of millivolts. Consequently, if we set the same voltage to R2 and R4, the voltage at R2 becomes smaller than that at R4. To obtain the symmetric potential, an appropriate value of the offset voltage should be applied to R4. By tuning this offset value, we can tune the trap to have a symmetric potential.

The asymmetry of the trapping potential results in the shift of the axial frequency $\nu_z$ of the trapped particle. This effect is employed for the tuning of the offset value. The mechanism of the frequency shift is discussed in the following.

If the trapping potential is not symmetric, the potential minimum is shifted from the geometrical center of the trap. Therefore the series expansion of the potential experienced by the particle is modified from Eq. (2.16) to be

$$\Phi(0,z) = V_{\text{ring}} \sum_{j=0}^{\infty} C_{j,\text{asm}}(V_j)(z - Z_{\text{min}})^j. \tag{8.9}$$

$Z_{\text{min}}$ is the potential minimum and $C_{j,\text{asm}}$ are the modified potential coefficients. They are defined by the voltage configuration $(V_i) := (V_1, V_2, V_3, V_4, V_5) = (V_{\text{R1}}, V_{\text{R2}}, V_{\text{R3}}, V_{\text{R4}}, V_{\text{R5}})$ using the potential expressions Eq. (2.16) and Eq. (2.17) as

$$Z_{\text{min}}(V_i) = -\frac{C_1(V_i)}{2C_2(V_i)}, \tag{8.10}$$

$$\begin{aligned} C_{j,\text{asm}}(V_i) &= \frac{2}{j!\Lambda V_0} \sum_{n=1}^{\infty} \left[ \frac{V_1 \cos(k_n z_0) - V_5 \cos(k_n \Lambda)}{k_n} + \sum_{i=1}^{4} \frac{V_{i+1} - V_i}{k_n^2 d} (\sin(k_n z_{2i}) - \sin(k_n z_{2i-1})) \right] \\ &\times \frac{1}{I_0(k_n a)} \left[ \frac{d^j}{dz^j} \sin\left( k_n \left( z + \frac{\Lambda}{2} \right) \right) \right]_{z=Z_{\text{min}}}. \end{aligned} \tag{8.11}$$

In Eq. (8.10), the coefficients $C_1(V_i)$, $C_2(V_i)$ are calculated as functions of the voltage configurations by Eq. (2.17). The effect of the voltage drop at R4 can be expressed by applying the voltage configuration $(V_{\text{R1}}, V_{\text{R2}}, V_{\text{R3}}, V_{\text{R4}}, V_{\text{R5}}) = (0, \text{TR} \cdot V_{\text{ring}}, V_{\text{ring}}, \text{TR} \cdot V_{\text{ring}} - V_{\text{drop}}, 0)$, where $V_{\text{drop}}$ stands for the voltage difference between R2 and R4, given by
$V_{\text{drop}} =$ (Voltage drop due to the connection) $-$ (Offset voltage additionally applied to R4).
The dependency of $C_{2,\text{asm}}$ on $V_{\text{drop}}$ is expressed as a symmetric function of $V_{\text{drop}}$ in respect of $V_{\text{drop}} = 0$. Therefore the shifted axial frequency

$$\nu_z = \frac{1}{2\pi} \sqrt{\frac{2qC_{2,\text{asm}}(0,\ \text{TR} \cdot V_{\text{ring}}, V_{\text{ring}}, \text{TR} \cdot V_{\text{ring}} - V_{\text{drop}}, 0) \cdot V_{\text{ring}}}{m}} \tag{8.12}$$

has a minimum value at $V_{\text{drop}} = 0$. By sweeping the offset voltage at R4, the shift of the axial frequency is measured as a function of the offset voltage. By tuning the offset voltage to the value which gives the minimum frequency shift, the voltage drop is compensated. For the measurement shown in Figure 8.4, the optimized offset value is obtained from the fitting function as 65(1) mV.

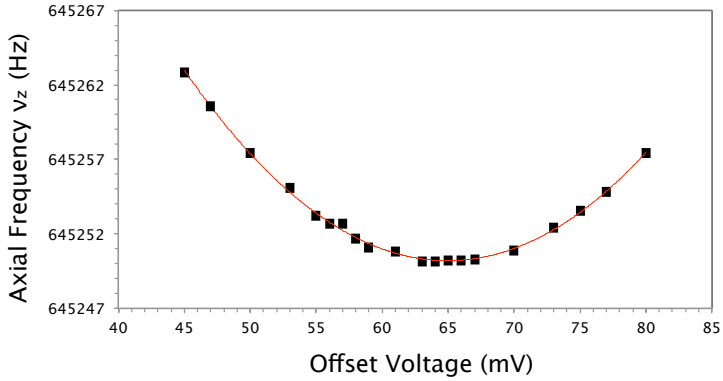


Figure 8.4: Asymmetry compensation performed for the RT using a trapped antiproton. The shift of the axial frequency is plotted as a function of the offset voltage applied to R4. The optimized offset voltage applied to R4 is obtained as 65(1) mV.

# Part IV

# High precision measurements of the cyclotron frequency

# 9. INTRODUCTION TO THE CYCLOTRON FREQUENCY MEASUREMENTS WITH BASE

In the next two chapters of this thesis, we will discuss the methods applied for the high precision measurement of the cyclotron frequency of a single antiproton trapped in a Penning trap of BASE. This chapter introduces the background of the measurement for the sake of discussion in the following chapters. The statistical variables used in the discussion is defined in Appendix A.

## 9.1 Precise Measurement of the Cyclotron Frequency

First, let us discuss about precision we should aim in the cyclotron frequency measurement. The precision of the cyclotron frequency measurement define a sweep interval of the g-factor resonance. The relation between the precision of the cyclotron frequency and the resulted g-factor does not correspond one be one, but it is said that the required precision of the cyclotron frequency is one order lower than the aimed precision of the g-factor. Therefore, in order to realize a measurement of the g-factor of the antiproton with ppb precision, we need precision of 10 ppb for the cyclotron frequency.

The cyclotron frequency of a particle trapped in a Penning trap is obtained by measuring each of the eigenfrequencies $\nu_+$, $\nu_z$ and $\nu_-$. As discussed before, the precision of these measurements are related to precision of the free cyclotron frequency as

$$\Delta\nu_c = \sqrt{\left(\frac{\nu_+}{\nu_c}\Delta\nu_+\right)^2 + \left(\frac{\nu_z}{\nu_c}\Delta\nu_z\right)^2 + \left(\frac{\nu_-}{\nu_c}\Delta\nu_-\right)^2}. \tag{9.1}$$

By substituting $\nu_+/\nu_c \approx 1$, $\nu_z/\nu_c \approx 1/46$, $\nu_-/\nu_c \approx 1/4200$, we see that a contribution of the precision of the magnetron frequency to the precision of the free cyclotron frequency is small, thus a moderate precision suffices for the magnetron frequency. Even if we set the aimed precision of the free cyclotron frequency to a ppb level, the required precision of a magnetron frequency measurement is only at 125 Hz. The high stability of the magnetron frequency against magnetic field fluctuations also merits us to attain a high precision in less frequent measurements. In our measurement, it is typically measured twice a week with an absolute precision of 200 mHz.

To measure the axial frequency and the modified cyclotron frequency, sequences of single-dip and double-dip measurements as shown in Figure 9.1 are employed. The modified cyclotron frequency is calculated by the measured frequencies $\nu_z$, $\nu_l$, $\nu_r$ and the sideband coupling frequency $\nu_{\mathrm{rf}}$. The averaging time for each measurement (indicated as $t_{\mathrm{single}}$ and $t_{\mathrm{double}}$ in the figure) is set between 30 and 120 s.

In next two sections, we shall discuss the precision of the measurements of the axial frequency and the modified cyclotron frequency.

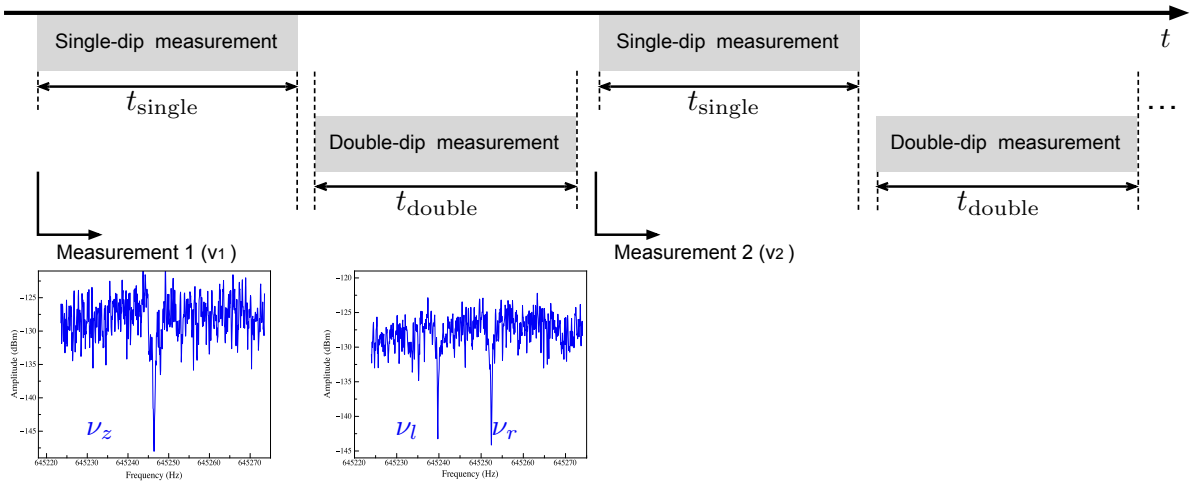


Figure 9.1: Two cycles in a sequence of the cyclotron frequency measurements are shown in the diagram. Single-dip measurements to measure the axial frequency and double-dip measurements by which the modified cyclotron frequency is derived, are performed alternately. A spectrum of a single/double-dip measurement is shown below each part of the diagram. $t_{\mathrm{single}}$ and $t_{\mathrm{double}}$ indicate the averaging time of respective measurements. The time needed for switching is about 1 s.

## 9.2 Stability of the Axial Frequency

The axial frequency of the trapped particle has high stability which is enough for our aimed precision of the cyclotron frequency measurement. According to the measurement, a typical value of the fluctuation for a set of measurements is 40 - 50 mHz. In this section we shall summarize the main factors which cause this fluctuation.

Comparison between fluctuations of axial frequency and the characterization of the voltage sources UM1-14 (see Sect.5.3) made it clear that the stability of the axial frequency mainly depended on the stability of these voltage sources.

According to the measurement performed in [31] before the beamtime, stability of the voltage sources is characterized by the drift of the temperature caused by external factors and an intrinsic electric noise of the voltage sources themselves. The drift of the temperature of the voltage source (which is typically 0.3 K in one night (about 6 h)) causes a drift of their output voltage with the proportionality factor -3.4 $\mu$V/K. The intrinsic noise has an amplitude of 0.2 $\mu$V.

During the beamtime, the temperature of the voltage sources is monitored by a temperature sensor which is implemented in the data logger system. The fluctuation of the temperature $T_{UM}$ is estimated

by an indicator *fluctuation*, whose definition is given in Appendix A. The result is

$$\sigma^f_{\mathrm{T_{UM}}} = 0.24\,\mathrm{K}. \tag{9.2}$$

Assuming that the voltage applied to the ring electrode (see 2.2) of the trap fluctuates by this effect, the axial frequency fluctuation due to this factor is estimated as

$$\frac{\sigma^f_z}{\nu_z} = \frac{1}{2}\frac{\sigma^f_{V_0}}{V_0} = \frac{0.24 \times 3.4 \times 10^{-6}}{2 \times 4.664499} = 8.7 \times 10^{-8}. \tag{9.3}$$

This leads $\sigma^f_z = 56\,\mathrm{mHz}$, which is consistent with the measured fluctuation of the axial frequency.

## 9.3 Possible Reasons of Fluctuations of the Modified Cyclotron Frequency

As discussed in the former section, the modified cyclotron frequency is the most important frequency among the eigenfrequencies we measure. In this section, we discuss the two major possible factors which cause the fluctuations of the modified cyclotron frequency. The following discussion gives a foundation of discussion in the next two chapters.

### 9.3.1 Effects of Magnetic Field Fluctuations on the Modified Cyclotron Frequency Measurement

The modified cyclotron frequency measurement is strongly affected by fluctuations of magnetic field experienced by a trapped antiproton. In Chap 6, we have discussed identified sources of magnetic field fluctuations in the AD hall. To discuss the effects of these magnetic field fluctuations on the cyclotron frequency measurements, we must retain the fact that the fluctuations due to the AD operation are fast and periodic (they fluctuates in a cycle of 80/110 s) , while that from the other sources are slow (their timescales are minutes/hours) and temporal. In fact, the period of the fluctuations due to the AD operation is comparable to or shorter than a typical length of the sequence of the cyclotron frequency measurements. Hereafter in this section, we treat the fluctuations due to the AD operation and the other fluctuations separately, since their effects on the modified cyclotron frequency measurement appear differently.

First, we shall see how the slow magnetic field fluctuations affect the measurement of the modified cyclotron frequency. Figure 9.2 shows the results of typical one shift of the modified cyclotron frequency measurements. Identified activities of ASACUSA and the AD crane are noted on the figure. Here, we can see some obvious effects of the magnetic field fluctuations on the modified cyclotron measurements. Around time $= 4\,\mathrm{h}$, a ramp up of one of the superconducting magnets of ASACUSA increased the magnetic field experienced by the antiproton by about $0.2\,\mu\mathrm{T}$ in about an hour.[1] After the ramp up of the superconducting magnet, continuous adjustment of bending magnets of a beamline

[1]This measurement was performed when ASACUSA was doing experiments with antiprotons from the AD. In another occasion, we observed the same order of magnetic field shifts caused by the magnets of the other experimental groups in the AD.

of antiprotons to the ASACUSA zone caused magnetic field fluctuations with amplitudes of about 1-10 nT.

We also find an effect of a crane operation at time $\approx 8.5$ h. The temporal shift of the magnetic field experienced by the antiproton, which was about $0.1\mu$ T changed the modified cyclotron frequency by 3 Hz.

In a time domain before time $= 4$ h, only some normal-conducting magnets of ASACUSA were being adjusted, which caused less fluctuations. In this domain, we observe a drift of the modified cyclotron frequency corresponded to a magnetic field drift about $0.13\mu$ T/h (67 ppb/h) , which is supposed to be caused by a drift of pressure inside the bore of the BASE magnet.[2] An effect of this slow drift can be compensated by evaluating an average of succeeding cyclotron frequency measurements, therefore it is possible to perform a g-factor measurement in the presence of such a drift. For a detail explanation of the procedure to measure a g-factor resonance and the method to cancel the magnetic field drift, see Appendix B.

Since their effects visibly appear on the results of the measurements, the effects of the slower magnetic field fluctuations can be avoided by appropriate data selection.

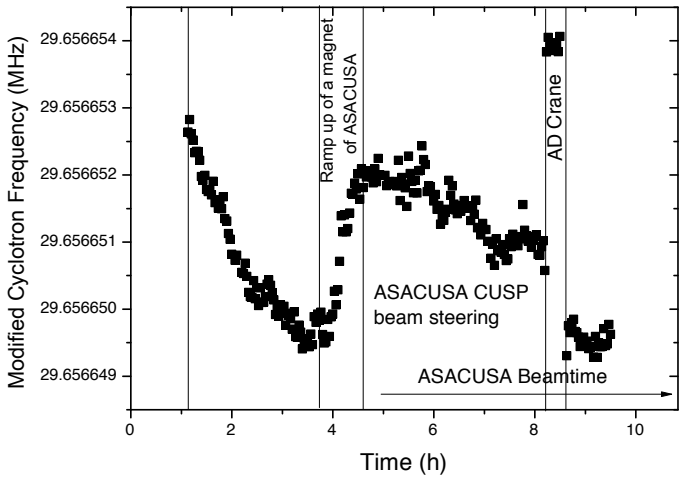


Figure 9.2: A result of continuous measurements of the modified cyclotron frequency. Activities of ASACUSA and the AD crane are noted on the graph.

[2]The exhaust of the superconducting magnet is connect to a recovery line of CERN, through which the evaporated Helium gas is sent to a facility for recycling. The pressure drift of this recovery line is supposed to change the pressure inside the bore of the magnet, and thus change the magnetic filed experienced by the antiproton mainly due to the slight shifts of the position the magnet. The natural drift of the BASE magnet of about 3 nT/h (1.5 ppb/h) is even smaller than the one observed in Figure 9.2.

Now, we shall discuss the effects of the fast magnetic field fluctuations due to the AD operation. We don't see clear effects of the fast fluctuations in the measurements shown in Figure 9.2. One reason for this is they are hidden because of their small amplitudes compared to that of the slow fluctuations. According to the measurement in Chap.6, their amplitudes are smaller than that of the fluctuations from the other sources by one order. Second, and more importantly, their cycle length of 80/110 s are comparable to or shorter than the cycle of the cyclotron frequency measurements, which is typically 100 s including both single and double-dip measurements. Consequently, the effects of the fast fluctuations don't appear as visible shifts of the frequency measured in each measurement. Instead, they cause fluctuations of the frequency obtained in different measurements, which remain even after canceling the effects of the slow fluctuations. Therefore, they can limit the precision of our cyclotron frequency measurements.

In Chap.10, the effects of the fast fluctuations due to the AD operations are discussed in more detail, together with a solution to suppress their effects on the measurements.

### 9.3.2 Frequency Fluctuations due to the Trap Imperfection

As discussed in Sect.2.3, the remaining imperfection of the trap couples with the particle's motion and shifts its eigenfrequencies. Consequently, fluctuations of the energies of the eigenmodes appear as fluctuations of the cyclotron frequency depending on the coupled trap imperfection. In this section, we shall discuss these effects in detail.

Based on the result of the optimization performed in Chap.8, we assume that the anharmonicity of electrical potential are suppressed to a negligible order. As for the coupling to the inhomogeneity of the magnetic field, the leading terms of $\Delta\nu_+$, $\Delta\nu_z$ are given by Eq.(2.30) and Eq.(2.31) as,

$$\Delta\nu_+ \simeq \frac{1}{4\pi^2 m}\frac{\nu_+}{\nu_z^2}\frac{B_2}{B_0}\cdot E_z \tag{9.4}$$

$$\Delta\nu_z \simeq \frac{1}{4\pi^2 m\nu_z}\frac{B_2}{B_0}\cdot E_+ \tag{9.5}$$

Let us discuss how these frequency shifts of the eigenfrequencies affect the cyclotron frequency measurement by the sideband coupling. The shifts of eigenfrequencies

$$\nu_+ \to \nu_+ + \Delta\nu_+(E_z), \quad \nu_z \to \nu_z + \Delta\nu_z(E_+)$$

result in shifts of $\nu_l$, $\nu_r$ measured by the sideband coupling as

$$\nu_l = \nu_z + \Delta\nu_z(E_+) - \frac{\Omega}{4\pi} - \frac{\delta}{2} \tag{9.6}$$

$$\nu_r = \nu_z + \Delta\nu_z(E_+) + \frac{\Omega}{4\pi} - \frac{\delta}{2}. \tag{9.7}$$

By its definition, the detuning $\delta$ is expressed as follows:

$$\delta = \nu_{\mathrm{rf}} - (\nu_+ + \Delta\nu_+(E_z) - \nu_z - \Delta\nu_z(E_+)) \tag{9.8}$$

The above three equations lead to

$$\nu_+ + \Delta\nu_+(E_z) = \nu_{\mathrm{rf}} + \nu_l + \nu_r - \nu_z - \Delta\nu_z(E_+), \tag{9.9}$$

which relates the shift of the modified cyclotron frequency $\Delta\nu_+(E_z)$ with that of the axial frequency $\Delta\nu_z(E_+)$ during the sideband coupling measurement. Note that during the coupling, both modes are at thermal equilibrium by the coupling to an axial detector. The temperature of each mode $T_+$, $T_z$, the averaged energy of each mode $< E_+ >$, $< E_z >$ are related to each other as

$$\frac{< E_+ >}{< E_z >} = \frac{T_+}{T_z} = \frac{\nu_+}{\nu_z}. \tag{9.10}$$

Therefore the averaged frequency shifts $\overline{\Delta\nu_+}$ and $\overline{\Delta\nu_z}$ are expressed using the axial temperature $T_z$ as

$$\overline{\Delta\nu_+} = \overline{\Delta\nu_z} = \frac{1}{4\pi^2 m}\frac{\nu_+}{\nu_z^2}\frac{B_2}{B_0}k_B T_z. \tag{9.11}$$

The energy of each mode $E_+$ and $E_z$ fluctuates according to their Boltzmann distribution respectively defined by $T_+$ and $T_z$. As a result, these energy fluctuations appear as frequency fluctuations of $\nu_+$ and $\nu_z$.

The feedback system introduced in Sect.3.2 allows us to decrease the temperatures $T_+$ and $T_z$. Therefore it is expected to be effective to reduce the frequency fluctuations. We applied the feedback system to the measurement of the axial frequency and the modified cyclotron frequency. The performance of the system and its effect will be discussed in Chap. 11.

# 10. Systematic Uncertainty due to the AD noise

## 10.1 Effects of the AD operation to the Cyclotron Frequency Measurement

In this chapter, we shall discuss the effects of the fast fluctuations of the magnetic field fluctuations due to the AD operation.

The data used for the evaluation were measured by the measurement sequence shown in Figure 10.1. This measurement was performed to demonstrate our technique of swapping two particles. Two antiprotons were parked at the high voltage electrodes and loaded into the trap alternately by adiabatic shuttling.

The averaging time for single-dip and double-dip measurement are 100 s and 60 s, respectively. The total cycle length of a set of measurement of two antiprotons including transport was 332 s. The AD was operated on the low energy mode, which has a cycle length of about 110 s.

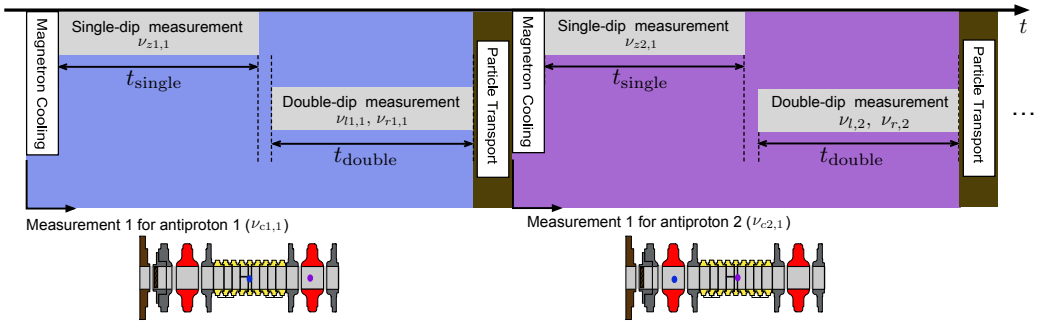


Figure 10.1: A measurement sequence of the cyclotron frequency comparison. Two antiprotons are marked by blue and purple. The two antiprotons are alternately loaded into the trap to measure their cyclotron frequency.

To discuss the short-timescale fluctuations, the ratio of the frequency from the sequential measurement of the two particles are evaluated. The ratio of the measured cyclotron frequencies $(\nu_{c1}/\nu_{c2})_i$ is defined in a way described in Figure 10.2. This evaluation cancels the slow fluctuations and drifts which have longer timescales than the measurement cycle, and enable us to discuss the order of the fast fluctuations which limit the precision of the cyclotron frequency measurement performed as a part of the g-factor measurement.

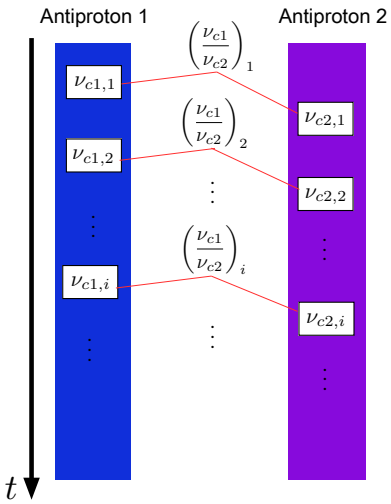


Figure 10.2: The definition of the array of the cyclotron frequency ratio calculated from the sets of cyclotron frequencies of the two antiprotons.

Figure 10.3 shows one set of the cyclotron frequency ratios. We see oscillating behavior of the frequency ratio. The amplitude of the oscillation is in the order of $10^{-8}$ which corresponds to a difference of the magnetic field of about 20 nT. The oscillation has a long period about $5 \times 332 = 1660$ s. A possible explanation of this oscillation is that a difference between the cycle length of the cyclotron frequency measurement and that of the AD operation causes a periodic shift of the magnetic field experienced by the antiprotons at different cycles due to the different phases of the AD operation. As a result, the oscillation is supposed to appear as a beat between the two cycles.

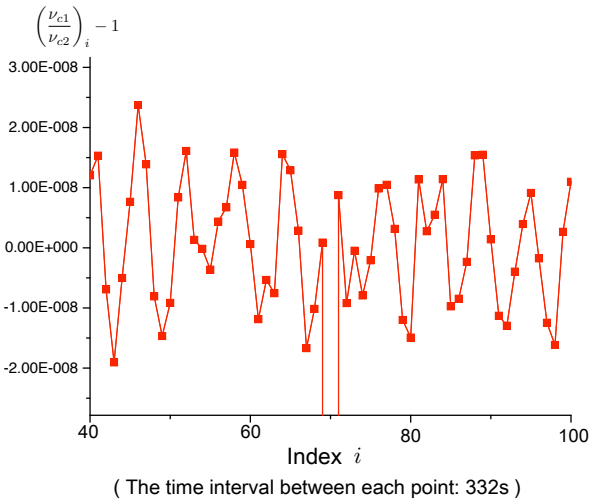


Figure 10.3: The transient of the cyclotron frequency ratio of the two antiprotons. The time interval between each point is about 332 s

## 10.2 Comparison with the Ambient Magnetic Field Fluctuations

If the short-timescale fluctuations observed in Figure 10.3 is the beat between the measurement cycle and the AD operation cycle, it should be compared with the measurement of the ambient magnetic field by the GMR sensor implemented in the data logger system. As presented in Sect.6.2, the GMR sensor is able to detect the magnetic field fluctuations produced by the AD operation. The set of data of the two-particle frequency measurements ($t_{\text{single}} = t_{\text{double}} = 60\,\text{s}$) and the ambient magnetic field measurement by the GMR sensor in an interval of 1 s are prepared for the evaluation. The AD was operated in a cycle of about 110 s during these measurements were performed.

To compare the ambient magnetic field measurement with that of the fluctuations of the frequency ratio, the averaged magnetic field during each frequency measurement is calculated from the data of the ambient magnetic field measurements. Arrays $B_{1,i}$ and $B_{i,2}$ are defined by averaging the ambient magnetic field during the double-dip measurement of each measurement cycle for particle 1 and 2, respectively. Their ratio $B_{1,i}/B_{2,1}$ is also evaluated to compare the difference of the averaged magnetic field between the measurement of the two particles.

In the result shown in Figure 10.4, we can see a drift of the magnetic field with long timescale which is observed in a) is canceled out in b). In Figure 10.4 a), we can see that oscillations in the averaged magnetic fields $B_{1,i}$ and $B_{2,i}$ which represent the difference of the phase of the AD operation when each frequency measurement is performed. In Figure 10.4 b), we also see the oscillation in the ratio $B_{1,i}/B_{2,1}$, which suggests that the difference of the AD phase at the time of the measurement between particle 1 and 2 periodically changes in a super-cycle of the frequency measurement and the AD operation.

The amplitude of the ratio of the magnetic field $B_{1,i}/B_{2,1}$ observed in Figure 10.4 b) is about 0.003, which corresponds to the fluctuations of the averaged magnetic field of $13.63 \times 0.003\,\mu\text{T} =$

40 nT. This will become smaller by one order in the BASE magnet. The resulting 4 nT is consistent with the fluctuations in the cyclotron frequency observed in the former section. This gives an order of differences of the averaged magnetic field experienced by the particles in different measurements.

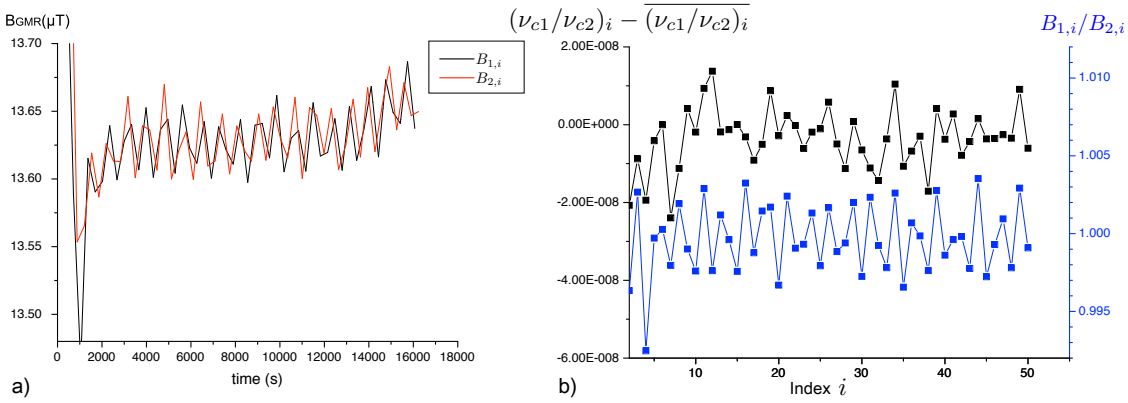


Figure 10.4: a) The averaged magnetic field $B_{1,i}$, $B_{2,i}$ as functions of time. b) The ratio of the measured cyclotron frequencies (black line, left axis) and the ratio of the averaged ambient magnetic field during the measurement (blue line, right axis). The ratio of the averaged magnetic field is calculated from the data shown in a).

## 10.3 The Triggered Measurement Scheme

To overcome the magnetic field fluctuations discussed above, the measurement sequence is synchronized to the AD operation cycle. In this section, we will discuss the effects of this scheme.

Figure 10.5 shows the measurement sequence for the dataset of the triggered measurement treated in this section. Since a two-antiproton measurement using the triggered sequence was not performed, a set of continuous measurements of the cyclotron frequency of a single antiproton is employed for the evaluation. Each measurement is triggered by a signal which is synchronized to the injection of a proton beam to the AD.

The averaging time for the measurement is set shorter; $t_{\mathrm{single}} = t_{\mathrm{double}} = 53\,\mathrm{s}$ so that a measurement cycle fits within one AD cycle of about 110 s. The AD was operated on the low energy mode. As shown in Figure 10.6, the time domain of the double-dip measurement is adjusted to an AD phase where the produced magnetic field is relatively stable. The measurement of the ambient field is referred for this adjustment.

To evaluate the result of this measurement in the same way with that of Sect. 10.1, the variable corresponds to the frequency ratio of two particles is defined by taking the ratio between the sequential measurements as described in Figure 10.7.

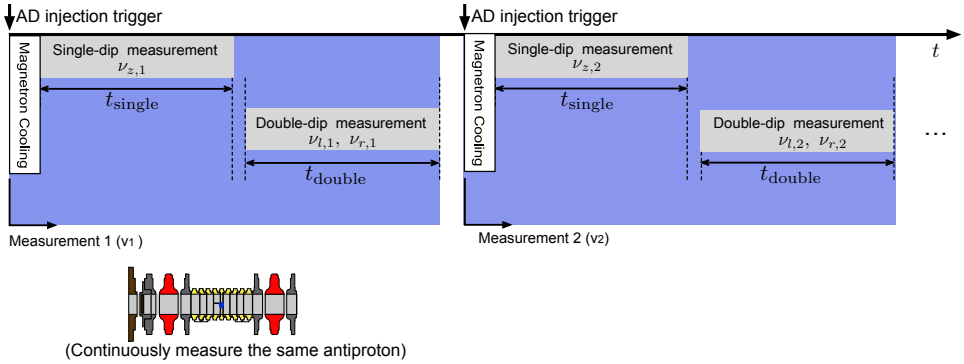


Figure 10.5: The cyclotron frequency of a single trapped antiproton is measured continuously. The measurement sequence is triggered by a signal synchronized to the injection of proton to the AD. The time window of the double-dip measurement is adjusted to an AD phase where the produced magnetic field is relatively stable.

The frequency ratio $(\nu_{c1}/\nu_{c2})_i$ is compared between the triggered and the untriggered measurement sequence in Figure 10.8 and 10.9. In Figure 10.8, we can see the oscillation appears in the transient of the frequency ratio a) in the untriggered sequence decreases its amplitude by half in the triggered measurement sequence in b). In Figure 10.9, the widths of the distributions of the frequency ratio estimated by rms values of the distributions, makes it clear that the triggered measurement scheme reduced the fluctuations by half.

By this triggered measurement scheme, the relative fluctuations are finally suppressed to 9.6 ppb for this dataset. The remaining fluctuations are caused by differences of the magnetic field produced by each AD cycle. This precision is enough precision to perform a planned g-factor measurement with ppb precision.

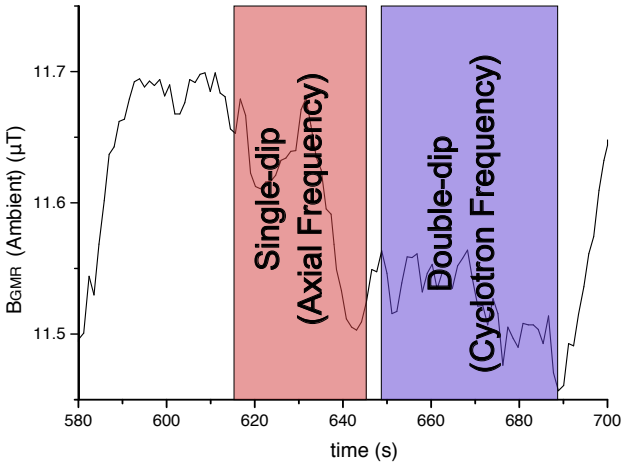


Figure 10.6: The time windows where the single-dip and the double-dip measurement are performed are shown. The measured ambient magnetic field is plotted together.

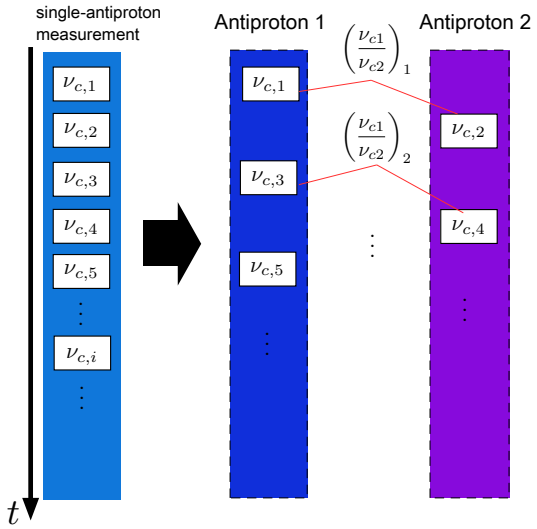


Figure 10.7: The variable $(\nu_{c1}/\nu_{c2})_i$ is defined for a continuous measurement of a single antiproton by taking the ratio of the sequential measurements as defined above.

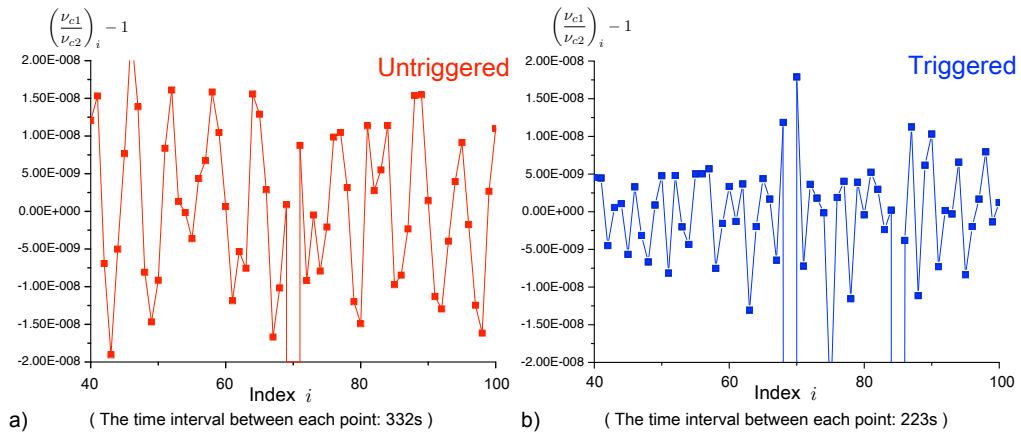


Figure 10.8: a) The transient of the frequency ratio $(\nu_{c1}/\nu_{c2})_i$ in case of the untriggered measurement. The same data as Figure 10.3 is shown again for a reference. b) The transient of the frequency ratio evaluated for a dataset obtained by the triggered measurement scheme.

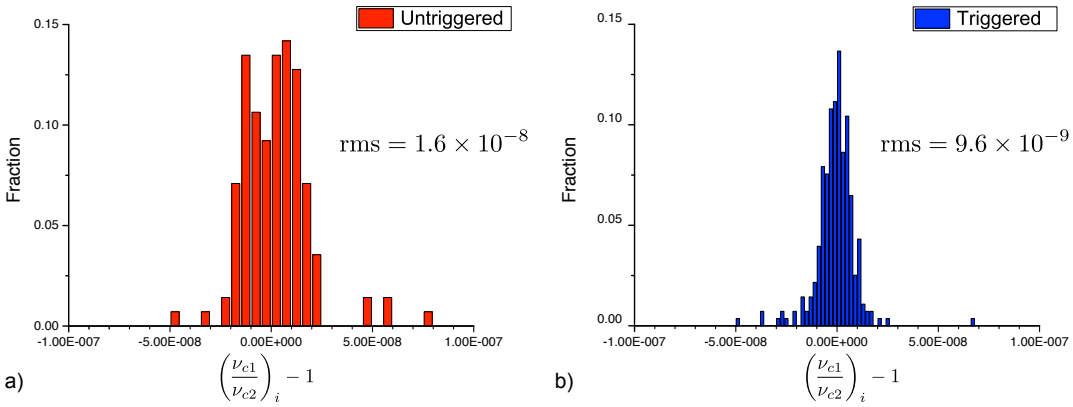


Figure 10.9: Histograms of the distributions of the cyclotron frequency ratio for triggered and untriggered measurement.

# 11. Application of the Feedback System

Within this thesis, an active feedback system to cool the axial motion of the trapped particle has been developed and implemented into the BASE experiment. This chapter present its performance and discusses its effects on cyclotron frequency measurements of a single antiproton.

## 11.1 Construction and Characterization of the Feedback circuit

Figure 11.1 shows a schematic of the feedback circuit implemented in the axial detection system. Note that the phase of the feedback signal is opposite from the model discussed in Sect.3.2. The detector signal is mixed down to become within the input range of the FFT analyzer. This signal is split, mixed up and fed back to the detector. The phase of the feedback signal is tuned by the phase of the local oscillator L.O. 2 in the figure. The two local oscillators are phase locked to a 10 MHz Rb frequency standard.

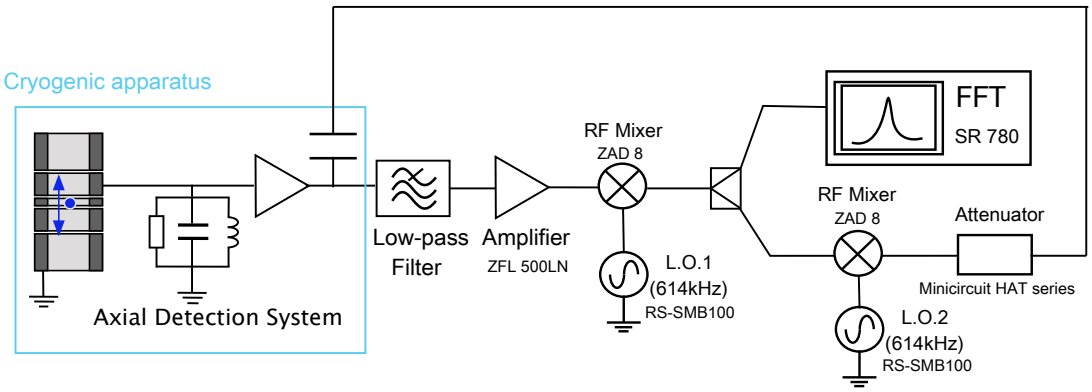


Figure 11.1: A schematic of the feedback circuit. The low pass filter before the amplifier is needed to prevent signals outside the range around the resonator frequency from being fed back to the detector. The attenuator consists of fixed attenuators connected in series. The attenuation is tuned by replacing parts of the attenuator.

Figure 11.2 shows the detector signal with different feedback strength of positive and negative feedback. The relative temperature of the detector for each condition is estimated from the dip width of the signal using the relation Eq.(3.21) and (3.24). The ratio of the temperature of the resonator with and without feedback $T_e/T_0$ was swept in a range between 0.5 and 12.

The absolute temperature of the axial detector was estimated by the power of noise generated by an

amplifier at the 4 K stage to be $T_0 = 6.2(1.5)$ K. Accordingly the axial temperature of the antiproton is cooled down to

$$T_{z,\mathrm{FB}} = 3.1(8)\,\mathrm{K}$$

by the application of negative feedback. [1]

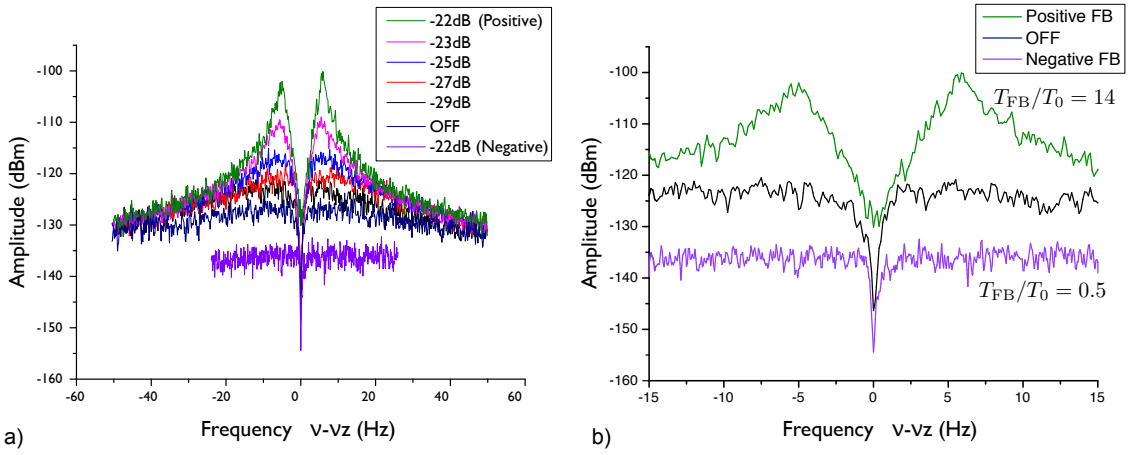


Figure 11.2: Spectra of the detector signals of a single antiproton, measured at different feedback conditions. The noted values of attenuation are the attenuation of the attenuator in Figure 11.1. To apply negative feedback, the phase of the L.O.2 of Figure 11.1 is set to be negative. b) shows a zoomed-in view of three signals shown in a).

[1] The uncertainty of the dip widths were estimated from by widths of their distribution. Datasets used for the estimation is one night measurement with and without feedback, which will be used in discussion in the next section. They were used to estimate the uncertainty of the absolute temperature with and without feedback. The uncertainty of the ratio was derived from these two values.

## 11.2 Cyclotron Frequency Measurement with Negative Feedback.

### 11.2.1 Measurement sequence and the preparation of datasets.

As discussed in Sect.9.3.2, the cooling of the axial resonator is expected to suppress the possible frequency fluctuations due to the trap imperfection, and thus improve the stability of the cyclotron frequency measurement. To test this method, the cyclotron frequency of the antiproton was measured for one night with negative feedback. The result of the measurement was compared to another night measurement without feedback cooling. For this measurement, the triggered measurement sequence in Figure 10.5 for a single antiproton was employed. The averaging time was set to be $t_{\text{single}} = t_{\text{double}} = 53\,\text{s}$. The trapped antiproton was cooled down to 3.1 K during the measurement with negative feedback.

To get the information for data selections, datasets of the ambient magnetic field measured by the Hall probe included in the data logger system were referred. The ambient magnetic field was continuously recorded in an interval of 1 s by the Hall probe. From these data of the ambient magnetic field, an array of the averaged ambient magnetic field $B_{\text{Hall},i}$ are defined by averaging the field over the time domain where the double-dip measurement is performed in each measurement cycle. From the measured frequencies, the averaged magnetic field and their jitters, the set of arrays $(\nu_{+,i},\ \nu_{z,i},\ B_{\text{Hall},i}, \delta\nu_{+,i},\ \delta\nu_{z,i},\ , \delta B_{\text{Hall},i})$ is defined. For the defined set of raw data, data which satisfy the following condition are chosen for evaluation.

1. $|\delta B_{\text{Hall},i}| < 0.1\mu T$
2. $|\delta\nu_{z,i}| < 100\,\text{mHz}$
3. $|\delta\nu_{+,i}| < 1\,\text{Hz}$.

The value of the cut used for the magnetic field jitter was defined by $2\sigma$ of its background distribution, which are mainly from the AD fluctuations. For the cut for the frequency jitters, the values were set to exclude the outliers of their gaussian-like distribution.

For data after the cut by the above condition, a scatter of $(\nu_{z,i}, \nu_{+,i})$ are plotted. The plotted $(\nu_{z,i}, \nu_{+,i})$ distributes in several groups separated from each other. This distribution implies that the frequency shifted several times for a larger degree due to some kind of external effects. In order to estimate the fluctuations due to the trap imperfection, we must treat these groups separately. By grouping each cluster on the scatter plot as a set of data, several datasets are defined for both conditions.

For each group of the data, the correlation coefficient between the two frequencies $r(\nu_{z,i}, \nu_{+,i})$ are calculated to chose the data which satisfy

$$|r(\nu_{z,i}, \nu_{+,i})| > 0.3. \tag{11.1}$$

For the frequency fluctuations caused by the coupling of the trap imperfection and fluctuations of the particle's energy, the fluctuations of the cyclotron frequency and that of the axial frequency should be correlated to each other according to the discussion of Sect.9.3.2. The above selection was performed to select the fluctuations which have such a statistical trait.

### 11.2.2 Results of the comparison

In the end, one set of the data with feedback cooling (with 135 samples) and another set of data without feedback cooling (with 104 samples) were obtained.

Histograms of the frequency jitters are plotted in Figure 11.3 for the comparison. Table 11.1 compares the fluctuations $\sigma_z^f$ and $\sigma_+^f$, defined as distributions of the jitters, are derived by the fitting of the distribution of the jitters of the eigenfrequencies.

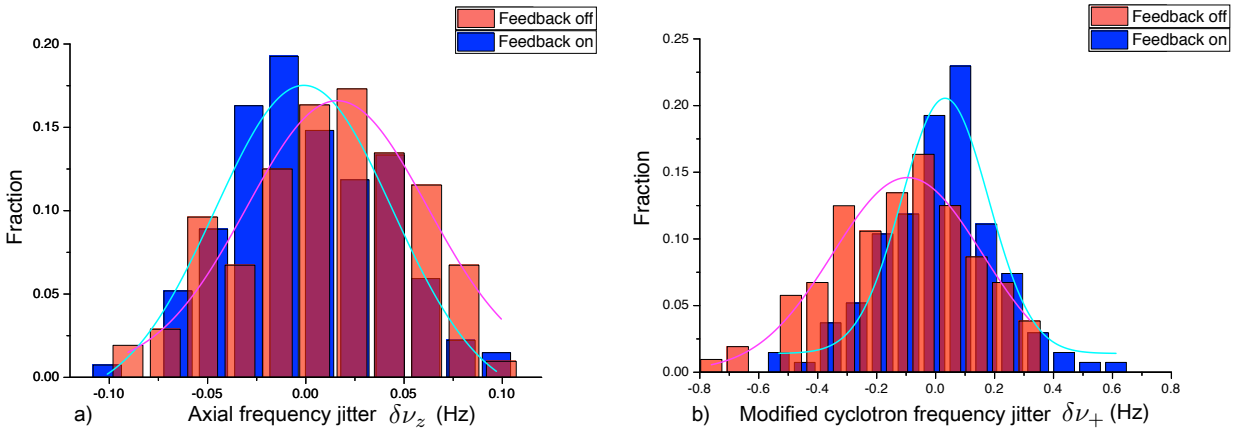


Figure 11.3: The jitters of the axial and modified cyclotron frequencies. The data with feedback and without feedback are compared.

| | Feedback ON (Hz) | Feedback OFF (Hz) |
|---|---|---|
| $\sigma_z^f$ | 0.038 | 0.044 |
| $\sigma_+^f$ | 0.20 | 0.23 |

Table 11.1: The summary of the results of comparison of the frequency fluctuations between the dataset with feedback and without feedback.

For both frequencies, 14 % of suppression in fluctuations were observed. However, this is not significant enough to statistically conclude that the fluctuations are decreased by the application of feedback cooling.

This suggests that the anharmonicity of the trap is well compensated by the optimizations performed in Chap.8 and the inhomogeneity of the magnetic field is not as large as it causes the significant frequency fluctuations. By using the difference between the fluctuation of the axial frequency with and without feedback, we can estimate an upper limit of $B_2$ from this measurement.

Assuming a property of the Boltzmann distribution, $\sqrt{< E_z^2 >} = \sqrt{2} k_B T_z$, the fluctuation of the

axial frequency expressed as Eq.(9.11) has a fluctuation $\sigma_{z.\text{theory}}$ denoted as

$$\sigma^{f}_{z.\text{theory}} = \sqrt{2} \cdot \frac{1}{4\pi^2 m} \frac{B_2}{B_0} \frac{\nu_+}{\nu_z^2} \cdot \sqrt{2}\, k_B T_z \tag{11.2}$$

We have no information to determine how much is the contribution of the energy fluctuations out of the measured fluctuations of the axial frequency. However, assuming that all of the measured fluctuations are from the energy fluctuations, we can obtain an upper limit of $B_2$ as

$$\begin{aligned} \sigma_{z,\text{FB OFF}} - \sigma_{z,\text{FB ON}} &= 2 \cdot \frac{1}{4\pi^2 m} \frac{B_2}{B_0} \frac{\nu_+}{\nu_z^2} \cdot\ k_B(6.2 - 3.1) < 0.044 - 0.038 \\ &\Rightarrow \frac{B_2}{B_0} < 0.065 \\ &\Rightarrow B_2 < 0.13\,\text{T/m}^2. \end{aligned} \tag{11.3}$$

In conclusion, the application of feedback cooling didn't significantly improve the precision of the measurement. However, the observed performance of the feedback system is still expected to merit the experiment in other ways.

The most expected future application of the feedback cooling is to improve the precision of the measurement of the g-factor resonance. The main factor which causes the broadening of the g-factor resonance is the axial amplitude of the particle. The axial amplitude of the particle couples with the magnetic field inhomogeneity, and difference of the Larmor frequency according to its position causes the broadening of the resonance. Accordingly, cooling of the axial temperature makes the line-width of the measured g-factor resonance narrower, and expectedly improve the precision of the finally obtained g-factor. The ability of the feedback system, to cool the antiproton down to 3.1 K will be a strong tool to achieve the g-factor measurement with the aimed precision.

# 12. Conclusion and Outlook

## 12.1 Conclusion

In this thesis, the methods toward the high precision measurement of the cyclotron frequency of the antiproton have been discussed as a part of the BASE experiment, which is one of the two important ingredients to perform high precision magnetic moment measurements.

In the first part of the thesis, the methods to prepare a single antiproton were developed. Antiprotons provided by the AD are caught by using a degrader and adequately timed high voltage pulses, then cooled by radiatively cooled electrons. Procedures to prepare a clean cloud of antiprotons in the center of the Reservoir trap were developed.

After applying the cleaning procedure and separation method to the antiproton clouds, a single antiproton is prepared in the Reservoir Trap. The Reservoir Trap is a new development and one of the key components of the BASE setup. Methods were developed to extract a single antiproton from the reservoir without losing other antiprotons.

This single antiproton was used to optimize the trap. The schemes were applied to tune the trap to ultra-high harmonicity and to compensate the asymmetry. They are the key techniques to provide fast and accurate measurements of the cyclotron frequency by using sideband coupling.

In the further part of the thesis, the cyclotron frequency measurements for the single antiproton are performed. Based on these measurements, magnetic field noise in the AD hall were characterized, and correlations between the magnetic field shifts due to external activities in the AD hall and the measured cyclotron frequencies were found. This provides important triggers for data evaluation.

We also found that fluctuations due to the AD operation which have about the same timescale with the measurement sequence of the cyclotron frequency contribute to fluctuations of the magnetic field experienced by the particle at the level of 10 ppb. They were reduced by triggering the measurement sequence by the AD injection trigger. By this strategy, we reduced the effects of the AD noise to the cyclotron frequency in a defined measurement time by half. The relative fluctuation is finally suppressed below 10 ppb, which is enough precision to preform a g-factor measurement with precision of ppb.

Furthermore, within this thesis, a system to apply active feedback cooling of the axial motion of a single trapped antiproton was developed. We cooled the axial temperature of an antiproton down to 3.1 K (0.27 meV). The feedback system was applied to the cyclotron frequency measurement. The cyclotron frequency measurement was performed to the cooled antiproton. The result of the measurement didn't significantly improve the precision of the measurement, which suggests that most of the frequency fluctuations are not due to the trap imperfections. However, the feedback method has high potential pf application to improve high precision measurements of the magnetic moment, e.g. by

reducing line-width of g-factor resonances measured in the Analysis Trap.

## 12.2 Outlook

Within this thesis, it has been shown that magnetic field fluctuations in the AD hall significantly contributes the frequency fluctuations, therefore limits the precision of the planned g-factor measurement. The strategies to reduce these magnetic field fluctuations are discussed below.

### 12.2.1 Improvement of the Shielding

As a major upgrade of the apparatus in 2015, the superconducting magnet is planned to be exchanged to an order made magnet which has a 20 times higher shielding factor than the current magnet.

Another thing planned for an improvement of the shielding is implementation of a self-shielding coil. The principle of the self-shielding coil is described in [32]. It is a shorted superconducting wire which compensates the magnetic field fluctuations by the induced current according to the Lenz law. By choosing an appropriate dimension of the coil, one can perfectly cancel out the field fluctuation at the center of the coil for an assumed homogeneous fluctuation. The shielding factor $S$ is defined by

$$S(0,0) = \frac{B_{\text{ext}}(0,0)}{B_{\text{ext}}(0,0) + B_{\text{coil}}(0,0)} \tag{12.1}$$

where $B_{\text{ext}}(\rho, z)$ and $B_{\text{coil}}(\rho, z)$ stand for an external magnetic field and the magnetic field produced by an induced current of the coil, respectively. $S^{-1} = 0$ corresponds to perfect shielding.

As a by-product of this thesis, a self-shielding coil was designed by simulations on *COMSOL Multiphysics*. For a fixed radius of the coil, simulations were performed for different lengths of the coil $l_c$ to decide the turn of the coil. The dimension assumed for the simulations and the results of the simulations are shown in Figure 12.1. The inverses shielding factor $S^{-1}$ crosses the axis at $l_c/r_c = 1.73$, which gives the turn of the coil to be wound around the trap chamber. This result was consistent with the former application of this method to another experiment [33].

This self sheilding coil will be installed on the apparatus by the next beamtime. This will suppress the magnetic field fluctuations by a factor of 2.

### 12.2.2 Optimization of the Triggered Measurement Sequence

Another way to reduce the magnetic field fluctuations is to investigate the triggered measurement sequence further. In the beamtime 2014, magnetic field fluctuations were reduced, but further improvements are proposed by the detailed tuning of the timing and the averaging time of the measurement.

By the measurement of the GMR sensor, it is indicated that the shot-to-shot fluctuations of the magnetic field produced by the AD depends on which time window is chosen for the double-dip measurement in the measurement sequence. For example, if we compare the averaged magnetic field produced by the AD in time window 1 and 2 shown in Figure 12.2, the field produced by the AD is more stable in case of Time window 2. We can estimate the stability of averaged magnetic field for different condition of the timing of the measurement only from the measurement by the GMR sensor.

Figure 12.3 shows a set of such comparison. From the ambient magnetic field data by the GMR sensor, the magnetic field experienced by the particle is calculated for assumed time window of the

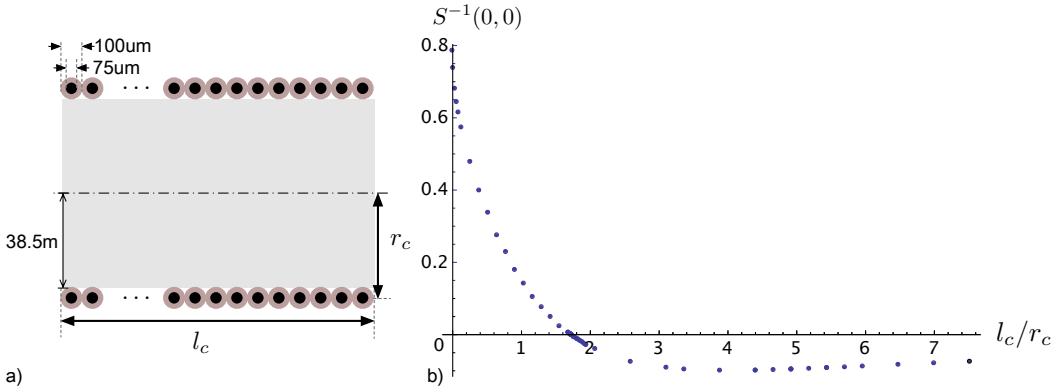


Figure 12.1: a) A geometry assumed for the simulation. b) The result of the simulation. The inverse shielding factor $S^{-1}$ is simulated for different length of the coil, and plotted as a function of the ratio of the length and the radius of the coil $l_c/r_c$.

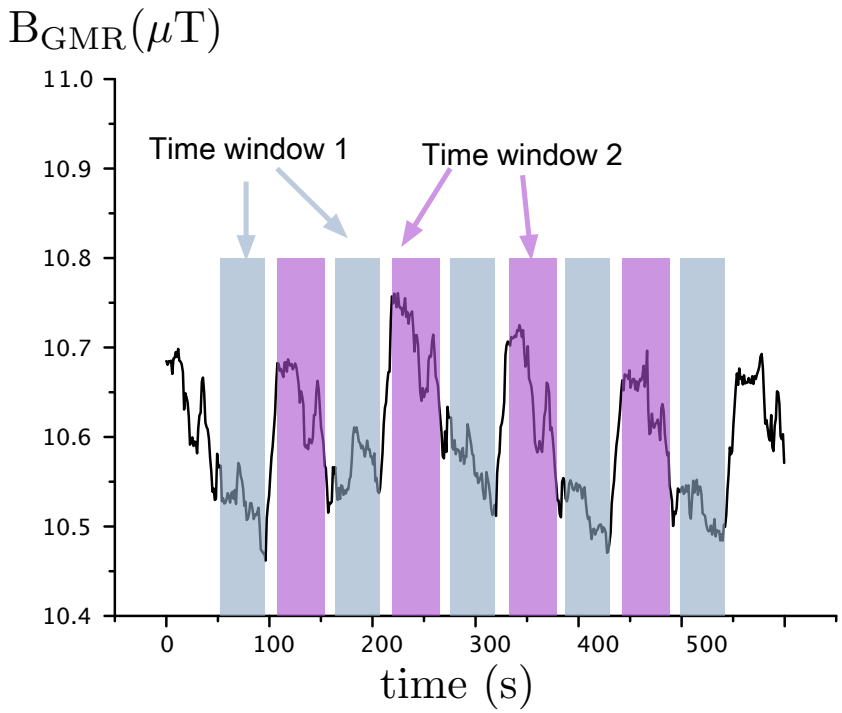


Figure 12.2: The concept of the dependency of the magnetic field fluctuations on the time window for double-dip measurements.

length of 60 s for double-dip measurements, and their distributions are plotted in the histograms. The AD was operated on the high energy mode with a cycle of about 80 s.

The width of the distribution of the ratio of magnetic averaged magnetic field is smaller in time window 1 than in time window 2 by a factor of 1.4. By comparing the relative fluctuations of the magnetic field in this way for various conditions of the measurements such as; the starting time of the measurement, the averaging time of the double-dip measurement, the order between single-dip and double-dip measurements. The magnetic field fluctuations are expected to be reduced by another factor from several to 10.

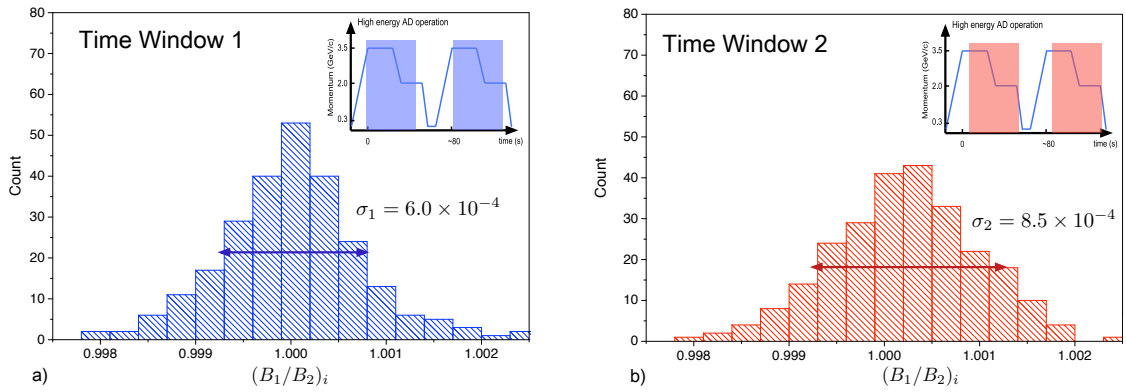


Figure 12.3: The comparison of relative fluctuations of ambient magnetic field for different time windows of the measurement.

By all these upgrades and optimization, we aim to suppress the magnetic field fluctuations experienced by a trapped antiproton from the current state by a factor of 40 - 50 in the next beamtime.

# A. DEFINITIONS OF STATISTICAL VARIABLES

This appendix gives definitions of statistical variables used in discussion in part IV of this thesis.

We shall define statistical variables to estimate orders of fluctuations for sequences of cyclotron frequency measurements, which are arrays of data $\{\nu_{z,i}\}$, $\{\nu_{+,i}\}$. Suppose $\{x_i\}$ as one of such sets. The difference between the succeeding data $\delta x_i$ is defined as the *jitter* of the variable $x$;

$$\delta x_i := x_i - x_{i-1}. \tag{A.1}$$

For the set of $\{\delta x_i\}$, the *fluctuation* of $\{x_i\}$ is defined as the standard deviation of $\{\delta x_i\}$. If one compares the variance of the jitter from the original data,

$$\overline{\delta x_i} = \overline{x_i - x_{i-1}} = \overline{x_i} - \overline{x_{i-1}} = 0 \tag{A.2}$$

$$\begin{aligned}\overline{\delta x_i^2} &= \overline{(x_i - x_{i-1})^2} \\ &= \overline{x_i^2} - 2\,\overline{x_i \cdot x_{i-1}} + \overline{x_{i-1}^2}\end{aligned} \tag{A.3}$$

If we assume that $x_i$ and $x_{i-1}$ are independent, it leads $\overline{x_i \cdot x_{i-1}} = \overline{x_i}^2$. Therefore,

$$\begin{aligned}\overline{\delta x_i^2} =& 2(\overline{x_i^2} - \overline{x_i}^2) \\ \therefore\ \sigma_{\delta x} =& \sqrt{2}\sigma_x.\end{aligned} \tag{A.4}$$

The fluctuation of variable $x$ is denoted as

$$\sigma_x^f := \sigma_{\delta x}. \tag{A.5}$$

In case of our frequency measurement, we often observe frequency shifts of several Hz caused by external effects which can be excluded by data selection. (It is especially the case of the modified cyclotron frequency measurement. See Sect. 9.3.1) The merit of employing the fluctuation as an indicator of the stability is that we can evaluate the stability of the measurement without these effects which can be excluded from the final precision of the measurement.

# B. The Measurement Procedure of the g-factor Resonance

In this appendix, the detailed procedure to measure the g-factor resonance is described.

The g-factor resonance is obtained by repeatedly measuring the spin-flip probability for different frequencies of the spin-flip drive. More precisely speaking, the value $2(\nu_{\mathrm{SF}}/\nu_c)$ is swept instead of the frequency itself. By taking the ratio with the cyclotron frequency $\nu_c$, effects of differences in the magnetic field between different measurements is cancelled.

The detailed procedure of a measurement of the spin-flip probability for one value of $2(\nu_{\mathrm{SF}}/\nu_c)$ is described in Figure B.1. In order to cancel an effect of the magnetic field drift, the cyclotron frequency is measured before and after the irradiation of the spin-flip drive, and the cyclotron frequency at the time of the spin-flip drive is estimated as an interpolated frequency calculated from $\nu_{c,\mathrm{before},i}$ and $\nu_{c,\mathrm{after},i}$. The set of twice cyclotron frequency measurements and the spin-flip drive is repeated for 100 times to derive the spin-flip probability for this value of $2(\nu_{\mathrm{SF}}/\nu_c)$. Throughout the repetition, the ratio of the spin-flip drive and the interpolated cyclotron frequency is kept as constant as possible. The final value of $2(\nu_{\mathrm{SF}}/\nu_c)$ plotted in the resonance plot is determined by applying a maximum likelihood method to the set of $\frac{2\nu_{\mathrm{SF}}}{(\nu_{c,\mathrm{before},i}+\nu_{c,\mathrm{after},i})/2}$.

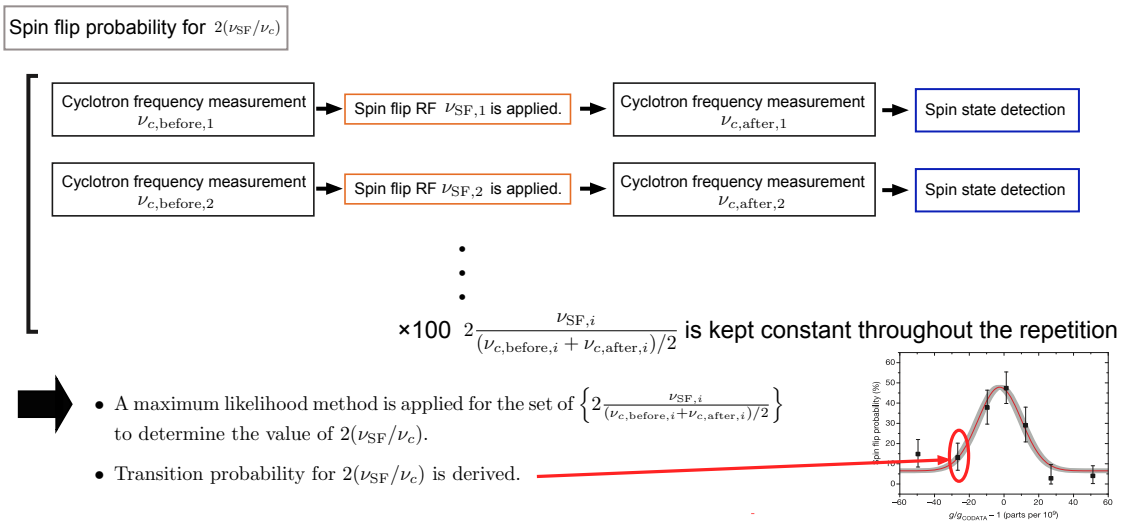


Figure B.1: The description of the procedure to measure the spin-flip probability for one value of $2(\nu_{\mathrm{SF}}/\nu_c)$. The spectrum in the figure is taken from [14]

For the result of the cyclotron frequency measurement of the single antiproton in the beamtime 2014, we derived a set of interpolated frequency from sequential measurements. The fluctuation of the interpolated cyclotron frequency $\overline{\nu_c}$ was estimated as

$$\sigma^{f}_{\overline{\nu_c}} = 6\,\text{ppb}, \tag{B.1}$$

which is enough precision to perform the planned g-favor measurement with ppb precision.

# BIBLIOGRAPHY


[1] R. Bluhm, V. A. Kostellecky, and N. Russell, Phys. Rev. D **57**, 3932 (1998).

[2] F. Ambrosino *et al.*, [KLOE Collaboration], JHEP **12**, 011 (2006).

[3] S. R. Van Dyck, B.P. Schwinberg, and G. H. Dehmelt, Phys. Rev. Lett. 59, 26 (1987).

[4] J. Beringer, R*et al.*, Phys. Rev. D **86**, 010001 (2012).

[5] J. DiSciacca *et al.*, Phys. Rev. Lett. **110**, 130801 (2013).

[6] B. Austin *et al.*, Technical Report, CERN document CERN-PS-95-36 AR. (1995).

[7] S. Ulmer *et al.*, Letter of Intent, CERN document CERN-SPSC-2012-019 / SPSC-I-241 14/06/2012 (2012).

[8] S. Ulmer *et al.*, Technical Design Report, CERN document CERN-SPSC-2013-002 / SPSC-TDR-002 (2013).

[9] H. Dehmelt and P. Ekström, Bull. Am. Phys. Soc. **18**, 72 (1973).

[10] S. Ulmer *et al.*, Phys. Rev. Lett. **106**, 253001 (2011).

[11] C. C. Rodegheri *et al.*, New J. Phys. 14, 063011 (2012).

[12] A. Mooser *et al.*, Phys. Rev. Lett. **110**, 140405 (2013).

[13] A. Mooser *et al.*, Phys. Lett. B **723**, 78 (2013).

[14] A. Mooser *et al.*, Nature **509**, 596 (2014).

[15] J. DiSciacca and G. Gabrielse, Phys. Rev. Lett. **108**, 153001 (2012).

[16] P. Mohr, B. Taylor, and D. Newell, Rev. Mod. Phys. **84**, 1527 (2012).

[17] L. S. Brown and G. Gabrielse, Rev. Mod. Phys. **58**, 233 (1986).

[18] J.D. Jackson, *Classical Electrodynamics* third Ed., Wiley and Sons Inc., New York (1998).

[19] S. Ulmer, PhD thesis, Ruprecht-Karls Universität, Heidelberg (2011).

[20] G. Schneider, Master's thesis, Johannes-Gutenberg Universität, Mainz (1999).

[21] J. Thompson, PhD thesis, Massachussetts Institute of Technology, Cambridge (2003).

[22] D. J. Wineland and H. G. Dehmelt, J. Appl. Phys. **46**, 919 (1975).

[23] J. Johnson, Phys. Rev. **32**, 97 (1928).

[24] B. D'Urso, B. Odom, and G. Gabrielse, Phys. Rev. Lett **90**, 43001 (2003).

[25] E. A. Cornell *et al.*, Phys. Rev. A, **41**, 312 (1990).

[26] D. Mohl *et al.*, Phys. Rep. **58**, 76 (1985).

[27] G. I. Budker *et al.*, Part. Acc. **7**, 197 (1976)

[28] G. Gabrielse, L. Haarsma, and S. L. Rolston, Int. J. Mass Spec. **88**, 319 (1989).

[29] S. Ulmer *et al.*, Annual Report, CERN document, CERN-SPSC-SR-152. (2015)

[30] H. Poth, Phys. Rep. **196**, 135 (1990)

[31] H. Nagahama, Master's thesis, The University of Tokyo (2014)

[32] G. Gabrielse and J. Tan, J. Appl. Phys. **63**, 5143 (1988).

[33] A. Wagner, PhD thesis, Ruprecht-Karls Universität, Heidelberg (2013).

# ACKNOWLEDGEMENTS

この論文が完成するまでの間、たくさんの方々のお世話になりました。ここに感謝して記させていただきます。

松田恭幸准教授には、修士課程を通して様々なかたちでお世話になりました。修士１年の間は駒場でご指導をいただきました。修士２年からCERNに滞在することが多くなったからは直接お話しする機会は少なくなりましたが、私が問題を抱えている時に、いつも時にかなったご助言をしてくださいました。ありがとうございました。また先生がこのBASEコラボレーションに参加する機会を与えて下さったことに感謝しています。

山崎泰規特任教授には、CERN滞在中に多くの面でお世話になりました。折に触れて励ましをいただいたこと、またご多忙な中で私の個人的な事柄にも相談に乗ってくださったことを感謝しています。

鳥居寛之助教には、研究上の疑問や質問について多くご助言を頂きました。また、CERN滞在中の生活やビザの申請など、生活上のことでも多くのアドバイスを頂きました。黒田直史助教には、修士１年次の夏のCERN滞在をはじめ多くの機会でお世話になりました。修士論文の執筆中には、特にAD他CERNの加速器施設のことに関しては貴重なご助言を多くいただきました。提出直前には、ご多忙な中で時間を割いて、丁寧に添削をして頂いたことを、本当に感謝しています。

松田研究室の田中香津生さんには、修士１年次にはミュオン実験でのご指導を中心に、お世話になりました。また、どんなことでも気さくに話して下さり、先輩とお話しできるのをいつも楽しみにしていました。大塚未来さんには、研究室の入ったばかりで右も左もわからない時に親切に助けていただきました。水谷丈洋さんは、折にふれて相談にのっていただき、時に長い時間を割いて一緒に問題を考えて下さいました。田島美典さんには駒場でも、CERNでも、多くの機会に助けていただきました。特に、第 6.2 節の磁場の測定を行う際には、ASACUSAの実験の情報をその都度教えていただいたおかげで、磁場の変動と外部磁場の情報を調べる上で大きな助けになりました。上野恭裕くん、東芳隆くんとは多くの時間を共にすることは出来ませんでいたが、駒場に帰ってくる度に成長している姿を見せてもらい、とても励まされました。そして、石川彰一郎くんには、大学院生活の色んな場面を共に過ごしました。いつでも気軽に話し合える友人がいるのは、CERNに滞在している間も、修士論文をまとめる期間も、最も大きな助けの一つでした。

和田ひとみさんをはじめ、理化学研究所山崎原子物理研究室の皆様には、CERNでの滞在の際に、大変お世話になりました。私が至らないためにご迷惑も多くおかけしましたが、いつも私の事情を理解して下さり、力を尽くして下さったことを心から感謝申し上げます。

I would like to show my gratitude from heart to each of BASE members;
S*tefan Ulmer, Christian Smorra*, *Andreas Hannes Mooser, Kurt Alan Franke*, *Hiroki Nagaham*a, *Georg Schneider* and *Simon Von Gorp*.

*Stefan,* Thank you for supervising me all through my time at BASE. I appreciate you for your trust in me and understanding to my personality. You always suggest the best plan for me. I am so thankful for all your help until I complete this thesis. It was definitely impossible for me to finish this without your help. I am so thankful not only for your sacrificial help, but also for your strong support in encouraging and strengthening me. I was often encouraged and motivated through your trustworthy words.

*Christian*, Thank you for all your help in my work and my life around CERN. I admire you for your knowledge and skills, but more so for your character and kindness. I appreciate for all your sacrificial helps.

*Andi*, You have always answered my questions and give me many profitable advices. Thank you for all your helps for me. I have learned many things about the Penning trap. Thank you for your encouragement and the help in my thesis work.

*Kurt,* Thank you for always willingly answer my questions. I learned from you a lot about data communications and the LabVIEW. I am also grateful for your kind friendship.

*Hiro*, Thank you for your helps and your friendships and many many practical helps. You have been the best advisor thorough my time at CERN.

*Georg*, Thank you for taking care of me when at the beginning point I joined BASE, I didn't spent long time with you, but your care at that time was a great help for me to get used to my new projects. And your thesis had been one of the best references for me to understand about BASE.

*Simon*, You have always encouraged me when you speak to me. Thank you also for helping in my lab work and the calculation works.

I would like to show my gratitude to *Matthias Borchert* and *Andrei Horia Gheorghe* for their help for our group and inspired me through their works.

また、生活上で、精神的に私を支えて下さった皆様ひとりひとりに感謝を表したいと思います。

浜寺聖書教会の皆さんに、いつも変わらないお祈りと励ましをありがとうございます。頻繁にお会いすることは出来なくても、祈り、祈られている関係が自分にとってかけがえのない支えです。また、大阪に帰る度、皆さんの主への忠実さにいつも励まされ、原点に帰ってきたように感じます。

グレース宣教会東京チャペルの皆さんには、東京での生活の間、とてもお世話になりました。ありがとうございます。祈祷会などでお互いに祈り合う関係が、忙しい生活の中で支えになりました。

Je veux monter ma gratitude aux frères et sœurs à l'Église Évangélique Internationale de Genève. Du fond du mon cœur, je vous dis merci. Merci pour votre encouragement et vos prières pour moi, surtout quand je étais dans une situation difficile.
J'aime parler avec vous et échanger situation de l'autre chaque semaine, et d'étudier la Bible ensemble. Le temps dans l'église a été de me donner la force tout au long de mon séjour au CERN.

I would like to express my thankfulness to all of my friends, who gave me advices, who encouraged me and sustained me through prayers, especially when the situation felt difficult for me. I want to say thank you to each of you.

ここまで、様々な形で私を育ててきた下さった全ての方に感謝します。特に、自分を産み、育て、また理解をもって導いてくれた父・母に心からの感謝を表します。
また、論文の追い込み時期には心から気遣ってくれ、様々な形で助けてくれ、必要な休息も与えてくれた家族のひとりひとりに感謝します。
そして、私を造り、全ての必要を満たし、いつも支えてくださっている主なる神に感謝し、誉れを帰します。

しかし私にとっては、
神の近くにいることが、しあわせなのです。
私は、神なる主を私の避け所とし、
あなたのすべてのみわざを語り告げましょう。

（詩編*73:28*　聖書 新改訳©1970,1978,2003 新日本聖書刊行会）

*But for me it is good to be near God;*
*I have made the Lord GOD my refuge,*
*that I may tell of all your works.*

Psalm 73:28

( The Holy Bible, English Standard Version © 2001 Crossway Bibles)

2015年3月20日
樋口　嵩